Contribution to the Physical Interpretation of Characteristic Mode Resonances

Application to Dielectric Resonator Antennas

Tomás Bernabeu Jiménez

Advisor: Alejandro Valero Nogueira

Co-Advisor: Felipe Vico Bondía

Department of Communications
Universitat Politècnica de València

This dissertation is submitted for the degree of
Doctor in Telecommunications Engineering

Institute of Telecommunications
and Multimedia Applications

August 2017

A mis padres y hermanas

Acknowledgements

Habiendo dejado los agradecimientos para lo último me resulta imposible empezar... Este viaje no ha sido fácil, han sido muchas las adversidades tanto profesionales como a nivel personal con las que he tenido que lidiar. El llevar a cabo este trabajo no sólo me ha preparado para desarrollarme profesionalmente, sino algo que considero todavía más importante, mi crecimiento personal. Un crecimiento que me ha permitido conocerme mucho más y ser capaz de entender mejor el mundo y las personas que me rodean. Es por eso que considero fundamental nombrar a todos aquellos que han contribuido a que esto haya sido posible. Porque sin vuestro apoyo hubiese resultado muchísimo más complicado y difícil.

En primer lugar, quisiera agradecer a mi director de tesis, Alejandro Valero, la oportunidad que un día me dio para empezar con este proyecto. En un principio la tesis tenía una dirección distinta, quizás más ingenieril. Y con el transcurso de los años me hizo sentir cómodo y sentí mi fluir como físico, dándome libertad para investigar aquello que me pareciese interesante, pero marcando el punto ingenieril que yo no tenía y he ido aprendiendo. Por esto, y por haber sido paciente, por haberme guiado como corresponde, por tu tiempo...porque he aprendido mucho de ti... te doy las gracias!

En segundo lugar, quisiera agradecer a mi codirector de tesis Felipe Vico su ayuda en la comprensión de las formulaciones integrales, las matemáticas que han intervenido en este trabajo. Han sido muchas las horas de pensar que me has dedicado, y al final... todo ha dado su fruto.

Después, quiero darte las gracias a ti, Daniel Sánchez! Considero que además de Alejandro y Felipe, tú has aportado mucho a este trabajo. Y al igual que a todos los que pasamos por el GRE me has dedicado muchísimo tiempo. Por esto... gracias!

Agradecimientos también para mis colegas Miguel Junior, Toni Vila, Bernat, y Alfonso. Habéis estado siempre apoyándome y aconsejándome, en los buenos

y malos momentos. Después de todos estos años juntos... gracias por todo chicos!

A mi amiga Nora, tu apoyo durante estos años ha sido fundamental. He podido contar siempre contigo, para cualquier cosa, y siempre has conseguido calmarme y hacerme ver las cosas de una mejor manera. Por eso te doy las gracias.

A mi amiga Alicia, siempre tan divertida. Gracias por tus consejos y apoyo. Ha sido un placer haber coincidido contigo.

Además, agradecer de manera especial a mi gran amigo Toni Berenguer todo lo que me ha ayudado. Has sido un pilar para mi, siempre has sacado tiempo para echarme una mano. Hemos disfrutado mucho juntos, hemos despertado juntos. No podía haberme llevado nada mejor al venirme a la UPV que conocerte. Ya sabes que para mi eres como un hermano, y que te aprecio como tal.

También agradezco a Miguel Ferrando, Eva Antonino, Marta Cabedo, y a José Ignacio Herranz vuestras sugerencias y ayuda. Siempre habéis estado dispuestos cuando lo he necesitado. A ti, María!! Mariano y Vicent Miquel Y al resto de compañeros y profesores del GRE, muchísimas gracias!

On the other hand, I would like to express my sincere grateful to the research groups where I was as stays during my PhD:

First, thanks to Professor Roberto Rojas-Teran from The Ohio State University (USA) and his students, who gave me the possibility to learn together with his group in my thesis beginnings. And also thanks to introduce me to Robert Garbacz, the inventor of the Theory of Characteristic Modes. It was an unforgettable moment.

And second, thank you so much to Professor Ahmed Kishk from Concordia University in Montreal (Canada). With whom in an advanced time of my PhD I was able to discuss numerous physical and mathematical aspects of my thesis. With him I concluded the main ideas presented in this work. Because of that, I am very grateful. Thank you also to his wonderful group of students, who made me spend a very pleasant stay. Especially to my friend Mehdi Ardavan with whom I had very funny and good moments. And especially also to my colleague Mohamed A. Moharram for his friendship, who allowed me to check with his numerical programs that the analytical solution for the EFIE for the circular waveguide I solved was correct.

També voldria donar les gràcies a tots els meus amics i companys de carrera, en especial a Raül, Pau, Elena, Juanma, Rosa, Varito mágico i Fedex, el seu

afecte i suport. Sempre he pogut comptar amb vosaltres. Per això moltes gràcies!

Agradecimientos también a mis amigos de la Old School, en especial a Marcus, Julius, Jimmy, Etool ,Paul y Lance. Sois como mis hermanos! Y siempre me habéis apoyado. A mi tete Enrique y a mi amigo Oscar por vuestra verdadera amistad y preocupación. A mis amigas Isa Supri y Sarita de Valencia en cuyos inicios de tesis os conocí y habéis estado para lo que necesitase. A mi hermanito pequeño Cristian John forever! Y a mi gran amiga Verito. Muchas gracias también a mi amiga y hermana Ipticem, por tu apoyo y especial manera de ser con la gente que quiero. A todos muchas gracias.

También quiero agradecer a Mónica su comprensión y cariño. Por todo tu apoyo y haber compartido conmigo el periodo más complicado de este trabajo. Gracias también a tu familia, siempre pendiente de mi: María, Pepe, Marisa, Tatá, Paco, Eva, Marta, Guille y Mónica.

Por último, y para mi los más importantes! Mi familia! En especial: Papá, Mamá, Soraya, Carla, Juancar y J. Pablo. Porque me habéis transmitido apoyo, coraje, y fuerza. Porque doy gracias de teneros siempre cerca. Porque sois únicos! Gracias por vuestro amor incondicional.

A todos! Muchísimas gracias por haber contribuido a mi bienestar y haberme enseñado tanto. Sois los mejores!

Resumen

En la última década, la teoría de los modos característicos está siendo utilizada por muchos grupos de investigación en todo el mundo. Este tema y su uso en diferentes diseños de antenas metálicas está creciendo muy rápido. Sin embargo, la mayoría de las aplicaciones se han concentrado únicamente en antenas metálicas sin ningún conocimiento físico acerca de sus limitaciones y su interpretación física. Además, en lo que se refiere a cuerpos dieléctricos, no han habido tantos artículos publicados como en metales. La razón es que existen diferentes formulaciones integro-diferenciales y la interpretación de sus soluciones no es tan obvia como en cuerpos metálicos. En esta tesis se presenta una interpretación física de las soluciones de la Teoría de Modos Característicos al considerar cuerpos metálicos y dieléctricos sin pérdidas.

Las conclusiones de esta tesis nos permitirán comprender mejor las soluciones de la Teoría de Modos Característicos y sus limitaciones. Esto es importante en ingeniería de antenas. Además, este análisis permitirá desarrollar un nuevo método para el diseño de antenas basadas en resonadores dieléctricos, DRA. Este método está basado en la formulación PMCHWT y la función de Green multicapa utilizada en el método de los momentos (MoM). A este nuevo método se le ha denominado "Substructure Characteristic Mode method", y está basado en la implementación de los complementos Schur sobre las submatrices del operador del MoM. Este estudio permite optimizar el ancho de banda de radiación de un DRA en el mismo proceso de análisis tanto para el dieléctrico como para la alimentación, como por ejemplo una ranura. Además, este método permite comprender como se comporta la ranura en presencia del resonador dieléctrico y viceversa. Este método también puede usarse para diseñar DRA usando permitividades bajas. Esto es importante en el diseño de DRA porque la alimentación perturba el sistema y produce un cambio en las resonancias de los modos característicos. Por lo tanto, al considerar la alimentación en el análisis de modos característicos se obtienen resultados más

realistas comparándolos con los obtenidos mediante un análisis convencional. Así, diseñando con el “Substructure Characteristic Mode method” se pueden extraer nuevas conclusiones sobre el diseño de DRA mediante la Teoría de Modos Característicos.

Resum

En l'última dècada, la teoria dels modes característics està sent utilitzada per molts grups d'investigació en tot el món. Este tema i el seu ús en diferents dissenys d'antenes metàl·liques està creixent molt ràpidament. No obstant això, la majoria de les aplicacions s'han concentrat únicament en superfícies conductores sense cap coneixement físic sobre les seues limitacions i la seua interpretació física. Pel que fa a cossos dielèctrics, no hi ha hagut tants articles publicats com en metalls. La raó és que hi ha diferents formulacions integrodiferencials i la interpretació de les seues solucions no és tan òbvia com en cossos conductors. En esta tesi es presenta una interpretació teòrica considerant cossos conductors i dielèctrics sense pèrdues.

Les conclusions d'esta tesi ens permetran comprendre millor les solucions de la Teoria de Modes Característics i les seues limitacions. Açò és important en enginyeria d'antenes. A més, esta anàlisi permetrà desenrotllar un nou mètode per al disseny d'antenes basades en ressonadors dielèctrics, DRA. Este mètode està basat en la formulació PMCHWT i la funció de Green multicapa utilitzada en el mètode dels moments (MoM). A este nou mètode se li ha denominat "Substructure Characteristic Mode method", i està basat en la implementació dels complements Schur sobre les submatrius de l'operador del MoM. Este estudi permet optimitzar l'amplada de banda de radiació d'un DRA en el mateix procés d'anàlisi tant per al dielèctric com per a l'alimentació, com per exemple una ranura. A més, este mètode permet comprendre com es comporta la ranura en presència del ressonador dielèctric i viceversa. Este mètode també pot usar-se per a dissenyar DRA usant baixes permitivitats. Açò és important en el disseny de DRA perquè l'alimentació pertorba el sistema i produïx un canvi en les ressonàncies dels modes característics. Per tant, al considerar l'alimentació en l'anàlisi de modes característics s'obtenen resultats més realistes comparant-los amb els obtinguts per mitjà d'una anàlisi convencional. Així, dissenyant amb el "Substructure Characteristic Mode method" es poden

extraure noves conclusions sobre el disseny de DRA per mitjà de la Teoria de Modes Característics.

Abstract

The Theory of Characteristic Modes is being adopted by many research groups around the world in the last decade. This topic and their use in different metallic antenna design is growing very fast. However, most of the applications has been only concentrated on conducting surfaces without any physical knowledge about its limitations and its physical interpretation. As far as dielectric bodies are concerned, there have not been so many published articles. The reason is that there are different integro-differential formulations and the interpretation of their solutions is not as obvious as in conducting bodies. Here, a theoretical interpretation considering loss-less conducting and dielectric bodies is presented.

The conclusions drawn in this thesis will allow us to better understand the solutions of the Theory of Characteristic Modes and their limitations. This is important for antenna engineering. In addition, this analysis will allow to develop a novel method for the design of antennas based on dielectric resonators, DRA. This method is called Substructure based-PMCHWT method, and is based on the implementation of the Schur complements of the method of moments matrix operator. This study permits to optimize the radiation bandwidth in the same analysis process for both, the dielectric and the feed, e.g. slot. Moreover, it allows to understand how the slot behaves in the presence of the dielectric resonator and vice versa. This method can also be used to design DRA using low permittivities. This is important in the design of DRA because the feed perturbs the system and produces a shift in the resonances of the characteristic modes. So, therefore, by considering the feed system in the characteristic modes analysis a more realistic results than a conventional analysis is obtained. On the other hand, the resonances of the characteristic modes at low permittivities are displaced from what are the natural resonances of the dielectric resonator and also the corresponding S11 resonance. Thus,

designing with this new method it can draw new conclusions about the design of DRA using the Theory of Characteristic Modes.

Table of contents

List of figures

List of tables

Chapter 1

Introduction

1.1 Problem Statement and Motivation

Telecommunications is probably one of the driving forces in current civilization. As a consequence antenna engineering is living a sweet moment since antennas are needed for many applications and frequency bands. Medical devices, e-commerce, bluetooth-enabled devices, wireless computer networks, drones, Internet of Things (IoT), and wireless communications, are some of the new applications where antennas are implemented to transmit and/or receive electromagnetic signals. Depending on the application, antennas are designed to operate efficiently in a desired frequency range and meet the demanded specifications. Moreover, they can take many geometrical forms and be composed by metal and/or dielectric/magnetic materials to satisfy the requirements set out. This is where the antenna engineer comes in. He is the responsible for designing the antenna model effectively to fulfill all the requirements. In order to do so, it is important to find the best computational design method to meet the needs of the antenna to be designed.

Nowadays, the most popular computational techniques are probably the method of moments (MoM) [56], the finite-difference time-domain (FDTD) method [69], and the finite element method (FEM) [60]. These numerical techniques are used depending on the user's requirements. For instance, while MoM is more efficient when designing open region problems involving PEC or homogeneous media objects, FEM is more efficient for closed region problems involving complex geometries and inhomogeneous media objects. Although these three techniques usually provide approximately the same solutions (total

electromagnetic fields or currents), they do not provide a physical insight of the electromagnetic phenomena involved. This, certainly, is not necessary to design the antenna in a brute force way, but it is very much desirable to understand better the design procedure and to be able to design more efficiently and easily the antenna under concern. In this thesis, special focus will be given to MoM, and also to the benefits that this method provides when diagonalizing its corresponding integro-differential operators.

As far as MoM is concerned, two diagonalization procedures can be done. The standard eigenvalue problem (SEP) that diagonalizes the entire MoM operator, as done in the eigenmode expansion method (EEM) introduced by Baum [13] and the generalized eigenvalue problem (GEP) considered in the theory of characteristic modes (TCM), introduced by Garbacz [49]. These methods diagonalize the electric field integral equation (EFIE) operator, $Z = R + jX$ as follows: EEM with the SEP as $ZI_n = \nu_n I_n$, and TCM with the GEP as $XJ_n = \lambda_n RJ_n$. Although both techniques provide results which are independent of any excitation and it is possible to see how much the eigenmodes contribute to the total currents or fields when a source is added, there are many differences between them. The most important differences are:

- The EEM provides the natural modes, while the TCM provides the characteristic modes.
- The EEM solutions are generally complex valued, while the TCM solutions are real numbers.
- To find the resonances of the EEM, known as natural resonances (NRs), the use of the complex frequency plane is needed, while to find the resonances provided by the TCM, known as characteristic mode resonances (CMRs), it is only needed a real frequency axis.
- The EEM's far field basis are not orthogonal, whereas the TCM is [57].

However, although both methods give a physical insight, the TCM is more intuitive and less time-consuming during an antenna design procedure. This results interesting because it is easier to handle and understand real than complex valued solutions. This translates into an optimum way for antenna design. That is why the TCM helps in the design, offering information that other methods can not provide.

Maybe, because of that, the number of publications dealing with the TCM in the last ten years have soared, and the TCM is nowadays being considered a key tool in the advanced antennas design methods. Fig. 1.1 shows the number of publications as a function of time.

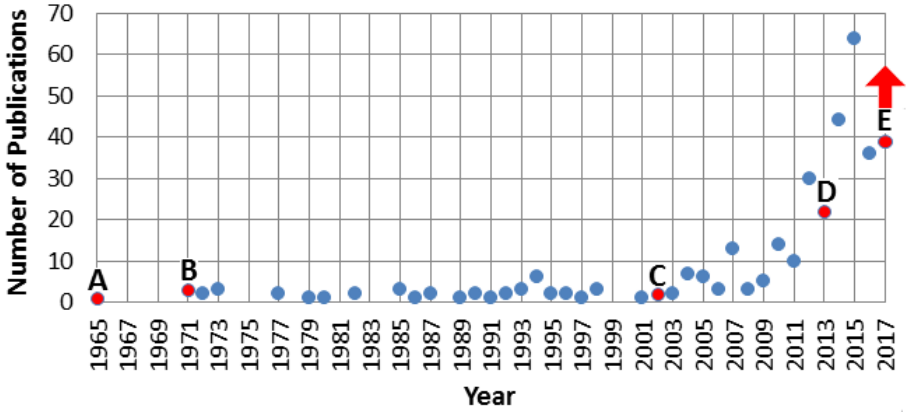

Fig. 1.1 IEEExplore Characteristic Modes search. Number of publications versus years

As shown in Fig. 1.1, the number of publications as function of years follows an exponential behaviour in IEEExplore. First, the characteristic mode idea was introduced by Garbacz in 1965 (A), [49]. Later, Harrington et al. defined the characteristic mode concept based on MoM in 1971 (B). It was in 2002 when the number of publications shooted. Then, the Electromagnetic Raditation Group (GRE) at Universitat Politècnica de València started to develop two PhD thesis published in 2007 [26], and 2008 [40]. In 2013, the GRE started working on TCM to design DRA (D) [46]. Finally, in 2017 the number of publications continue growing (E).

Some of the most interesting applications where the TCM is being applied are vehicular antennas, chassis mobile phones, MIMO design, fractal antennas, reflectarrays, patch antennas, DRA, inverse scattering and metamaterials, among others. In addition, the TCM is being extended to other fields. Interestingly enough, companies like Samsung, Siemens and Nokia are using TCM to design their mobile antennas taking the effect of the chassis into account. As a last token of the momentum TCM is gaining lately, it is worth mentioning that FEKO, CST or WIPL-D, well-known electromagnetic simulation suites, have

included CM computation modules in their solvers. As a matter of fact, in [27] the performance of commercial simulators and academic packages have been thoroughly investigated.

From this it derives the importance of studying the TCM and its performance, because there are still unknown aspects in the interpretation of the solutions provided by the TCM. Not only on PEC bodies, but also in dielectric/magnetic bodies. It is also worth citing Baum in [14], and Chang and Harrington in [28] in this regard, and I quote:

- Baum: "Another type of frequency domain modes is weighted eigenmodes of the form used by Garbacz and Turpin, and by Harrington and Mautz. These are referred to as characteristic modes to distinguish them from the EEM eigenmodes. They have been shown to be useful for frequency domain design and analysis of antennas and scatterers. These characteristic modes have some similar relations to the singularity expansion method (SEM) quantities but appear to be more complicated for this purpose. **More work is needed to further explore these relations.**" In this work a comparison between the SEM and EEM was done in 1976.

- Chang and Harrington: "It is expected that this is one of the important areas for future research. **Many questions are still left unanswered in the interpretation and application of characteristic modes to material objects.** It is hoped that this work will be of some value to future researchers in their effort to gain a complete understanding of the theory of characteristic modes." In this work the TCM was formulated considering the PMCHWT formulation for material bodies in 1977.

Thus, a physical interpretation of the solutions in metals and dielectrics is of interest to establish the theoretical bases of the TCM. That is why, an objective of this thesis is to try to provide an answer to some of the main theoretical questions that remain open in this theory. This thesis will be the first to link natural modes to characteristic modes for metal and dielectric materials.

In addition, as far as DRAs are concerned, they are designed based on known natural modes for isolated DRAs without any considerations of the excitation mechanisms and the involved ground plane. Including the excitation mechanisms and the ground plane in the analysis will lead to more accurate designs. This is other of the outcomes of this thesis.

1.2 State of the Art

Since Garbacz first proposed the Theory of Characteristic Modes (TCM) in 1968, TCM is being increasingly used for antenna design and extended to other fields in electromagnetics. This theory was first formulated by Garbacz for metal bodies of arbitrary shape through the scattering matrix diagonalization [49]. Conceptually, Garbacz was the first to show that there exists a modal representation for any scattered or radiated field for any obstacle that acts as a real Hilbert space basis [48]. Later, Harrington, Mautz and Chang reformulated this theory establishing a more direct method to obtain Garbacz's modal expansion. They considered integro-differential formulations using the impedance matrix of the Method of Moments (MoM), [28, 29, 54, 55]. The generalized eigenvalue problem is solved for the eigenvalues and the eigencurrents. The fields radiated by these eigencurrents are called Characteristic fields. Similarly to the characteristic currents, characteristic fields also form an orthonormal real basis in Hilbert space. Characteristic Modes (CM) depend only on the shape and material of the body and are independent of any excitation. Moreover, as a set of orthogonal eigenfunctions, they can be used to generate the total current on its surface or on the radiated far field for any given excitation. Lastly, in contrast to other forms of design methods, CM give a physical insight into the radiating phenomena taking place in the antenna.

Methodologically, in order to extend the computation of CM to arbitrarily shaped bodies, Harrington and Mautz generalize the analysis in 1971 based on an integral equation formulation [53]. However no in-depth physical interpretation for these modes was given for antenna analysis and design until the work of Cabedo-Fabres [23, 26] where it was shown how the TCM can be systematically applied to design wire and planar antennas. As a continuation of Cabedo-Fabres' work, in the same research group at Universtitat Politècnica de València, Antonino-Daviu presented a work focused in the connection between modal methods and characteristic modes and on the effect of the feeding configuration and location on the modal excitation using the TCM [40]. Another interesting dissertation about FDTD application in CM was published by Surittikul [107, 108]. After these works, a dissertation about planar fractal antennas was developed by Hazdra [107]. Later, Obeidat's work used the TCM with the theory of matching networks to increase both the input impedance bandwidth and the far field radiation pattern bandwidth [88], and Raines's thesis provided a systematic approach to designing complex radiator systems, especially those

involving more than one antenna [94]. Publications have soared in antenna design since these theses.

From the application point of view, recently the TCM is being applied to the design of shipboard antennas in HF band [32], chipless RFID tags [98], slots etched in a metallic finite-sized ground plane [83, 84], orthogonal MIMO handset antennas [73], Non-Foster circuits and multiport reactive matching loading technique [42, 101], reflectarrays [25], vehicular antennas [87], and so on. Another interesting area is metamaterials, in which a recent dissertation has been published [93]. Moreover, thanks to the application of efficient algorithms like Multilevel Fast Multiple Method Algorithm to CM computation [39], TCM is expanding to new fields of application involving electrically larger bodies, where the conventional MoM-based approach is severely challenged. On the other hand, TCM is being also extended to other integral formulations. Some of this formulations and its applications can be found in [34]. Other applications in which TCM has been used are those related to use of the supporting structure itself as an antenna. Here, the structure is able to broadcast radio signals. These applications are amphibious assault vehicles [104], mobile phone chassis [10, 11, 44], car chassis [75], ships [36], and aircrafts [31]. This is a practical point of view, turning structures into transmitters making antennas more efficient enhancing communication between transmitter and receiver.

Nevertheless, there are not many works to date on the use of this theory to explain dielectric antennas and scatterers, or dielectric antennas containing electric/magnetic parts. It is a more complex problem since different integral equation approaches can be tried. It has been observed that depending on the approach, modes obtained can change and its physical interpretation is not obvious.

Concerning to conventional methods in designing dielectric-based antennas, the most important references are the following. In 1939, Richtmyer [100] showed that unmetallized dielectric objects can function much like metallic objects, which he called dielectric resonators (DR). It is well known that dielectric objects can resonate in various modes. Due to that, DR were first implemented as microwave filters in 1968 where high permittivity was used [37, 58]. Later, Long et al. [76] introduced DR as application for antennas, called dielectric resonator antennas (DRA). Radiation characteristics [65], computed resonance frequencies [66], modal field distributions [62] and more, were realized for different canonical DRA. DRA have interesting features such as greater bandwidth,

simple feeding, high radiation efficiency, and easy fabrication. Furthermore, DRA avoid conducting loss when high frequencies are employed.

From the point of view of design, applying the TCM becomes interesting because it allows us to obtain separately each CM that can be excited and the best position for the feed in order to feed a selected mode. Moreover, the TCM gives the possibility to know the contribution of these modes when the excitation is considered. In addition, the TCM can be applied to a certain substructure part of a more complex structures demonstrated in [7, 9, 20, 43, 106]. Such feature is very appealing for DRA design methods since it separates the DR from the slot or coaxial probe through which the DR is fed. This and other properties will be discussed throughout this thesis.

The research considered in this thesis concerns mainly to the study of the TCM applied to conducting and dielectric canonical bodies, an infinite circular cylinder and a sphere. The selection of a canonical problem has been made to be able to provide further knowledge not available from numerical analysis even using the TCM. In addition, this thesis presents a novel method to design DRA. This method provides more realistic results than the conventional design methods. Furthermore, it also provides relevant information during the design procedure not obtained from other techniques.

1.3 Structure of the Thesis

This thesis is divided into two parts. The first one deals with the physical interpretation of characteristic resonances in conducting and dielectric bodies, and the second part with the design of DRA with a new design method, extension of the TCM.

Chapter 2 presents an introduction to the integral formulations governing the TCM for the analysis of conducting and dielectric bodies. In the case of conducting bodies the EFIE is used. Whereas for dielectrics, VIE and PMCHWT formulations have been selected. The formulations presented here do not consider losses.

In Chapter 3, characteristic mode resonances and natural resonances are compared first for a straight wire, and later for an infinite PEC circular cylinder, and a PEC sphere. Furthermore, a connection between the SEP and the GEP is presented, helping to understand the definition of the characteristic eigenvalues and their resonances. Finally, a method to obtain the dispersion diagram in a PEC circular waveguide is presented.

Chapter 4 presents a comparison between the natural resonances and characteristic mode resonances for an infinite dielectric circular cylinder and a dielectric sphere. This study has been done based on the PMCHWT formulation. Moreover, some conclusions with regard the resonances of DR with low permittivities are also presented. Finally, the physical contribution of the so-called *non-physical* modes to the electric and magnetic equivalent currents, and also to its associated fields is presented. This study has been analytically realized for a TM^z plane-wave incidence and an electric line source located inside the cylinder.

Chapter 5 will focus exclusively on DRA design using previous conclusions drawn in previous chapters. Here, a new method to design DRA based on the substructure characteristic mode concept is developed. This method is compared with a conventional approach based on the computation of characteristic modes of an isolated DR. Unlike the conventional method, this new approach takes into account the surrounding structures influencing the actual resonance of a DR with low permittivity.

Finally, chapter 6 presents the conclusions arrived at in this thesis.

Chapter 2

The Theory of Characteristic Modes

2.1 Introduction

In this chapter, a brief summary of the TCM applied to conducting, dielectric and/or magnetic bodies is presented. The EFIE formulation for conducting bodies is shown first. Then, the VIE-EFIE and the PMCHWT integro-differential formulations used in dielectric bodies are also presented. The difference between these two last formulations is the domain where the equivalent currents are defined. The VIE-EFIE uses only electric currents and are defined volumetrically inside the dielectric body. The PMCHWT formulation uses both electric and magnetic currents and are defined on the dielectric and/or magnetic body surface. There exists a complete VIE formulation defining any dielectric and/or magnetic body, but for what comes to be the object of this thesis we are only interested in dielectric bodies, although the conclusions of this thesis can be generalized to the complete VIE formulation. Another important aspect in differentiating both formulations is that the VIE-EFIE formulation serves for solving both homogeneous and inhomogeneous dielectric bodies. In contrast to this, the PMCHWT formulation only serves for solving homogeneous bodies. It is important to note that since VIE-EFIE requires a volumetric meshing the number of unknowns is greater than the PMCHWT formulation because it only requires a surface meshing. Thus, the matrix operators calculation involved in the PMCHWT formulation is much lighter than for the VIE-EFIE formulation.

The integral formulations presented here will not consider lossy materials. Furthermore, this thesis will only refer to homogeneous dielectric bodies.

2.2 Conducting Bodies

CM concept can be easily applied to any metallic surface after the appropriate definition of the integro-differential operator involved. In this case, Harrington and Mautz [54] defined the TCM using the EFIE formulation to obtain the same modes defined by Garbacz in [49]. As far as this work is concerned, only PEC bodies are studied.

2.2.1 Characteristic Currents and Characteristic Eigenvalues

Let the PEC body be represented as in Fig. 2.1, where $\mathbf{E}^i$ and $\mathbf{E}^s$ are the incident and the scattered electric fields, respectively. The EFIE describes both the tangential incident field, and scattered electric field on an arbitrary PEC surface by imposing the following boundary conditions, $\hat{n} \times \left(\mathbf{E}^s + \mathbf{E}^i\right) = 0$.

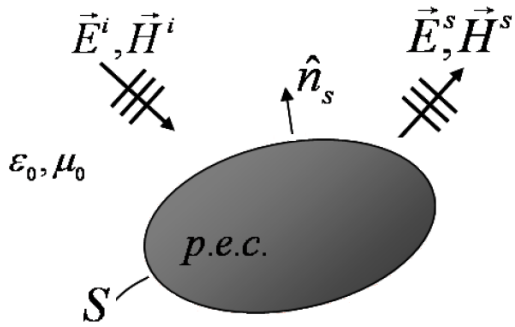

Fig. 2.1 A general PEC body. Image taken from the lecture notes of the ESoA course book [74]

That means the tangential components of the total electric field, $\mathbf{E}^T = \mathbf{E}^s + \mathbf{E}^i$, on the PEC body have to be zero. The scattered field $\mathbf{E}^s$ can be expressed as a function of the vector and scalar potentials.

$$\mathbf{E}^s = -j\omega\mathbf{A}(\mathbf{J}) - \nabla\phi(\mathbf{J}) \tag{2.1}$$

Where $\mathbf{A}$ and ϕ are the magnetic vector and the electric scalar potentials, and are defined as

$$\mathbf{A}(\mathbf{J}) = \frac{\mu}{4\pi}\iint_S \mathbf{J}(\mathbf{r'})\frac{e^{jk|\mathbf{r}-\mathbf{r'}|}}{|\,\mathbf{r}-\mathbf{r'}\,|}dS' \qquad \text{Magnetic vector potential} \tag{2.2}$$

$$\phi(\mathbf{J}) = -\frac{1}{4\pi j\omega\varepsilon}\iint_S \nabla'\mathbf{J}(\mathbf{r'})\frac{e^{jk|\mathbf{r}-\mathbf{r'}|}}{|\,\mathbf{r}-\mathbf{r'}\,|}dS' \qquad \text{Electric scalar potential} \tag{2.3}$$

In equations (2.2) and (2.3), $\mathbf{r}$ is the observation point, $\mathbf{r'}$ denotes the source point, S is the scattering surface, S' is the surface on which we integrate, ω is the angular frequency, and μ, ε and $\mathbf{k}$ are the outer media permeability, permittivity, and wavenumber, respectively.

Thus, substituting the potentials (2.2) and (2.3) in equation (2.1), and (2.1) in $\hat{n}\times\left(\mathbf{E}^s+\mathbf{E}^i\right)=0$, the following expression is obtained

$$\hat{n}\times\mathbf{E}^i = \tag{2.4}$$
$$\hat{n}\times\left[j\omega\mu\iint_S \mathbf{J}(\mathbf{r'})G(|\,\mathbf{r}-\mathbf{r'}\,|)dS' - \frac{1}{j\omega\varepsilon}\nabla\iint_S \nabla'\mathbf{J}(\mathbf{r'})G(|\,\mathbf{r}-\mathbf{r'}\,|)dS'\right]$$

In which $G(|\,\mathbf{r}-\mathbf{r'}\,|) = \frac{e^{jk|\mathbf{r}-\mathbf{r'}|}}{|\mathbf{r}-\mathbf{r'}|}$ is the free space Green's function. Furthermore, equation (2.4) can be rewritten as an operator equation as follows,

$$\left[L(\mathbf{J}) + \mathbf{E}^i\right]_{tan} = 0 \tag{2.5}$$

where L is a linear operator acting on the surface electric current. And the subscript *tan* denotes the surface tangential component of the fields. Moreover, because of its physical dimensions, this operator can be seen as an impedance operator, i.e., it is recommended to redefine it as $[-L(\mathbf{J})]_{tan} = Z(\mathbf{J})$. Where the operator Z is complex and symmetric. For convenience, it becomes interesting

to separate the impedance operator into its real and imaginary parts such $Z = R + jX$. In such a way that we can use its mathematical properties, since R and X are hermitian operators.

At this point, it is important to introduce the symmetric product (2.6). This inner product reduces the operator equations into matrix equations.

$$\langle \mathbf{B}, \mathbf{C} \rangle = \iint_S \mathbf{B} \bullet \mathbf{C} \, dS' \tag{2.6}$$

Where $\mathbf{B}$ and $\mathbf{C}$ are two vector functions of the square-integrable space on S. The product $\langle \mathbf{B}^*, \mathbf{C} \rangle$, where the asterisk denotes complex conjugate, defines an inner product for the Hilbert space of square integrable vector functions on S.

Turning to the definition of the R operator, it is noteworthy that if R is positive semidefinite, then the power radiated by a current $\mathbf{J}$ on S is $\langle \mathbf{J}^*, R\mathbf{J} \rangle \geq 0$. On the other hand, if no resonator field exist internal to S, i.e., no cavity is involved, then R is positive definite, i.e., $\langle \mathbf{J}^*, R\mathbf{J} \rangle > 0$, and that means all the electric currents radiate some power, however small.

Now, consider the following generalized eigenvalue equation

$$Z(\mathbf{J}_n) = \nu_n M(\mathbf{J}_n) \tag{2.7}$$

where Z is the operator matrix to be diagonalized, $\mathbf{J}_n$ are the eigencurrents of the conducting body defined on S, ν_n their corresponding eigenvalues, and M a weight operator to be chosen. Only if $M = R$ the eigencurrent or characteristic currents $\mathbf{J}_n \in \mathbb{R}$, and $\nu_n = 1 + j\lambda_n$. Being $\lambda_n \in \mathbb{R}$ the characteristic eigenvalues. Therefore, in order to get a more compact equation, these definitions can be substituted in equation (2.7), i.e., $M = R$, $\nu_n = 1 + j\lambda_n$, and $Z = R + jX$. Reordering it is easy to obtain the following equation governing in the TCM.

$$X(\mathbf{J}_n) = \lambda_n R(\mathbf{J}_n) \tag{2.8}$$

In (2.8) the characteristic currents $\mathbf{J}_n$ must satisfy the following orthogonality relationships.

$$\langle \mathbf{J}_m, Z(\mathbf{J}_n) \rangle = \langle \mathbf{J}_m^*, Z(\mathbf{J}_n) \rangle = (1 + j\lambda_n)\delta_{m,n} \tag{2.9}$$

$$\langle \mathbf{J}_m, R(\mathbf{J}_n) \rangle = \langle \mathbf{J}_m^*, R(\mathbf{J}_n) \rangle = \delta_{m,n} \tag{2.10}$$

$$\langle \mathbf{J}_m, X(\mathbf{J}_n) \rangle = \langle \mathbf{J}_m^*, X(\mathbf{J}_n) \rangle = \lambda_n \delta_{m,n} \tag{2.11}$$

The three equations define the power balance between reactive and active power of the characteristic modes. Where $\delta_{m,n}$ is the Kronecker Delta function defined as

$$\delta_{m,n} = \begin{cases} 1 & \text{if } m = n \\ 0 & \text{if } m \neq n \end{cases}$$

As can be seen from (2.10), these characteristic eigencurrents are normalized to radiate unit power. Each eigencurrent associated with an internal resonance cannot be normalized since they do not radiate. Nevertheless, they are not needed for radiation problems, only for cavity problems. For the following, we assume the eigencurrents to be normalized.

Equations (2.10) and (2.11) are implicitly included in equation (2.9). Thus, these orthogonality relations are used to normalize the characteristic currents, and to obtain the characteristic eigenvalues associated to those characteristic currents.

To finalize with this discussion, it is important to understand how the eigenvalues are defined. By definition the characteristic eigenvalues, λ_n, range from $-\infty$ to $+\infty$. Furthermore, if $\lambda_n > 0$, those related modes have predominantly storing magnetic energy (inductive modes), while if $\lambda_n < 0$, they predominantly store electric energy (capacitive modes). A mode having $\lambda_n = \pm\infty$ is called an internally resonant mode. And a mode having $\lambda_n = 0$ is called an externally resonant mode. Those modes corresponding to the external resonances for the conducting surface are those involved to design antennas and scatterers.

In addition, it is common to define another parameter widely used in the TCM, the modal significance, [23].

$$MS_n = \left\| \frac{1}{1 + j\lambda_n} \right\| \tag{2.12}$$

This parameter has only dependence of the characteristic eigenvalue, and it is another way of viewing the information contained in it. For example, the resonance will be at $MS_n = 1$. The interesting thing about this parameter is that it allows us to define the radiation bandwidth of a given mode, BW_n. BW_n is defined as the range of frequencies in which the power radiated by the mode is greater than half the power radiated at resonance, we have that $MS = 0.707$, and therefore

$$BW_n = \frac{f_U - f_L}{f_r} \tag{2.13}$$

In (2.13) f_U is the upper frequency and f_L the lower frequency. These are the corresponding frequencies to the cut of $MS = 0.707$ with the MS_n curve, and f_r the resonance frequency for that given mode, n. This is the bandwidth of each characteristic mode that could intervene in the radiation of the antenna/scatterer in the case to be excited.

2.2.2 Modal Solutions

Once the characteristic modes and its associated eigenvalues are obtained, it is possible to construct the total current distribution and its associated radiated fields through these solutions.

The total current distribution can be constructed considering the following equation,

$$\mathbf{J} = \sum_n \alpha_n \mathbf{J}_n \tag{2.14}$$

where α_n is a coefficient to be determined for each corresponding characteristic current $\mathbf{J}_n$. α_n can be obtained substituting (2.14) in equation (2.2.1), and using the linearity of the L operator. By doing so, equation (2.15) can be obtained.

$$\left[\sum_n \alpha_n L(\mathbf{J}_n) + \mathbf{E}^i\right]_{tan} = 0 \tag{2.15}$$

Next, an inner product considering each characteristic current $\mathbf{J}_m$ is considered. This gives the following equation,

$$\sum_n \alpha_n \langle \mathbf{J}_m, Z(\mathbf{J}_n) \rangle = \langle \mathbf{J}_m, \mathbf{E}^i \rangle \tag{2.16}$$

where $m = 1, 2, \ldots$. Here we have put $L_{tan} = -Z$, and dropped the subscript "tan" on $\mathbf{E}^i$. Because of the orthogonality relationship (2.9), equation (2.16) is reduced to

$$\alpha_n (1 + j\lambda_n) = \langle \mathbf{J}_m, \mathbf{E}^i \rangle \tag{2.17}$$

where α_n takes the following form,

$$\alpha_n = \frac{\langle \mathbf{J}_n, \mathbf{E}^i \rangle}{(1 + j\lambda_n)} \tag{2.18}$$

In equation (2.18), $\langle \mathbf{J}_n, \mathbf{E}^i \rangle$ is called the modal excitation coefficient defined as

$$V_n^i = \langle \mathbf{J}_n, \mathbf{E}^i \rangle = \iint_S \mathbf{J}_n \mathbf{E}^i dS' \tag{2.19}$$

Thus, the total electric current distribution takes the form,

$$\mathbf{J} = \sum_n \frac{V_n^i}{(1 + j\lambda_n)} \mathbf{J}_n \tag{2.20}$$

If the eigencurrents $\mathbf{J}_n$ are not normalized, the term $(1 + j\lambda_n)$ has to be replaced by the term $(1 + j\lambda_n)\langle \mathbf{J}_m, R(\mathbf{J}_n) \rangle$.

Let us now turn to the definition of the electric and magnetic fields. The electric field $\mathbf{E}_n$ and the magnetic field $\mathbf{H}_n$ produced by an eigencurrent $\mathbf{J}_n$ on S are called the characteristic fields. The set of all the $\mathbf{E}_n$ or $\mathbf{H}_n$ form a Hilbert space throughout the space. These fields can be obtained once the characteristic currents have been obtained from equation (2.1), and from its associated magnetic field,

$$\mathbf{E}_n^s = -j\omega\mathbf{A}(\mathbf{J}_n) - \nabla\phi(\mathbf{J}_n) \tag{2.21}$$

$$\mathbf{H}_n^s = \frac{1}{\mu_0}\nabla \times \mathbf{A}(\mathbf{J}_n) \tag{2.22}$$

The interesting thing here is that when these fields are calculated on the sphere surface at infinity, S_∞, they are newly called characteristic far fields and fulfill the following orthogonality relationship

$$\frac{1}{\eta}\iint_{S_\infty} \mathbf{E}_m^* \mathbf{E}_n dS = \eta \iint_{S_\infty} \mathbf{H}_m^* \mathbf{H}_n dS' = \delta_{m,n} \tag{2.23}$$

So therefore, the characteristic far fields have the property to be orthogonal.

By definition, the characteristic far fields can be obtained considering equation (2.24)

$$\mathbf{E}_n = \eta\mathbf{H}_n \times \mathbf{n} = \frac{-j\omega\mu}{4\pi r} e^{-jkr}\mathbf{F}_n(\theta,\phi) \tag{2.24}$$

where $\mathbf{F}_n$ is defined as

$$\mathbf{F}_n = \iint_S \mathbf{J}_n(\mathbf{r}') e^{-j\mathbf{k}\mathbf{r}'} dS' \tag{2.25}$$

Here $\eta = \sqrt{\mu/\varepsilon}$ is the intrinsic impedance of the space, $\mathbf{n}$ is the unit radial vector on S_∞ and (θ,ϕ) are the angular coordinates of the position on S_∞. The complex vector $\mathbf{F}_n$ is called the characteristic pattern or eigenpattern corresponding to the eigencurrent $\mathbf{J}_n$. $\mathbf{F}_n$ is calculated integrating on the object surface, S', where the electric sources $\mathbf{J}_n$ are located at the $\mathbf{r}'$ position.

Since the far fields are linearly related with the currents they can also be expanded in terms of the characteristic far fields considering the same excitation coefficient (2.18)

$$\mathbf{E} = \sum_n \frac{V_n^i}{(1+j\lambda_n)}\mathbf{E}_n \tag{2.26}$$

$$\mathbf{H} = \sum_n \frac{V_n^i}{(1+j\lambda_n)}\mathbf{H}_n \tag{2.27}$$

2.3 Dielectric Bodies: EFIE-VIE

In this section a brief review of the theory of characteristic modes for lossless dielectric bodies considering the EFIE-VIE formulation is presented. The approach is similar to that used for conducting bodies, with regard to equation $Z(\mathbf{J}) = \mathbf{E}^i$, but considering another definition for the operator and the involved electric currents. Here, a dielectric body with volumetric equivalent electric currents is considered.

2.3.1 Characteristic Currents and Characteristic Eigenvalues

Consider the homogeneous loss-free dielectric body represented in Fig. 2.2, where the scattered field is related to the volumetric polarization currents $\mathbf{J}$ according to

$$\mathbf{E}^s = -j\omega\mathbf{A}(\mathbf{J}) - \nabla\phi(\mathbf{J}) = -Z_V(\mathbf{J}) \tag{2.28}$$

where the magnetic vector potential and the electric scalar potential are now integrated over the volume V

$$\mathbf{A}(\mathbf{J}) = \frac{\mu}{4\pi}\iiint_V \mathbf{J}(\mathbf{r'})\frac{e^{jk|\mathbf{r}-\mathbf{r'}|}}{|\,\mathbf{r}-\mathbf{r'}\,|}dV' \qquad \text{Magnetic vector potential} \tag{2.29}$$

$$\phi(\mathbf{J}) = -\frac{1}{4\pi j\omega\varepsilon}\iiint_V \nabla'\mathbf{J}(\mathbf{r'})\frac{e^{jk|\mathbf{r}-\mathbf{r'}|}}{|\,\mathbf{r}-\mathbf{r'}\,|}dV' \qquad \text{Electric scalar potential} \tag{2.30}$$

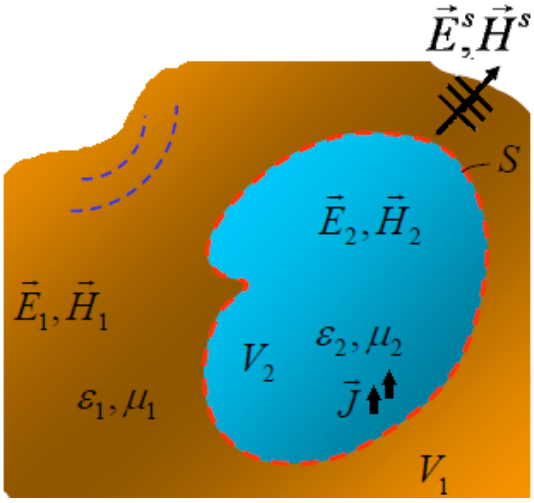

Fig. 2.2 Homogeneous loss free dielectric body. Image taken from the lecture notes of the ESoA course book [74].

If the polarization current is related to the total field by the constitutive relationship

$$\mathbf{J} = j\omega\Delta\varepsilon(\mathbf{E}^i + \mathbf{E}^s) \tag{2.31}$$

where $\Delta\varepsilon = \varepsilon - \varepsilon_0$, it is possible to rearrange in order to obtain the VIE-EFIE substituting (2.31) in (2.28). That is

$$\frac{1}{j\omega\Delta\varepsilon}\mathbf{J} + Z_V(\mathbf{J}) = \mathbf{E}^i \tag{2.32}$$

or in a more compact form

$$Z(\mathbf{J}) = \mathbf{E}^i \tag{2.33}$$

where the operator $Z = Z_V + 1/j\omega\Delta\varepsilon$, and can be treated as in the above section for conducting bodies, but with respect to a volume symmetric product (2.34) in

which **B** and **C** are two vector functions of the square-integrable space defined on V.

$$\langle \mathbf{B}, \mathbf{C} \rangle = \iiint_V \mathbf{B} \bullet \mathbf{C} \, dV' \tag{2.34}$$

This serves to reduce the operator equations to matrix equations. From the reciprocity theorem, it can be concluded that Z_V is a symmetric operator, $\langle \mathbf{J}_1, Z_V(\mathbf{J}_2) \rangle = \langle \mathbf{J}_2, Z_V(\mathbf{J}_1) \rangle$, and if $\Delta\varepsilon$ is a scalar or a symmetric operator, Z remains symmetric. In addition, Z can be expressed into its hermitian parts R and X as $Z = R + jX$, where

$$R = \frac{1}{2}(Z + Z^*) \tag{2.35}$$

$$X = \frac{1}{2j}(Z - Z^*) \tag{2.36}$$

It is important to note that the operator equation (2.33) takes the form as that for conducting bodies, and the development of a TCM for dielectric bodies when considering the volumetric equivalent electric currents is similar to that for conducting bodies. Thus, the generalized eigenvalue equation defining the characteristic modes is the same as for conducting bodies but considering the operator presented by (2.33),

$$X(\mathbf{J}_n) = \lambda_n R(\mathbf{J}_n) \tag{2.37}$$

Here again the eigenvalues λ_n and all the characteristic currents are real valued, since the involved operators X and R are hermitian. Moreover, the volumetric characteristic current, $\mathbf{J}_n$, can be normalized to radiate unit power by using the following orthogonality relationships

$$\langle \mathbf{J}_m, Z(\mathbf{J}_n) \rangle = \langle \mathbf{J}_m^*, Z(\mathbf{J}_n) \rangle = (1 + j\lambda_n)\delta_{m,n} \tag{2.38}$$

$$\langle \mathbf{J}_m, R(\mathbf{J}_n) \rangle = \langle \mathbf{J}_m^*, R(\mathbf{J}_n) \rangle = \delta_{m,n} \tag{2.39}$$

$$\langle \mathbf{J}_m, X(\mathbf{J}_n) \rangle = \langle \mathbf{J}_m^*, X(\mathbf{J}_n) \rangle = \lambda_n \delta_{m,n} \tag{2.40}$$

where $\delta_{m,n}$ is the Kronecker delta.

To finalize, it is important to define the characteristic eigenvalues provided by the VIE-EFIE formulation. Here λ_n ranges from $-\infty$ to $+\infty$. Furthermore, if $\lambda_n > 0$, those related modes have predominantly storing magnetic energy (inductive modes), while if $\lambda_n < 0$ have predominantly storing electric energy (capacitive modes). A mode having $\lambda_n = \pm\infty$ is called an internally resonant mode. And a mode having $\lambda_n = 0$ is called an externally resonant mode. Those modes corresponding to the external resonances for the dielectric body are those involved to design dielectric resonator antennas and dielectric scatterers.

2.3.2 Modal Solutions

In the same manner as for PEC bodies, a modal solution exists for $\mathbf{J}$ and takes the following form

$$\mathbf{J} = \sum_n \frac{V_n^i}{(1+j\lambda_n)}\mathbf{J}_n \tag{2.41}$$

If the eigencurrents $\mathbf{J}_n$ in equation (2.41) are not normalized, the term $(1+j\lambda_n)$ has to be replaced by the term $(1+j\lambda_n)\langle \mathbf{J}_m, R(\mathbf{J}_n)\rangle$. On the other hand, V_n^i is defined as previously done for conducting bodies in equation (2.19) but integrating over the volume where the volumetric currents are defined within the dielectric, V.

$$V_n^i = \langle \mathbf{J}_n, \mathbf{E}^i \rangle = \iiint_V \mathbf{J}_n \mathbf{E}^i dV' \tag{2.42}$$

The electric field $\mathbf{E}_n$ and the magnetic field $\mathbf{H}_n$ produced by a characteristic current $\mathbf{J}_n$ are called characteristic fields and can be obtained from equation (2.28), and from its associated magnetic field.

It is important to note, that when these fields are calculated on the surface sphere at infinity, S_∞, they are also called characteristic far fields and fulfill the following orthogonality relationship

$$\frac{1}{\eta}\iint_{S_\infty} \mathbf{E}_m^* \mathbf{E}_n dS' = \eta \iint_{S_\infty} \mathbf{H}_m^* \mathbf{H}_n dS' = \delta_{m,n} \tag{2.43}$$

In addition to the orthogonality relations presented by equations (2.38)-(2.40), this is another of the properties that make interesting to use the TCM in antenna design. (2.43) shows that the characteristic far fields are orthogonal.

Since the far fields are linearly related with the currents they can also be expanded in terms of the characteristic far fields considering the same coefficients used within the linear combination for the total electric current (2.41).

$$\mathbf{E} = \sum_n \frac{V_n^i}{(1+j\lambda_n)}\mathbf{E}_n \tag{2.44}$$

$$\mathbf{H} = \sum_n \frac{V_n^i}{(1+j\lambda_n)}\mathbf{H}_n \tag{2.45}$$

2.4 Dielectric and/or Magnetic Bodies: PMCHWT-SIE

The PMCHWT-SIE formulation for characteristic modes is more complex than the EFIE-VIE formulation for dielectric bodies because there are both electric and magnetic equivalent currents involved. In this problem, the surface equivalence principle is used to find the matrix operator involved in the problem. To do so, the real problem is then formulated in terms of an equivalent problem facilitating the calculation of the electromagnetic fields in the regions of interest.

The formulation presented in this section only considers materials without ohmic losses. Furthermore, this formulation can be applied for both dielectric and/or magnetic bodies.

2.4.1 Characteristic Currents and Characteristic Eigenvalues

Consider the problem of an object as shown in Fig. 2.3. The object is characterized by (ε_2, μ_2), and the surrounding media by (ε_1, μ_1), both homogeneous materials. Moreover, the object is illuminated by an incident electric and magnetic fields $\mathbf{E}^{inc}$ and $\mathbf{H}^{inc}$, respectively.

Furthermore, the scattered fields outside $(\mathbf{E}_1, \mathbf{H}_1)$ and inside $(\mathbf{E}_2, \mathbf{H}_2)$ the object are also defined in Fig. 2.3. The boundary conditions $\hat{n} \times \mathbf{E}_1 = \hat{n} \times \mathbf{E}_2$ and $\hat{n} \times \mathbf{H}_1 = \hat{n} \times \mathbf{H}_2$ are satisfied between the object and the surrounding media, i.e., the object surface.

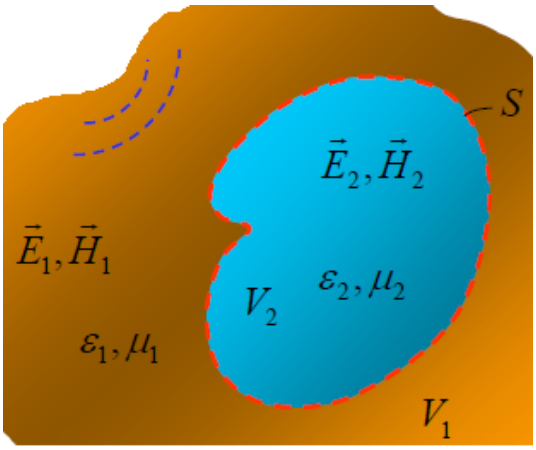

Fig. 2.3 Original problem. Image taken from the lecture notes of the ESoA course book [74]

As the surface equivalence principle establishes, it is possible to separate the original problem presented in Fig. 2.3 into two equivalent problems as presented in Fig. 2.4. As can be seen, the original problem is exactly the sum of these two separate problems, one in which the interior fields are completely zero and the outer fields are produced by the equivalent currents $(\mathbf{J}_1, \mathbf{M}_1)$, and other in which the exterior fields are completely zero and the inner fields are produced by the equivalent currents $(\mathbf{J}_2, \mathbf{M}_2)$. Both cases are shown in Fig. 2.4 as case 1 (right), and case 2 (left). These equivalent currents are related with the fields according the following equations

$$\mathbf{J}_1 = \hat{n} \times \mathbf{H}_1 \tag{2.46}$$

$$\mathbf{J}_2 = -\hat{n}' \times \mathbf{H}_1 \tag{2.47}$$

$$\mathbf{M}_1 = \mathbf{E}_1 \times \hat{n} \tag{2.48}$$

$$\mathbf{M}_2 = \mathbf{E}_2 \times \hat{n}' \tag{2.49}$$

where $\hat{n}$ and $\hat{n}'$ are the normal unit vectors pointing outwards and inwards the surface S, respectively. Since the real problem does not present such equivalent

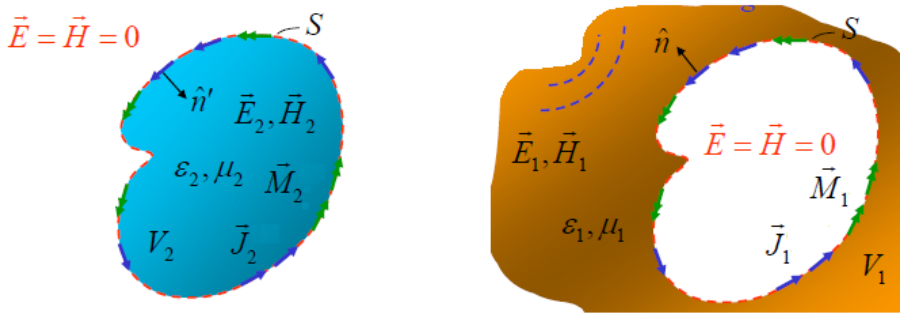

Fig. 2.4 Decomposition of the original problem. Left: The fields are zero outside (case 2). Right: The fields are zero inside (case 1). Image taken from the lecture notes of the ESoA course book [74]

surface currents, the following conditions must be satisfied to continue meeting the boundary conditions on the surface S of the original problem.

$$\mathbf{J}_1+\mathbf{J}_2=0 \tag{2.50}$$

$$\mathbf{M}_1+\mathbf{M}_2=0 \tag{2.51}$$

We now replace in both equivalent problems the medium of the zone where there is EM field, by the medium of that volumetric zone where the field is zero. So that the medium in the two zones becomes equal, both inside and outside the object. That is, the entire space has to be formed by the medium 1 in Fig. 2.4 (right), and the entire space has to be formed by the medium 2 in Fig. 2.4 (left). This means that the equivalent currents radiate into a homogeneous medium, and therefore we can make use of the following equations to calculate the radiated fields produced by the electric and magnetic equivalent currents.

$$\mathbf{E}_1 = -j\omega\mathbf{A}^{(1)} - \nabla\phi_e^{(1)} - \frac{1}{\varepsilon_1}\nabla\times\mathbf{F}^{(1)} + \mathbf{E}^{inc} \tag{2.52}$$

$$\mathbf{H}_1 = \frac{1}{\mu_1}\nabla\times\mathbf{A}^{(1)} - j\omega\mathbf{F}^{(1)} - \nabla\phi_m^{(1)} + \mathbf{H}^{inc} \tag{2.53}$$

$$\mathbf{E}_2 = -j\omega\mathbf{A}^{(2)} - \nabla\phi_e^{(2)} - \frac{1}{\varepsilon_2}\nabla\times\mathbf{F}^{(2)} \tag{2.54}$$

$$\mathbf{H}_2 = \frac{1}{\mu_2}\nabla\times\mathbf{A}^{(2)} - j\omega\mathbf{F}^{(2)} - \nabla\phi_m^{(2)} \tag{2.55}$$

where the superscripts (1) and (2) refer to the exterior and interior regions, respectively. Furthermore, the Green's function of an unbounded homogeneous medium is used, $G_i(|\mathbf{r}-\mathbf{r}'|) = \frac{e^{jk_i|\mathbf{r}-\mathbf{r}'|}}{|\mathbf{r}-\mathbf{r}'|}$. This can be seen from the potentials defined below, for $i = 1,2$.

$$\mathbf{A}^{(i)}(\mathbf{r}) = \frac{\mu_i}{4\pi}\iint_S \mathbf{J}_i(\mathbf{r}')G_i(|\mathbf{r}-\mathbf{r}'|)dS' \qquad \text{Magnetic vector potential} \tag{2.56}$$

$$\mathbf{F}^{(i)}(\mathbf{r}) = \frac{\varepsilon_i}{4\pi}\iint_S \mathbf{M}_i(\mathbf{r}')G_i(|\mathbf{r}-\mathbf{r}'|)dS' \qquad \text{Electric vector potential} \tag{2.57}$$

$$\phi_e^{(i)}(\mathbf{r}) = -\frac{1}{4\pi j\omega\varepsilon_i}\iint_S \nabla'\mathbf{J}_i(\mathbf{r}')G_i(|\mathbf{r}-\mathbf{r}'|)dS' \qquad \text{Electric scalar potential} \tag{2.58}$$

$$\phi_m^{(i)}(\mathbf{r}) = \frac{1}{4\pi j\omega\mu_i}\iint_S \nabla'\mathbf{M}_i(\mathbf{r}')G_i(|\mathbf{r}-\mathbf{r}'|)dS' \qquad \text{Magnetic scalar potential} \tag{2.59}$$

This means the equivalent currents $\mathbf{J}_1$ and $\mathbf{M}_1$ radiate the fields $\mathbf{E}^{(1)}$ y $\mathbf{H}^{(1)}$, and the equivalent currents $\mathbf{J}_2$ and $\mathbf{M}_2$ radiate the fields $\mathbf{E}^{(2)}$ y $\mathbf{H}^{(2)}$. It is important to note that since the problem considered has an external incident electromagnetic

wave, the exterior fields $\mathbf{E}^{(1)}$ and $\mathbf{H}^{(1)}$ are composed by the sum of the scattered fields and the incident fields. While the fields in the interior region are only described as a function of the scattered fields. On the contrary, if the incident field were placed within the object, the definition would be different. In that case, the incident fields would be summed in the interior region, within the fields $\mathbf{E}^{(2)}$ and $\mathbf{H}^{(2)}$. This point will be interesting when analyzing the physical meaning of the solutions provided by the PMCHWT formulation when applied the TCM, as will be explained later.

Once the surface equivalence principle is understood, let us first construct the integral equations of the PMCHWT formulation from the boundary conditions for the electric field $\hat{n} \times \mathbf{E}_1 = \hat{n} \times \mathbf{E}_2$,

$$\hat{n} \times [j\omega\mu_1 \iint_S \mathbf{J}_1(\mathbf{r'}) G_1(|\,\mathbf{r}-\mathbf{r'}\,|) dS' + \frac{1}{j\omega\varepsilon_1} \nabla \iint_S \nabla' \mathbf{J}_1(\mathbf{r'}) G_1(|\,\mathbf{r}-\mathbf{r'}\,|) dS'$$

$$+ \nabla \times \iint_S \mathbf{M}_1(\mathbf{r'}) G_1(|\,\mathbf{r}-\mathbf{r'}\,|) dS' - j\omega\mu_2 \iint_S \mathbf{J}_2(\mathbf{r'}) G_2(|\,\mathbf{r}-\mathbf{r'}\,|) dS'$$

$$- \frac{1}{j\omega\varepsilon_2} \nabla \iint_S \nabla' \mathbf{J}_2(\mathbf{r'}) G_2(|\,\mathbf{r}-\mathbf{r'}\,|) dS' - \nabla \times \iint_S \mathbf{M}_2(\mathbf{r'}) G_2(|\,\mathbf{r}-\mathbf{r'}\,|) dS'] = \hat{n} \times \mathbf{E}^{inc} \quad (2.60)$$

and second, the boundary conditions for the magnetic field $\hat{n} \times \mathbf{H}_1 = \hat{n} \times \mathbf{H}_2$,

$$\hat{n} \times [j\omega\varepsilon_1 \iint_S \mathbf{M}_1(\mathbf{r'}) G_1(|\,\mathbf{r}-\mathbf{r'}\,|) dS' - \frac{1}{j\omega\mu_1} \nabla \iint_S \nabla' \mathbf{M}_1(\mathbf{r'}) G_1(|\,\mathbf{r}-\mathbf{r'}\,|) dS'$$

$$- \nabla \times \iint_S \mathbf{J}_1(\mathbf{r'}) G_1(|\,\mathbf{r}-\mathbf{r'}\,|) dS' - j\omega\varepsilon_2 \iint_S \mathbf{M}_2(\mathbf{r'}) G_2(|\,\mathbf{r}-\mathbf{r'}\,|) dS'$$

$$+ \frac{1}{j\omega\mu_2} \nabla \iint_S \nabla' \mathbf{M}_2(\mathbf{r'}) G_2(|\,\mathbf{r}-\mathbf{r'}\,|) dS' + \nabla \times \iint_S \mathbf{J}_2(\mathbf{r'}) G_2(|\,\mathbf{r}-\mathbf{r'}\,|) dS'] = \hat{n} \times \mathbf{H}^{inc} \quad (2.61)$$

To simplify notation, and build the integro-differential equations system, let us recall equations (2.60) and (2.61) by using the following operators

$$L_e(\mathbf{J}) = j\omega\mu_1 \iint_S \mathbf{J}(\mathbf{r'})G_1(|\,\mathbf{r}-\mathbf{r'}\,|)dS' + \frac{1}{j\omega\varepsilon_1}\nabla \iint_S \nabla'\mathbf{J}(\mathbf{r'})G_1(|\,\mathbf{r}-\mathbf{r'}\,|)dS'$$

$$+ j\omega\mu_2 \iint_S \mathbf{J}(\mathbf{r'})G_2(|\,\mathbf{r}-\mathbf{r'}\,|)dS' + \frac{1}{j\omega\varepsilon_2}\nabla \iint_S \nabla'\mathbf{J}(\mathbf{r'})G_2(|\,\mathbf{r}-\mathbf{r'}\,|)dS' \tag{2.62}$$

$$C(\mathbf{M}) = \nabla \times \iint_S \mathbf{M}(\mathbf{r'})G_1(|\,\mathbf{r}-\mathbf{r'}\,|)dS' + \nabla \times \iint_S \mathbf{M}(\mathbf{r'})G_2(|\,\mathbf{r}-\mathbf{r'}\,|)dS' \tag{2.63}$$

$$C(\mathbf{J}) = -\nabla \times \iint_S \mathbf{J}(\mathbf{r'})G_1(|\,\mathbf{r}-\mathbf{r'}\,|)dS' - \nabla \times \iint_S \mathbf{J}(\mathbf{r'})G_2(|\,\mathbf{r}-\mathbf{r'}\,|)dS' \tag{2.64}$$

$$L_m(\mathbf{M}) = j\omega\varepsilon_1 \iint_S \mathbf{M}(\mathbf{r'})G_1(|\,\mathbf{r}-\mathbf{r'}\,|)dS'$$

$$- \frac{1}{j\omega\mu_1}\nabla \iint_S \nabla'\mathbf{M}(\mathbf{r'})G_1(|\,\mathbf{r}-\mathbf{r'}\,|)dS' + j\omega\varepsilon_2 \iint_S \mathbf{M}(\mathbf{r'})G_2(|\,\mathbf{r}-\mathbf{r'}\,|)dS'$$

$$- \frac{1}{j\omega\mu_2}\nabla \iint_S \nabla'\mathbf{M}(\mathbf{r'})G_2(|\,\mathbf{r}-\mathbf{r'}\,|)dS' \tag{2.65}$$

where they have been expressed in terms of one equivalent current $\mathbf{J} = \mathbf{J}_1 = -\mathbf{J}_2$ and $\mathbf{M} = \mathbf{M}_1 = -\mathbf{M}_2$, considering equations (2.50) and (2.51). With this, we arrive at the following matrix expression

$$\begin{bmatrix} L_e & -C \\ C & L_m \end{bmatrix} \begin{bmatrix} \mathbf{J} \\ \mathbf{M} \end{bmatrix}_{tan} = \begin{bmatrix} \mathbf{E}^{inc} \\ \mathbf{H}^{inc} \end{bmatrix}_{tan} \tag{2.66}$$

The subscript *tan* means the tangential components on the surface. For the characteristic mode analysis, the matrix operator in (2.66) has to be symmetric, otherwise the characteristic mode solutions would be generally complex-valued. That is why, (2.66) takes the following form,

$$\begin{bmatrix} L_e & -jC \\ -jC & L_m \end{bmatrix} \begin{bmatrix} \mathbf{J} \\ j\mathbf{M} \end{bmatrix}_{tan} = \begin{bmatrix} \mathbf{E}^{inc} \\ j\mathbf{H}^{inc} \end{bmatrix}_{tan} \tag{2.67}$$

The introduction of the imaginary number was first introduced by Chang and Harrington in [29]. Equation (2.67) is simply the usual linear system operator equation expressed below:

$$T(\mathbf{f}) = \mathbf{g}^{inc} \tag{2.68}$$

where the subscript "*tan*" have been dropped for brevity. In (2.68),

$$T = \begin{bmatrix} L_e & -jC \\ -jC & L_m \end{bmatrix}; \quad \mathbf{f} = \begin{bmatrix} \mathbf{J} \\ j\mathbf{M} \end{bmatrix}; \quad \mathbf{g}^{inc} = \begin{bmatrix} \mathbf{E}^{inc} \\ j\mathbf{H}^{inc} \end{bmatrix} \tag{2.69}$$

Being T the operator tangent to the surface of the object, $\mathbf{f}$ the current vector, and $\mathbf{g}^{inc}$ the incident field vector. Let's now define the symmetric product

$$\langle \mathbf{f}, \mathbf{g} \rangle = \iint_S \mathbf{f} \bullet \mathbf{g} \, dS' \tag{2.70}$$

This inner product reduces the components of the matrix operator to submatrices in the matrix operator, in the same way as for the Galerkin MoM procedure when using the same expansion and testing basis functions. On the other hand, $\langle \mathbf{f}^*, \mathbf{g} \rangle$ is a suitable inner product for the Hilbert space functions $\mathbf{f}$ and $\mathbf{g}$ on S'. By reciprocity, it is easy to show that T is symmetric, $\langle \mathbf{f}_1, T\mathbf{f}_2 \rangle = \langle T\mathbf{f}_1, \mathbf{f}_2 \rangle$. The operator T can be expressed in terms of its hermitian parts as $T = T_1 + jT_2$ where

$$T_1 = \frac{1}{2}(T + T^*) = \begin{bmatrix} R & N_1 \\ N_1 & G \end{bmatrix} \tag{2.71}$$

$$T_2 = \frac{1}{2j}(T - T^*) = \begin{bmatrix} X & N_2 \\ N_2 & B \end{bmatrix} \tag{2.72}$$

So, considering the same definition of the generalized eigenvalue equation presented in (2.8) and (2.37), here we have

$$[T_2][\mathbf{f}_n] = \lambda_n [T_1][\mathbf{f}_n] \tag{2.73}$$

In (2.73), both the characteristic eigenvalues λ_n and eigencurrents $\mathbf{f}_n$ are defined to be real valued. The characteristic mode basis function is defined as

$$\mathbf{f}_n = \begin{bmatrix} \mathbf{J}_n \\ j\mathbf{M}_n \end{bmatrix} \tag{2.74}$$

where $\mathbf{J}_n$ and $\mathbf{M}_n$ are the basis functions determining the electric and magnetic equivalent characteristic currents. The characteristic currents can be normalized to radiate unit power using the following orthogonality relations

$$\langle \mathbf{f}_m, T(\mathbf{f}_n) \rangle = \langle \mathbf{f}_m^*, T(\mathbf{f}_n) \rangle = (1 + j\lambda_n)\delta_{m,n} \tag{2.75}$$

$$\langle \mathbf{f}_m, T_1(\mathbf{f}_n) \rangle = \langle \mathbf{f}_m^*, T_1(\mathbf{f}_n) \rangle = \delta_{m,n} \tag{2.76}$$

$$\langle \mathbf{f}_m, T_2(\mathbf{f}_n) \rangle = \langle \mathbf{f}_m^*, T_2(\mathbf{f}_n) \rangle = \lambda_n \delta_{m,n} \tag{2.77}$$

where $\delta_{m,n}$ is the Kronecker delta. Once the eigenvalues λ_n are obtained, the expression for the modal significance, MS, is the same as for metals, equation (2.12).

The complete definition for the characteristic eigenvalues is not presented in [28]. In fact, Chang and Harrington mentioned that many questions were still left unanswered in the interpretation of the characteristic modes to material objects. The interpretation of these solutions will be one of the purposes of this thesis.

2.4.2 Modal Solutions

After having introduced the eigenvalue and eigenfunction definitions, the total equivalent current can be defined on the body surface as

$$\mathbf{f} = \sum_n \alpha_n \mathbf{f}_n \tag{2.78}$$

where α_n are the excitation coefficients of the characteristic currents $\mathbf{f}_n$. In order to obtain the definition for α_n, (2.78) has to be substituted in (2.68), and the resulting equation after multiplying by the weight function $\mathbf{f}_m$ is

$$\sum_n \alpha_n \langle \mathbf{f}_m, T(\mathbf{f}_n) \rangle = \langle \mathbf{f}_m, \mathbf{g}^{inc} \rangle \tag{2.79}$$

Next, the orthogonality condition (2.75) is also applied to (2.79), and α_n takes the same form as in previous sections for both conducting and dielectric bodies

$$\alpha_n = \frac{\langle \mathbf{f}_n, \mathbf{g}^{inc} \rangle}{(1 + j\lambda_n)} \tag{2.80}$$

where

$$\langle \mathbf{f}_n, \mathbf{g}^{inc} \rangle = \iint_S \left(\mathbf{J}_n \mathbf{E}^{inc} - \mathbf{M}_n \mathbf{H}^{inc} \right) dS' \tag{2.81}$$

On the other hand, the fields can be calculated through these results. Let us define a field produced by a characteristic eigencurrent $\mathbf{f}_n$

$$\mathbf{g} = \sum_n \alpha_n \mathbf{g}_n \tag{2.82}$$

As can be seen, the total field distribution can also be expressed as a sum of the characteristic fields $\mathbf{g}_n$ and its corresponding excitation coefficients α_n. These coefficients are the same as the calculated for the total current distribution

(2.80). Moreover, the characteristic fields are composed by the electric and magnetic fields, $\mathbf{E}_n$ and $\mathbf{H}_n$, respectively.

$$\mathbf{g}_n = \begin{bmatrix} \mathbf{E}_n \\ j\mathbf{H}_n \end{bmatrix} \tag{2.83}$$

In the radiation zone, the characteristic fields $\mathbf{E}_n$ and $\mathbf{H}_n$ are known as characteristic far fields, and only there, they satisfy the following orthogonality relation,

$$\frac{1}{\eta}\iint_{S_\infty} \mathbf{E}_m^* \mathbf{E}_n dS' = \eta \iint_{S_\infty} \mathbf{H}_m^* \mathbf{H}_n dS' = \delta_{m,n} \tag{2.84}$$

where S_∞ is the sphere at infinity.

Chapter 3

Analysis of Resonances on PEC Bodies

In this chapter, some aspects in the interpretation of the solutions provided by the TCM of a PEC infinite circular cylinder and a PEC sphere are presented. Firstly, natural resonances (NRs) and characteristic mode resonances (CMRs) are introduced and compared. Secondly, characteristic eigenvalues are used to find those NRs considering complex *ka* values. These analysis are firstly done for the infinite circular cylinder, and after for the PEC sphere. It will be seen that both the 2D (cylinder) and 3D (sphere) analysis provide the same conclusions.

On the other hand, another analysis will be presented. By linking the standard and the generalized eigenvalue problems a relation between NRs and characteristic mode eigenvalues is shown. Moreover, the thesis stating that external CMR does not imply maximum field scattering, or maximum current distribution, is also demonstrated.

Furthermore, the internal resonances of the characteristic mode eigenvalues are studied to obtain the dispersion curve of a circular PEC waveguide. For this study, the EFIE considering oblique incidence have been solved. Finally, the overall conclusions drawn in this chapter will be presented and some open question will be proposed.

The results provided in this chapter will help to better understand CMs in dielectric bodies.

3.1 Introduction

NRs are well known in the field of target identification. They are aspect independent, depending only on the intrinsic properties of the target and the surrounding media. This makes them a good tool for detection and discrimination in radar applications. In practice, NRs are extracted from the late time responses of impinging electromagnetic waves. This can be done using some well known theoretical procedures to extract the poles related with the target. Some of the main techniques for pole extraction are the Singularity Expansion Method (SEM) [16], the Prony's method [82], the Matrix Pencil (MP) method [103], and the Cauchy's method [72]. These methods are also used to extract poles from the radiated fields. An alternative approach, similar to SEM, would be to determine the NRs by searching for the zeros of the determinant of the MoM matrix in the complex frequency plane, [50, 66]. Or, equivalently, to find these zeros using a standard eigenvalue problem (SEP), where natural eigenmodes and natural eigenfrequencies are computed. This method is called eigenmode expansion method (EEM), and it was introduced by Baum in [13]. All methods mentioned above provide the same set of resonances. These NRs are in general complex numbers and are also known as complex natural resonances (CNRs). NRs can be classified into internal or external to the body under consideration. Internal resonances are merely cavity resonances caused by the internal waves experiencing multiple internal reflections. External resonances, however, are caused by creeping waves propagating along the body surface with attenuation due to the continuous radiation in the tangent direction. It is worth recalling that, unlike external, internal resonances are pure real numbers because they are undamped, representing those solutions that can not radiate outside the PEC cavity.

Along with these resonances, the TCM is being widely used lately to find other type of modes and resonances. However, there are still unknown aspects in the interpretation of the resulting CMRs. Interestingly, as for NRs, CMRs can also be classified into internal or external. As explained in [54], when an eigenvalue is zero or infinite, the corresponding CM is resonating externally or internally to the object, respectively. Therefore, in order to interpret these solutions, it is interesting to look at the NRs since they are unique, regardless of the technique considered to compute them or the formulation employed, [70]. In fact, to relate both procedures in which the NRs and the CMRs are found, it is a matter which has not been yet determined, and it was first proposed by

Baum in [14], where he quoted "*More work is needed to further explore these relations*".

Regarding to open PEC bodies, as dipoles or planar antennas, the TCM proves to be a useful method for antenna design. This happens because the resonance frequencies of the CMs and the natural modes are very close to each other. Therefore, CMA is considered a good candidate for the design of this type of antennas. Although this relation has not been studied before, this introduction presents a result that shows the close vicinity of both families of resonances, and the relatively low damping observed in its resonances, in comparison with the closed PEC bodies examined later. Therefore, what is presented next has been carried out with the only purpose of clarifying that there is a small difference between both types of resonances for open bodies. And this illustrates that different methods provide different resonance frequencies.

Let us firstly look for the NRs of a relatively thin straight wire, with $d/L = 0.01$, as an example:

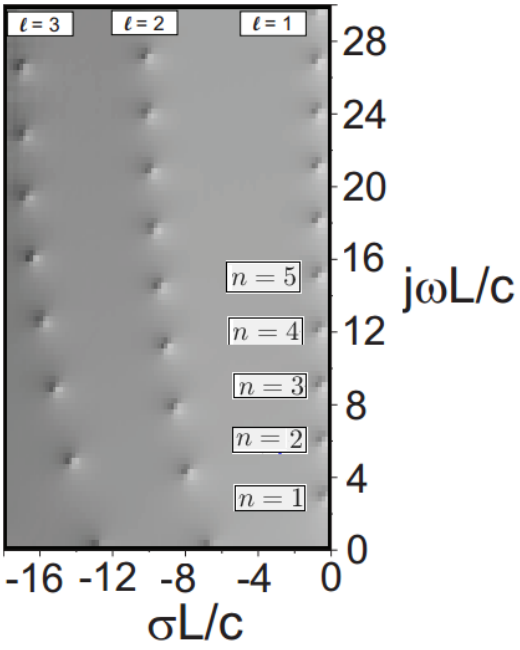

Fig. 3.1 Natural resonances for a straight wire considering $d/L = 0.01$ extracted from [111] .

Fig. 3.1 shows the natural resonances extracted from [111]. Note that the frequency axes have been normalized as $j\omega L/c$ and $\sigma L/c$, where a complex wave number has been used, $k = \omega/c + j\sigma/c$. These resonances have been obtained by making zero the determinant of the method of moment matrix. Another interesting observation is that natural resonances occur in layers $l = 1$, $l = 2$, and so on. Moreover, the modes of the first layer are named as $n = 1$, $n = 2$, etc.

Let us see now the characteristic eigenvalues of the same straight wire. Note that the frequency x-axis in Fig. 3.2 is normalized as kL, i.e., in this case $kL = \omega L/c$. The characteristic eigenvalues for each mode are differentiated as $n = 1$, $n = 2$, etc. When $\lambda_n = 0$ the characteristic mode is in an external CMR.

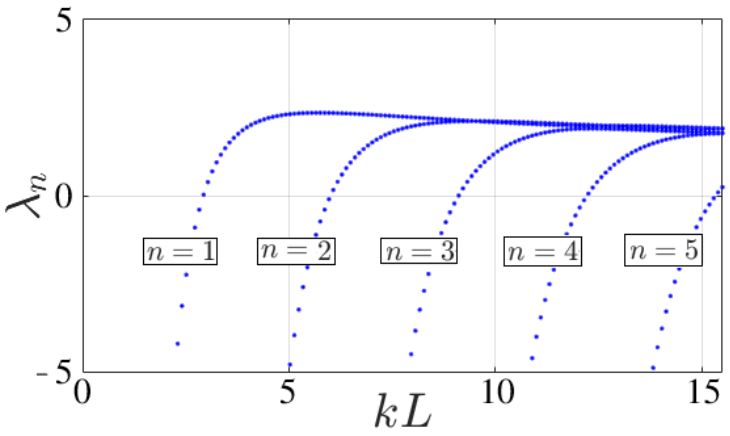

Fig. 3.2 Characteristic mode eigenvalues for a straight wire considering $d/L = 0.01$.

In order to compare both types of resonances, Table 3.1 shows some of the resonance frequencies obtained from Fig. 3.1 and Fig. 3.2 [111], and its percentage difference Δ.

Table 3.1 shows that there is a small difference Δ between the CMRs and the NRs. Δ decreases as the order mode n increases. As can be seen in Fig. 3.1, the damping factor increases as the order mode increases. Thus, as the order of the mode increases, the damping increases with it, and the percentage difference between both families of resonances decreases. So therefore, this is the clearer example in open PEC bodies where the difference between NRs and CMRs can

Table 3.1 A comparison between some of the resonant frequencies provided by the characteristic eigenvalues and the NRs

n	CMR	NR	$\Delta(\%)$
1	2.927	2.873	1.87
2	6.011	5.931	1.29
3	9.110	9.010	1.10
4	12.221	12.101	0.99
5	15.334	15.196	0.90

be seen. Another conclusion is that CMRs can only be compared with the first layer of the NRs since they are the closest to the $j\omega L/c$ axis.

In addition, it can also be seen from Fig. 3.1 that all NRs are external, since there are no resonances on the $j\omega L/c$ axis, which would be internal resonances in that case. This happens because the straight wire is not a cavity and all natural modes are leaking. As far as we know, the same is true for other types of open PEC structures, e.g., patch antennas. And this is why the TCM works very well for the design of planar antennas. However, we must be clear that both methods provide different resonances and that, therefore, **the CMs are not the natural modes**.

Concerning to PEC cavities, things work differently. Although some efforts have been made in the past to establish the relation between NRs and CMRs. In [21] and [5] it was shown that internal cavity NRs coincide with internal CMRs. However, although external CMRs were also mentioned in [21], no discussion was provided on the relation between them and external NRs. As for [5], wrong conclusions were drawn. Moreover, in [99] it was wrongly stated that NRs are the zeros of the eigenvalues of the governing equation in CMA, (2.8). Furthermore, Sarkar et al. recently published some insightful explanations about CMs and its resonances [102]. Building on that analysis, we present here some additional statements supporting the ideas from Sarkar and coauthors.

For that purpose, in this chapter, some aspects in the interpretation of the CM solutions for a PEC infinite circular cylinder and a PEC sphere are presented. Firstly, NRs and CMRs are compared. Secondly, it is observed that NRs can be obtained from characteristic eigenvalues when complex ka-plane is considered. Furthermore, by linking standard and generalized eigenvalue problems, a mathematical relation between NRs and characteristic eigenvalues

is found and presented. In addition, the thesis stating that external CMRs does not imply maximum field scattering [102], is also demonstrated. Furthermore, this chapter presents a new approach to finding the $\beta - \omega$ diagram for the circular PEC waveguide through the CMRs. This has been done by analytically solving the EFIE formulation considering the propagation constant k_z.

3.2 Natural Modes vs Characteristic Modes: A Definition

Consider a PEC scatterer illuminated by an incident electric field, $\mathbf{E}^i$. This incident field induces an electric current distribution $\mathbf{J}$ flowing on the PEC surface that radiates a scattered field $\mathbf{E}^s$. After imposing the boundary conditions for the tangential field on the PEC surface, and considering that the scattered field can be expressed as $\mathbf{E}^s = -Z(\mathbf{J})$ the problem to be solved can be written from the functional defined by the electric field integral equation (EFIE), (2.2.1).

$$Z(\mathbf{J}(\mathbf{r},\omega)) = \mathbf{E}^i(\mathbf{r},\omega) \tag{3.1}$$

Where the functional relation Z is

$$Z(\mathbf{J}(\mathbf{r},\omega)) = -\frac{j\omega\mu}{4\pi}\iint_S \mathbf{J}(\mathbf{r'})\frac{e^{jk|\mathbf{r}-\mathbf{r'}|}}{|\,\mathbf{r}-\mathbf{r'}\,|}dS' + \frac{1}{4\pi j\omega\varepsilon}\nabla\iint_S \nabla'\mathbf{J}(\mathbf{r'})\frac{e^{jk|\mathbf{r}-\mathbf{r'}|}}{|\,\mathbf{r}-\mathbf{r'}\,|}dS' \tag{3.2}$$

In (3.2), $\mathbf{r}$ denotes the observation point, $\mathbf{r'}$ the source point, S the scattering surface, ω the angular frequency, and μ, ε and k the permeability, permittivity, and the wavenumber, respectively. Equation (3.1) is solved for the current $\mathbf{J}$ through the inverse of the impedance operator. That is $\mathbf{J}(\mathbf{r},\omega) = Z^{-1}\mathbf{E}^i(\mathbf{r},\omega)$.

The resonance problem considered in this work is formulated in (3.3), where no excitation is applied, i.e., $\mathbf{E}^i(\mathbf{r},\omega) = 0$. Equation (3.3) defines the natural frequencies and natural modes of the target involved in the scattering process,

$$Z(\mathbf{J}(\mathbf{r},\omega)) = 0 \tag{3.3}$$

This means that one seeks for the nontrivial solutions of (3.3), which requires to find the solutions for which Z is a singular operator. This generally occurs at an infinite number of discrete complex frequencies, known as natural frequencies, $\omega = \omega' + j\omega''$. Where ω' provides the natural resonant frequency of a given natural mode, and ω'' its damping factor. The damping factor is linked to the radiating properties of a given mode.

To find the singularities of the Z operator one can seek for the zeros of the eigenvalues of the SEP presented by equation (3.4), i.e., $\nu_n = 0$. Or, equivalently, to solve for $det(Z) = 0$, being Z a matrix operator, since $det(Z) = \prod_n \nu_n$.

$$Z\mathbf{I}_n(\mathbf{r},\omega) = \nu_n \mathbf{I}_n(\mathbf{r},\omega) \tag{3.4}$$

In (3.4), $\mathbf{I}_n$ is the natural basis or the natural modes. It is important to note that both $\mathbf{I}_n$ and ν_n **are generally complex**, except for the related inner solutions. From this natural base, it is possible to construct the total current distribution $\mathbf{J}$ as

$$\mathbf{J}(\mathbf{r},\omega) = \sum_n \frac{\left\langle \mathbf{I}_n(\mathbf{r},\omega), \mathbf{E}^i \right\rangle}{\nu_n \left\langle \mathbf{I}_n(\mathbf{r},\omega), \mathbf{I}_n(\mathbf{r},\omega) \right\rangle} I_n(\mathbf{r},\omega) \tag{3.5}$$

This method is known as eigenfunction expansion method (EEM). More details can be found in [13].

Total current $\mathbf{J}(\mathbf{r},\omega)$ can be expanded in terms of so-called characteristic modes as well. When using CMA, it is not necessary to resort to complex frequencies and complex eigenvalues and eigenvectors to find the same $\mathbf{J}(\mathbf{r},\omega)$. Unlike the physical solutions provided by the EEM, CMA provides a mathematical basis with some interesting properties facilitating their manipulation and understanding when designing antennas or scatterers. CMA exploits the mathematical properties of the Z operator **to obtain real eigenvalues and eigenmodes**. Since $Z = R + jX$ is a complex symmetric operator, its real and imaginary parts, R and X, are hermitian matrices. The following generalized or

weighted eigenvalue problem defines the characteristic eigenvalues, λ_n, and the characteristic eigencurrents, $\mathbf{J}_n$.

$$X\mathbf{J}_n(\mathbf{r},\omega) = \lambda_n R\mathbf{J}_n(\mathbf{r},\omega) \tag{3.6}$$

Remembering the theory presented in Chapter 2, by definition, the characteristic eigenvalues, λ_n, range from $-\infty$ to $+\infty$. Furthermore, if $\lambda_n > 0$, the corresponding modes have predominantly magnetic stored energy (inductive modes), while if $\lambda_n < 0$ they have electric stored energy (capacitive modes). A mode having $\lambda_n = \pm\infty$ is called an internally resonant mode (cavity mode). And a mode having $\lambda_n = 0$ is called an externally resonant mode. The modes corresponding to external resonances are those considered in antenna and scatterer design.

Electric Current $\mathbf{J}$ can be also obtained from the expansion of their characteristic eigensolutions as

$$\mathbf{J}(\mathbf{r},\omega) = \sum_n \frac{\left\langle \mathbf{J}_n(\mathbf{r},\omega), \mathbf{E}^i \right\rangle}{(1+j\lambda_n)\left\langle \mathbf{J}_n(\mathbf{r},\omega), \mathbf{J}_n(\mathbf{r},\omega) \right\rangle} \mathbf{J}_n(\mathbf{r},\omega) \tag{3.7}$$

From the antenna design point of view, having real solutions become more practical than complex ones because they are easier to interpret. In fact, real modes are described as standing waves which have fixed stationary nodes. On the other hand, complex modes are described as travelling waves and appear to have moving nodes on the structure. Thus, since for antenna design it is interesting to know where to place the power supply to drive a particular electromagnetic mode, the characteristic modes facilitates the design to the engineers unlike the conventional design method, or the EEM, because whatever the geometric shape of the antenna is, a set of orthogonal and real modes can be obtained.

3.3 The Infinite PEC Circular Cylinder

In this section, NRs and CMRs for a PEC infinite circular cylinder are compared when considering the EFIE impedance operator. For this purpose, the well known analytical formulas to express the EFIE operator for TM^z and TE^z polarizations are used [90, 114]. Equations (3.8) and (3.9) can be analytically calculated from the procedure presented in Appendix A.1.

$$Z^{EFIE,\,TM_n^z} = \frac{\eta\pi ka}{2} J_n(ka)\, H_n^{(2)}(ka) \tag{3.8}$$

$$Z^{EFIE,\,TE_n^z} = \frac{\eta\pi ka}{2} J_n'(ka)\, H_n'^{(2)}(ka) \tag{3.9}$$

In (3.8) and (3.9) a is the cylinder radius, $H_n^{(2)}(x)$ the Hankel functions of second kind, $J_n(x)$ the Bessel functions of first kind, n the azimuthal mode order ($n = 0, 1, 2, 3...$), k the wavenumber, and η the intrinsic impedance. The primes on the Bessel and Hankel functions denote differentiation with respect to the entire argument.

3.3.1 Natural Resonances

NRs are extracted from the zeros of the determinant of the impedance matrix operator. Thus, concerning the PEC infinite circular cylinder, equations (3.8) and (3.9) have to be equal to zero. Some of the first natural resonances are shown in Fig. 3.3.

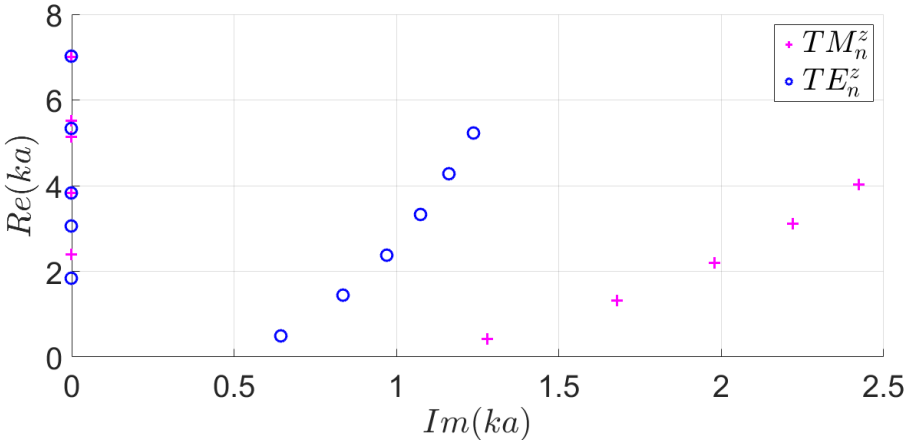

Fig. 3.3 Natural resonances of the infinite PEC circular cylinder.

TM_n^z and TE_n^z resonances are marked with "+" and "∘", respectively. Considering the conclusions presented in [30] for the PEC sphere, the same can be

concluded here: NRs in Fig. 3.3 can be separated into internal (cavity modes) and external (surface modes or creeping waves) NRs.

The internal NRs are those located on the real axis and the external ones are complex numbers. The imaginary part of these complex numbers (surface modes) provides surface mode ability to radiate (radiation losses). Unlike the surface modes, cavity modes do not radiate and that is why their resonances are pure real numbers. Just for the sake of completeness, let us add that these cavity resonances are transverse resonances and they are the cut-off frequencies of the corresponding circular waveguide modes, i.e., $J_n(ka) = 0$ (TM_n^z modes) and $J_n'(ka) = 0$ (TE_n^z modes). This means that looking at equations (3.8) and (3.9), external resonances can be calculated from $H_n^{(2)}(ka) = 0$ (TM_n^z modes) and $H_n'^{(2)}(ka) = 0$ (TE_n^z modes). External NRs are due to those surface waves that circumnavigate the cylinder surface matching their phases so as to build up to the resonance by constructive interference.

From the viewpoint of radar scattering, these external NRs can also be approximately calculated from the radar cross section (RCS). The difference between the NRs and the RCS spectrum is that the information in the RCS spectrum is not as complete as that in the natural frequency spectrum [12]. Since resonant peaks in RCS plot do occur at real frequencies at which the zeros of equations (3.8) and (3.9) are not zero, i.e., the natural resonances are not excited. Furthermore, the RCS spectrum is partially a function of the angle of incidence and polarization. Nevertheless, a good agreement is observed in most cases for the real frequency pole coordinates when compared to the RCS spectrum and physical information can be obtained from it, [86]. These comments will serve to better understand the subsection where NRs and CMRs are compared.

3.3.2 Characteristic Mode Resonances

CMRs are obtained from the GEP presented below [54]

$$X\mathbf{J}_n = \lambda_n R\mathbf{J}_n \tag{3.10}$$

where X and R are the imaginary and real part of the EFIE impendance matrix operator , ($Z = R + jX$), $\mathbf{J}_n$ the characteristic currents, and λ_n the characteristic eigenvalues. By definition, $\lambda_n = 0$ and $\lambda_n = \pm\infty$ (asymptotic behavior) are being interpreted as external and internal CMRs, respectively.

Concerning the infinite PEC cylinder, characteristic eigenvalues can be found substituting equations (3.8) and (3.9) into (3.10). The analytical results for their associated eigenvalues are

$$\lambda_n^{TM_n^z} = -\frac{Y_n(ka)}{J_n(ka)} \tag{3.11}$$

$$\lambda_n^{TE_n^z} = -\frac{Y_n'(ka)}{J_n'(ka)} \tag{3.12}$$

Equations (3.11) and (3.12) can be also found in [49]. They are graphed in Fig. 3.4.

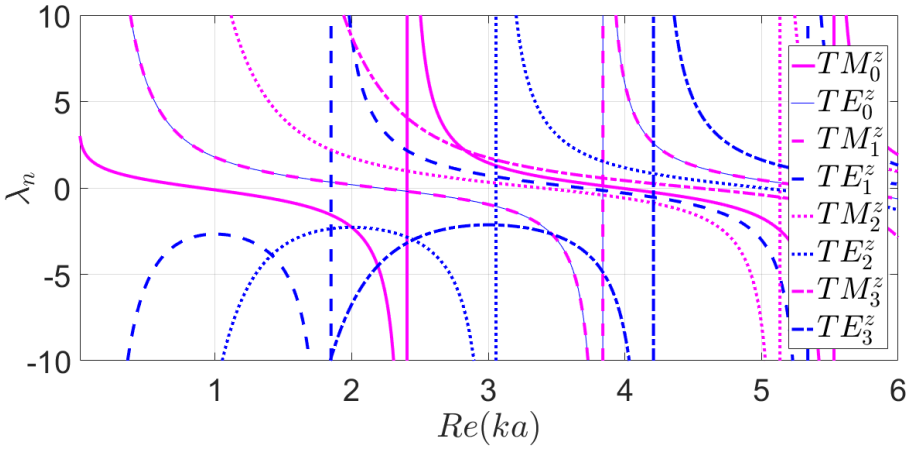

Fig. 3.4 Characteristic eigenvalues of the infinite PEC circular cylinder.

Let us consider for instance the TM_n^z characteristic eigenvalues. Observing equation (3.11) in Fig. 3.4, it can be clearly seen that the zero crossings of λ_n correspond with the zeros of the Neumann function, $Y_n(ka)$. Moreover, when $\lambda_n = \pm\infty$ (asymptotic behavior), it corresponds with the zeros of the Bessel function, $J_n(ka)$. Therefore, $Y_n(ka) = 0$ and $J_n(ka) = 0$ provide the external and internal CMRs, respectively. Furthermore, it is also important to note that in λ_n curves, each asymptote is located between two consecutive zeros. The consecutive asymptotes provide the order of the radial variation of a given cavity mode, i.e., the corresponding λ_n for TM_0^z mode has $m = 1,2,3...$ asymptotes that are representing the cavity resonances with radial variations

Table 3.2 Comparison between external natural resonances and external characteristic modes resonances.

$Re(ka)$	Natural Resonances		Characteristic Mode Res.	
n	$TM_{n,1}$	$TE_{n,1}$	$TM_{n,1}$	$TE_{n,1}$
0	X	X	0.89	2.20
1	X	0.50	2.20	3.68
2	0.43	1.44	3.38	5.00
3	1.31	2.38	4.53	X
4	2.21	3.32	5.65	X

$TM^z_{0,m}$. They are for instance $TM^z_{0,1}$, $TM^z_{0,2}$, $TM^z_{0,3}$, and so on. Regarding the zero crossings of λ_n, they are simply solutions related with the zeros of the reactance operator X, as a result of using the GEP (3.4). As mentioned above, since we are dealing with a circular PEC infinite cylinder these zeros are exactly the zeros of the Neumann function. According to CMA, these are called external CMRs. Interestingly, they do not coincide with the external NRs, as it will be evidenced next. In fact, it will be shown that unlike for the straight wire, in PEC cavities the NRs and the CMRs are very far each other.

The same can be concluded for the TE^z_n characteristic modes, but considering equation (3.12). $Y'_n(ka) = 0$ and $J'_n(ka) = 0$ lead to external and internal CMRs, respectively.

3.3.3 Natural Resonances vs Characteristic Modes Resonances

With regard to internal resonances, it is obvious that both procedures lead to exactly the same results, since both are calculated from $J_n(ka) = 0$ (TM^z_n) and $J'_n(ka) = 0$ (TE^z_n). As for external resonances, Table 3.2 shows the corresponding values obtained from Fig. 3.3 and Fig. 3.4. Contrary to [5, 99], where it was stated that external NRs and CMRs were the same, here it is concluded that both methods provide quite different resonances. Notice that letter X on Table 3.2 is for points outside the graph region shown.

Nevertheless, it would be interesting to show whether characteristic eigenvalues (λ_n) are somehow capable of providing the external NRs. Notice, though, that external NRs involve complex ka values. However a complex argument should not be used directly on (3.11) or (3.12) because these equations were obtained by Garbacz assuming real ka values. That would lead to wrong solu-

tions. Instead, the proper thing to do is introducing complex *ka* values in (A.13) and (A.14) before solving equation (3.10). It is worth noting that λ_n remains a real number. The eigenvalues obtained for complex *ka* are shown in Fig. 3.5.

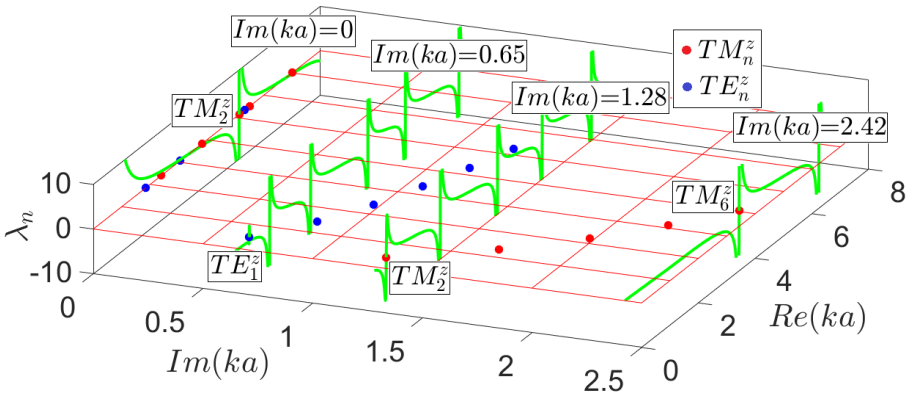

Fig. 3.5 Characteristic eigenvalues for different imaginary planes and the poles of the natural resonances.

A few resonances have been chosen for the sake of illustration. Fig. 3.5 shows a schematic correspondence between the characteristic eigenvalues (λ_n) obtained for a set of imaginary *ka* planes and the natural resonance poles for the PEC cylinder. The real part corresponds to the location of the resonant frequencies and the imaginary part to the damping factor. The imaginary *ka* planes selected contain external natural resonances of modes TE_1^z, TM_2^z and TM_6^z. These planes are $Im(ka) = 0.65, 1.28, 2.42$ (See fig. 3.3). Notice that each eigenvalue trace crosses zero or have an asymptote right at the natural resonance location. For $Im(ka) = 0$ plane, only the internal natural resonance of TM_2^z mode matches the eigenvalue trace. Therefore, now characteristic eigenvalues are able to provide the NRs. Along with the NRs, the λ_n curves plotted show other zero crossings and asymptotes. These are just due to singularities in *X* or *R* operators in equation (3.10) with no physical meaning, to the authors' knowledge.

3.4 The PEC Sphere

In this section, the analysis performed on the infinite circular PEC cylinder is briefly extended to the PEC sphere. The purpose of this analysis is not just exploring the relationship between CMRs and NRs for this particular canonical body, but demonstrating that the conclusions drawn from a 2D analysis can also be extended to 3D bodies. To this purpose, the following analytical solutions obtained from the EFIE are used here, [113],

$$Z^{EFIE,\,TM_n^r} \propto \mathbb{J}'_n(ka)\,\mathbb{H}'^{(2)}_n(ka) \tag{3.13}$$

$$Z^{EFIE,\,TE_n^r} \propto \mathbb{J}_n(ka)\,\mathbb{H}^{(2)}_n(ka) \tag{3.14}$$

Where $\mathbb{J}_n(ka)$ and $\mathbb{H}^{(2)}_n(ka)$ are Riccati-Bessel and Riccati-Hankel functions defined in [1], respectively. a is the sphere radius, n the azimuthal mode order ($n = 1, 2, 3...$), and k the wavenumber. The primes on the Riccati's functions denote differentiation with respect to the entire argument. Note that equations (3.13) and (3.14) are written using the proportionality symbol "$\propto$", since there exist some proportionality constants, but for the purpose of this section it is enough to express the equations in this way.

The first difference to note between the cylinder and the sphere is that unlike for the cylinder, where the electromagnetic modes are transverse to the z-axis, for the sphere they are transverse to the radial direction, r. Furthermore, there is also a mathematical relationship between the functions defined in the coordinate systems used. While in the previous case they are cylindrical Bessel functions, in this case they are spherical Bessel functions, and the same occurs for the Hankel functions.

3.4.1 Natural Resonances

Since NRs are calculated making the $det(Z(ka)) = 0$, it is possible to extract the natural resonances either internal and/or external using the ka complex plane as done for the infinite circular cylinder. For the PEC sphere case, making use of the equations (3.13) and (3.14) the internal NRs can be calculated doing $\mathbb{J}_n(ka) = 0$ and $\mathbb{J}'_n(ka) = 0$, and the external NRs making $\mathbb{H}^{(2)}_n(ka) = 0$ and $\mathbb{H}'^{(2)}_n(ka) = 0$. These solutions are presented in Fig. 3.6.

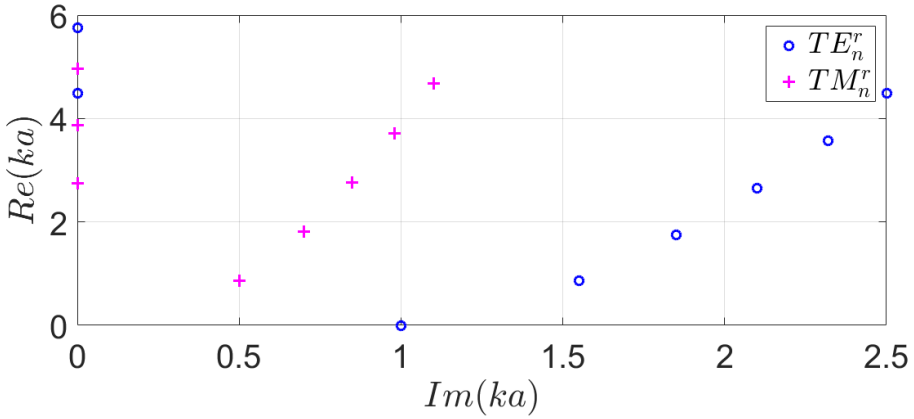

Fig. 3.6 Natural resonances of the PEC sphere.

Fig. 3.6 shows the NRs for a PEC sphere. TE_n^r and TM_n^r resonances are marked by "$\circ$" and "$+$", respectively. As for the cylinder, the real and imaginary parts of the NRs define the resonant frequency and the damping factor, respectively. Moreover, the same conclusions can be drawn for the PEC sphere. Internal NRs can be found on the real *ka* axis, and external NRs are located in the *ka* complex plane. As mentioned in the previous section, only internal resonances are completely real because there is no leakage outside the sphere surface. These NRs could also be found considering the scattering coefficient singularities as presented in [30].

3.4.2 Characteristic Mode Resonances

Let us now consider the characteristic eigenvalues for the PEC sphere. Substituting equations (3.13) and (3.14) in equation (3.10), the characteristic eigenvalues (3.15) and (3.16) are obtained.

$$\lambda_n^{TM_n^r} = -\frac{\mathbb{Y}'_n(ka)}{\mathbb{J}'_n(ka)} \tag{3.15}$$

$$\lambda_n^{TE_n^r} = -\frac{\mathbb{Y}_n(ka)}{\mathbb{J}_n(ka)} \tag{3.16}$$

These eigenvalues were first analytically obtained by Garbacz in [49]. Fig. 3.7 shows the characteristic eigenvalues (3.15) and (3.16).

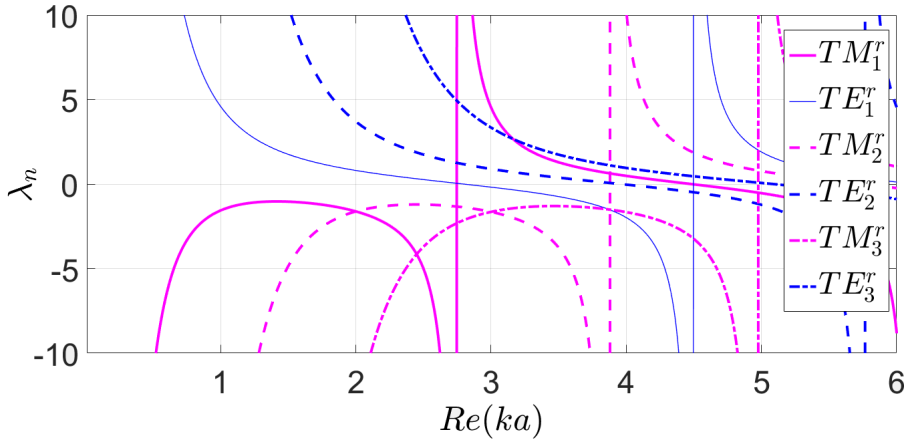

Fig. 3.7 Characteristic eigenvalues of the PEC sphere.

As defined for the cylinder, when $\lambda_n \to \pm\infty$ it represents an internal CMR. In contrast, when $\lambda_n = 0$ represents an external CMR. Thus, let us consider the case, for instance, in which a TE_n^z mode is being studied. Observing equation (3.16) in Fig. 3.7, it can be seen that the zero crossings of λ_n correspond with the zeros of the Riccati-Neumann function, $\mathbb{Y}_n(ka)$. On the other hand, when $\lambda_n \to \pm\infty$ (assymptotic behaviour), it corresponds with the zeros of the Riccati-Bessel function $\mathbb{J}_n(ka)$. Therefore, $\mathbb{Y}_n(ka)$ and $\mathbb{J}_n(ka)$ provide the external and internal CMRs, respectively. It is important to note that for a particular mode, either TE_n^r or TM_n^r, each asymptote represents the m-th order of the radial variation of a given cavity mode. For example, the corresponding λ_n for the TE_1^r mode has $m = 1,2,3,...$ asymptotes that are representing the cavity resonances with radial variation $TE_{1,m}^r$, i.e., $TE_{1,1}^r$, $TE_{1,2}^r$, $TE_{1,3}^r$, etc. With regard to the consecutive zero cuts of a given eigenvalue λ_n, they are generally understood as external CMRs. But as far as we know, they have no meaning for closed PEC cavities. Interestingly, in the same way as for the PEC cylinder, the external CMRs for the PEC sphere do not coincide with the external NRs, as it will be discussed in the next section.

The same conclusions can be reached for the TM_n^r characteristic modes but considering equation (3.15). Where $\mathbb{Y}'_n(ka) = 0$ and $\mathbb{J}'_n(ka) = 0$ provide the external and internal CMRs, respectively.

3.4.3 Natural Resonances vs Characteristic Modes Resonances

As concluded in the analysis for the PEC cylinder, the same can be said for the sphere with regard to the comparison between NRs and CMRs: only internal resonances coincide. Obviously, in both procedures internal resonances are found through the zeros of the Ricatti-Bessel functions $\mathbb{J}_n(ka)$ and $\mathbb{J}'_n(ka)$ for the TE_n^r and TM_n^r modes, respectively. So, that is the reason why they are the same.

As far as the external resonances are concerned, they are completely different. A proof of this can be seen from Table 3.3. It can be easily seen that they are clearly different. Table 3.3 shows the resonances obtained from Figs. 3.6 and 3.7.

Table 3.3 Comparison between external natural resonances and external characteristic modes resonances for the PEC sphere.

$Re(ka)$	Natural Resonances		Characteristic Mode Res.	
n	$TE_{n,1}$	$TM_{n,1}$	$TE_{n,1}$	$TM_{n,1}$
1	0	0.88	2.80	4.48
2	0.87	1.81	3.96	5.74
3	1.76	2.76	5.09	X

Since the external NRs are located in the complex ka plane, it is interesting to check whether it is possible to obtain them from the characteristic eigenvalues. To do so, an imaginary axis is needed to find the external NRs. Fig. 3.8 shows two cases in which the imaginary planes $Imag(ka) = 0.85$ (left) and $Imag(ka) = 0.69$ (right) have been considered to find the TE_3^r and TM_2^r external NRs (blue diamonds), respectively. Furthermore, it is interesting to mention that the characteristic eigenvalues are still real functions for complex ka values.

With these analysis it is demonstrated that NRs can be found with characteristic eigenvalues. Moreover, it is also demonstrated that external NRs and external CMRs are different again for the 3D case of the PEC sphere.

3.5 Geometrical Relation between NR and CMR

At this point, it is interesting to explain why external NRs and external CMRs are different. Furthermore, it is also important to explain their relation, since Baum was the first to introduce this question in [14].

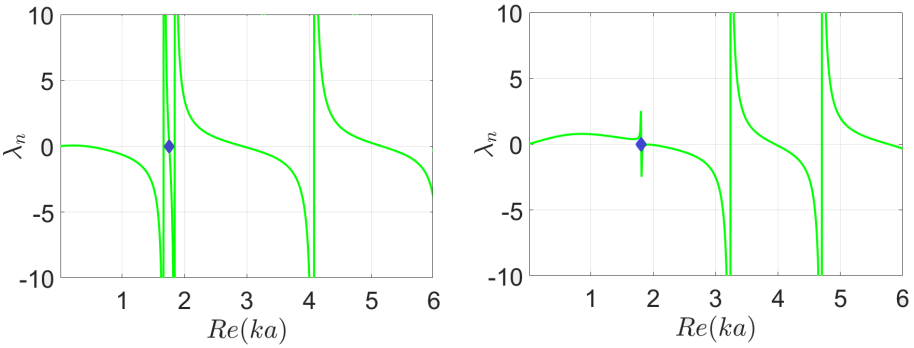

Fig. 3.8 External NRs found with the characteristic eigenvalues for two different cases. Left: TE_3, Imag(ka)=1.85. Right: TM_2 Imag(ka)=0.69. The blue diamonds correspond to the resonant frequency of each natural mode.

As presented by equation (3.1), the electric current $\mathbf{J}$ is related to $\mathbf{E}^i$ through the impedance operator Z as

$$Z(\mathbf{J}) = \mathbf{E}^i \tag{3.17}$$

Z is a symmetric complex matrix operator containing the geometrical and material information about the scatterer under study. Since the previous studies on the PEC cylinder and the PEC sphere show that the same conclusions can be drawn from the 2D and the 3D case, in this section we will stick to the PEC cylinder study.

In order to relate NRs with the resonances obtained from the characteristic eigenvalues, it is worth having a look to the standard eigenvalues obtained from the SEP (3.4),

$$Z\mathbf{I}_n = \nu_n \mathbf{I}_n \tag{3.18}$$

where $\mathbf{I}_n$ are the eigencurrents, and ν_n their associated eigenvalues. Since Z is a non-hermitian symmetric matrix, both, eigenvalues and eigenvectors, are generally complex. Since one seeks to solve the nontrivial solution for equation (3.17), $Z(\mathbf{J}) = 0$, natural resonances are calculated by forcing the determinant of the impedance matrix operator to vanish, but the same can be achieved from

the eigenvalues of the SEP (3.18) when they are set to zero, i.e., $\nu_n = 0$. Thus, **natural resonances can be found if and only if** $\nu_n = 0$.

Let us consider the TE_n^z solution of the infinite PEC circular cylinder as an example. Note that since equations (3.8) and (3.9) represent a diagonal impedance matrix operator, their associated impedance eigenvalues are exactly the same equations. Then, from the SEP viewpoint we have

$$\nu_n^{TE_n^z} = \frac{\eta \pi ka}{2} J_n'(ka) H_n'^{(2)}(ka) \tag{3.19}$$

In order to study the eigenimpedance $\nu_n^{TE_n^z}$, also known as characteristic impedance, it is interesting to separate it into its real and imaginary parts, $\nu_n = \alpha_n + j\beta_n$. Where α_n and β_n represent the resistance and the reactance, respectively. Characteristic impedance is commonly represented in polar coordinates as $\nu_n = |\nu_n| e^{j\phi_n}$. Where $|\nu_n| = \sqrt{\alpha_n^2 + \beta_n^2}$, and $\phi_n = arctan(\beta_n/\alpha_n)$ is the phase angle. This polar representation is called impedance diagram. Considering the TE_1^z mode from equation (3.19), its impedance diagram is presented in Fig. 3.9.

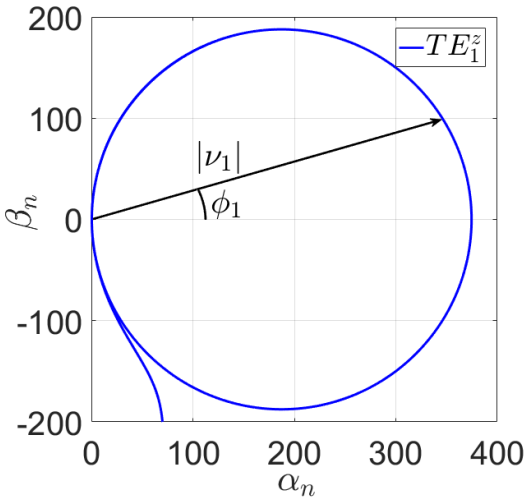

Fig. 3.9 Impedance diagram for the TE_1^z eigenimpedance.

In Fig. 3.9, α_n is plotted on the X-axis and β_n on the Y-axis. Each point represented by vector ν_n is the characteristic impedance at a given frequency. In

Fig. 3.9, frequency grows in the clockwise direction. As frequency increases, ν_1 is generating a circle. When $\nu_1 = 0$ it implies that $|\nu_1| = 0$ and $\phi_1 = \pi/2$ *or* $-\pi/2$. Only in this case (considering real *ka* values), the EFIE eigenvalue (3.19) breaks down giving an internal resonance. The internal resonance problem is explained in [91] and [114] from the numerical viewpoint, and it is also explained in [102] for the TM_n^z polarization considering characteristic modes. On the other hand, ν_1 experiences its minimum value ($\nu_1 = \alpha_1$) when $\phi_1 = 0$, indicating the cylinder impedance is purely resistive. Moreover, right at this frequency the cylinder is supposed to present a maximum value in its associated eigencurrent under study. Finally, when $\phi_1 > 0$ and $\phi_1 < 0$, the associated eigencurrent is behaving inductively and capacitively, respectively.

The analogy with the generalized equation governing characteristic modes (3.10) is that since equation (3.10) can also be expressed as $\alpha_n X\mathbf{J}_n = \beta_n R\mathbf{J}_n$, it is straightforward to write $\lambda_n = \beta_n/\alpha_n$. According to this, **it is concluded that the TCM diagonalizes the phase angle of the characteristic impedance**. That is why the information provided by λ_n is related with the energy storage of the scatterer under study, either inductive or capacitive, and the resonances, as defined in section 3.3.2. This makes clear that the relation between the eigenvalues obtained from the SEP and the GEP is

$$\nu_n = |\nu_n|\, e^{j\ arctan(\lambda_n)} \tag{3.20}$$

So, here is the relationship that helps to understand the difference between the two solutions, and also links them.

Going forward, the external NRs are not presented in Fig. 3.9 (only the internal ones), unless complex *ka* values were considered to achieve $\nu_n = 0$, as demonstrated in Fig. 3.5. Notice that at an external CMR, $\lambda_n = 0$. Thus, $\phi = 0$ and $\nu_n = |\nu_n|$ and at its corresponding frequency, the condition $\nu_n = 0$ is not accomplished and the maximum eigencurrent is not obtained. This simple reasoning contradicts the assumption done by other researchers that CMRs and NRs are equal, and also that CMs radiate maximum field when they are in resonance.

To finalize this discussion, let us explain what is happening in the total electric current and the scattered electric field at a *ka* value for which an external CM resonates. Since external resonances from characteristic eigenvalues do occur at real frequencies for which equations (3.8) and (3.9) are not singular,

the external NRs are not excited, i.e., the singularity condition $det(Z) = 0$ is not met. Thus, the maximum radiated field and maximum current distribution will not be in scattering resonance. To illustrate this point, let us consider the same explanation procedure followed by Sarkar in [102]. As mentioned in the previous section, external characteristic mode resonances for the TM_n^z polarization occur when $Y_n(ka) = 0$. Unlike natural resonance, which is produced for the complex ka value solving $H_n^{(2)}(ka) = 0$, if $Y_n(ka) = 0$ is substituted in equation (3.21), a maximum electric current does not occur at this ka real value. The same can be said for the scattered field when one looks at equation (3.22). Only $H_n^{(2)}(ka) = 0$ breaks down the electric current and the scattered field.

$$J_z = \frac{-2E_0}{k\eta\pi a} \sum_{n=-\infty}^{\infty} \frac{j^{-n} e^{jn\phi}}{H_n^{(2)}(ka)} \tag{3.21}$$

$$E_z^s = -E_0 \sum_{n=-\infty}^{\infty} j^{-n} \frac{J_n(ka)}{H_n^{(2)}(ka)} H_n^{(2)}(k\rho)\, e^{jn\phi} \tag{3.22}$$

As mentioned previously, the same happens for the RCS spectrum. They give real ka values and the electric current and the scattered electric field are approximately in resonance for those RCS resonances. That is to say, resonant peaks in RCS plot do occur at real frequencies at which the zeros of equations (3.8) and (3.9) are not zero. Nevertheless, a good agreement is observed in most cases for the real frequency pole coordinates when compared to the RCS spectrum and physical information can be obtained from it [86].

3.6 Open Question: Propagation and TCM

Until today, the TCM has only been used for the design of antennas and scatterers. However, it may be of interest to apply them to closed waveguides, since as it has been shown before, the internal resonances of the characteristic modes predict the transverse resonances of the PEC cylinder, i.e., internal NRs. And because the waveguides can also be designed considering the MoM [105, 109, 110], and the TMC is built based on it, it could be useful to design closed waveguides by using the TCM.

Thus, the question is, could the characteristic eigenvalues give us the dispersion diagram of guided modes inside an arbitrary cross-section metallic waveguide? Let us study the circular PEC waveguide as an example.

To study this, the EFIE of a circular PEC cylinder has to be solved considering oblique incidence. The entire analytical resolution of it can be seen in Appendix A.1. Let us consider a circular waveguide with radius $a = 5$ mm filled with air ($k = k_0$). The impedance matrix operator presented by equation A.12 is shown below,

$$Z = \frac{2\pi a}{4\omega\varepsilon_0} \cdot \begin{bmatrix} k_t^2 J_n(k_t a) H_n^{(2)}(k_t a) & \frac{n}{a} k_z J_n(k_t a) H_n^{(2)}(k_t a) \\ \frac{n}{a} k_z J_n(k_t a) H_n^{(2)}(k_t a) & \frac{nk_z}{ak_t} J_n(k_t a) \frac{nk_z}{ak_t} H_n^{(2)}(k_t a) - k_0^2 J_n'(k_t a) H_n'^{(2)}(k_t a) \end{bmatrix} \tag{3.23}$$

where $k_t = k_0 sin(\theta)$, $k_z = -k_0 cos(\theta)$, being θ the incident angle of a plane wave. As it differs with respect to other bodies, the impedance matrix has dependence on the incident angle and therefore the characteristic eigenvalues will also depend on θ. Let us therefore calculate the characteristic eigenvalues from the generalized eigenvalue equation that governs the conducting bodies, $X\mathbf{J}_n = \lambda_n R\mathbf{J}_n$. Therefore, separating the impedance matrix in its real R and imaginary X part and substituting in the eigenvalue equation the following curves are obtained.

As can be seen in Fig. 3.10, the eigenvalue curves of the TM_0 and TE_0 modes are presented for two different values of θ. In the case of a circular waveguide, the angles of incidence are related with the phase of the electric currents to generate its corresponding electromagnetic field propagating within the guide. Furthermore, since the impedance matrix is a 2×2 matrix, after the diagonalization the characteristic eigenvalues decouple each other generating the corresponding TM_n and TE_n family modes.

This has been shown in order to observe that the asymptotes of the eigenvalues move to the right as we move from $\theta = 90^\circ$ to lower angles. It is important to note that $\theta = 90^\circ$ represents the eigenvalues of the circular cross-section

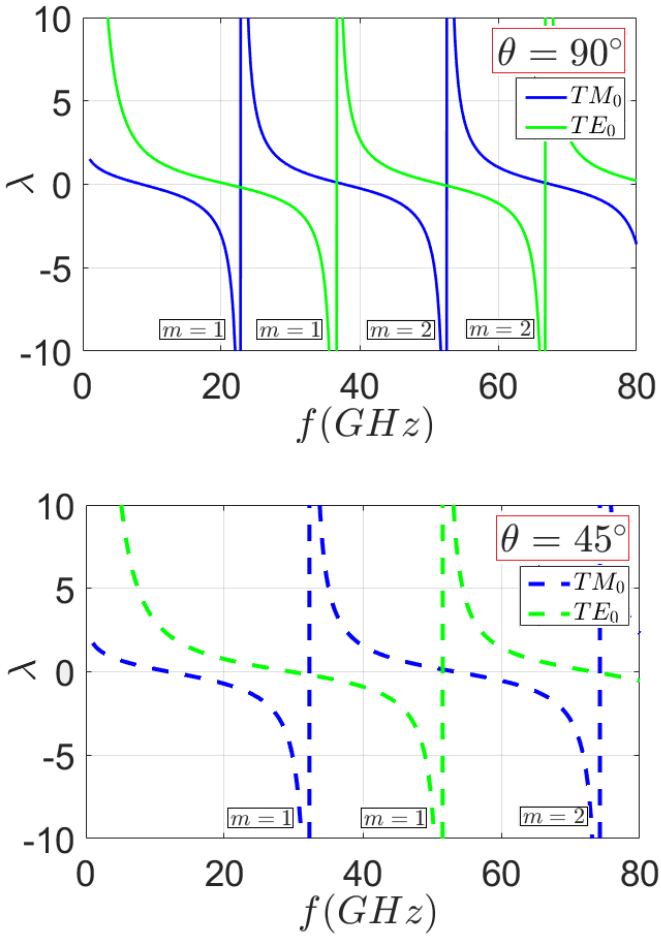

Fig. 3.10 Characteristic eigenvalues for two different incidence angles. Above: $\theta = 90°$. Below: $\theta = 45°$. Both top and down represent the eigenvalues of the TM_0 and TE_0 modes

waveguide. Thus, the internal CMRs extracted from the asymptotes of the eigenvalues will be in this case the cutoff frequencies of the modes. As regards the internal CMRs extracted for the rest of the angles, since the incidence is oblique, the EFIE sees the cylinder cross-section as if it were an elliptical section generating the internal CMRs of it. This is an equivalent problem to

that of the circular waveguide, and will provide the remaining information to complete the entire dispersion diagram.

On the other hand, as defined in section 3.3.2, each asymptote generated in the same eigenvalue refers to the corresponding resonance to the mode of different order m, i.e., as can be seen in the above graph the TM_0 mode has two internal CMRs $m = 1$ and $m = 2$ in the frequency range shown. These have to be represented such TM_{0m}, and therefore TM_{01} and TM_{02} modes. With respect to the below graph, the internal CMRs of the TM_{01}, TM_{02}, TE_{01} and TE_{02} have been shift as expected.

Thus, the idea to represent the dispersion diagram in a particular way is to give values to the incidence angles to have the corresponding k_z, and for each value of the same, to extract those frequencies for which an asymptotic behavior exists.

As it is well known, the conventional procedure uses the following formulas, [92].

$$\begin{aligned} J_n(k_t^{TM}a) = 0; \quad k_t^{TM} = \frac{P_{nm}}{a} \\ J_n'(k_t^{TE}a) = 0; \quad k_t^{TE} = \frac{P_{nm}'}{a} \end{aligned} \tag{3.24}$$

and uses the k_t values to obtain the $k_z = \sqrt{k_0^2 - k_t^2}$ as a function of frequency. In (3.24) P_{nm} and P_{nm}' are the zeros of the Bessel function and its derivative, respectively.

To show that the mentioned procedure works Fig. 3.11 shows the dispersion diagrams obtained by this new method presented here, and the conventional one. Dispersion curves obtained by these two methods superimposed each other, i.e. they coincide.

This method works for the calculation of any of the modes of the circular guide. The study of the characteristic modes, and other cross sections, remains an open question to this work.

3.7 Conclusion

In this chapter, some aspects in the interpretation of the solutions obtained when analyzing PEC cavities with the TCM have been presented. Firstly, NRs and CMRs of the infinite PEC circular cylinder and a PEC sphere have been pre-

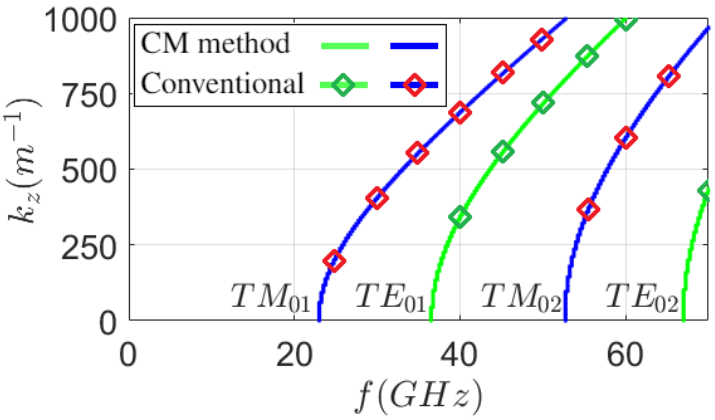

Fig. 3.11 Dispersion diagram for the circular waveguide. Modes TM_{01}, TE_{01}, TM_{02}, and TE_{02} Conventional method and CM method coincide each other.

sented using the analytical EFIE operators. These operators are those calculated considering both TM_n^z and TE_n^z polarizations. Secondly, NRs and CMRs have been compared. It has been concluded that external NRs and external CMRs are different. However, internal NRs and internal CMRs coincide. Moreover, characteristic eigenvalues have been used to find NRs in complex *ka* plane. It has been shown that characteristic eigenvalues remain real while it is possible to locate NRs with them. In addition, it has been explained why external NRs and external CMRs are different. This has been done using the SEP and the polar representation of the characteristic impedance. It can be concluded that characteristic eigenvalues are related with the phase angle of the characteristic impedance and they do not predict external NRs when considering real *ka* values in PEC cavities. Furthermore, the thesis stating that being at a given external CMR does not imply maximum wave scattering is also demonstrated. Finally, a method to extract the dispersion diagram has been presented considering the circular waveguide, whose solution coincides with the conventional one.

It is worth remarking, however, that the conclusions drawn, apply to a closed conducting body exhibiting internal and external resonances. Open bodies such as flat plates or thin dipoles will not show such important differences between external CMRs and external NRs since the imaginary part of the latter are significantly closer to the real axis.

Chapter 4

Analysis of Resonances on Dielectric Bodies

Now we turn to the interpretation of the resonances provided by the theory of characteristic modes (CMs) for dielectric bodies. The analysis has been performed analytically based on surface integral equation (SIE) using the Poggio-Miller-Chang-Harrington-Wu-Tsai (PMCHWT) formulation on a canonical problem such as the infinite dielectric circular cylinder. Firstly, natural resonances (NRs) and characteristic mode resonances (CMRs) are presented and compared. It has been observed that CMRs are in general near to internal NRs but not to external ones. It will also be demonstrated that characteristic resonances become closer to internal natural ones as the relative permittivity of the dielectric cylinder is increased. The same analysis, but numerically, has been carried out for a dielectric sphere.

Furthermore, a detailed analysis of CMs and fields of an infinite dielectric circular cylinder when computed through the PMCHWT formulation is carried out. The purpose is to determine their contribution to the total field, inside and outside the dielectric body and under two possible excitations: incident plane wave or electric line source within the cylinder. The study has been done analytically to provide necessary physical insight of the results obtained. New details about so-called *non-physical* modes are provided, [8]. It is found that these modes, that can be neglected outside the dielectric body, do have a significant contribution to the inner field when the excitation source is within the dielectric body. It is concluded that the terms physical and *non-physical* CMs should more properly be replaced for radiating and non-radiating CMs.

The conclusions obtained in this chapter will be considered for the development of the design method presented in the next chapter.

4.1 Introduction

NRs (NRs) on dielectric bodies have been extensively studied in the past. Some of the main geometries studied are the infinite circular cylinder and the sphere. The infinite circular cylinder was first studied by Rayleigh [97], and the sphere by Mie [77]. After these two works, many other works have been carried out to understand physically the behavior of the electromagnetic fields inside and outside of them. Linked to this, many of these works treated the resonance problem of the natural modes that can be excited by a source.

For example, with regard to the infinite dielectric circular cylinder, in [112], resonant modes, field patterns, resonant frequencies, and quality factors of the modes were determined. In [41] internal and external resonant modes for both TM^z and TE^z polarizations were analyzed providing a mathematical procedure for singling out internal and external NRs without resorting to *a priori* visualization of the electromagnetic field of the mode. Even if simple, the analysis of an infinite dielectric circular cylinder may be of practical use in problems such as the estimate of cylinder radius for optical-communications fibers through its transverse resonances [89], [67], among others.

Concerning the dielectric sphere, in [38] natural resonant frequencies and poles associated with the electromagnetic modes were analyzed. In [30], internal and external NRs were exhaustively studied via the Mie series, and in [71], the Cauchy method was applied to extract the NRs of dielectric spheres considering different parameters such as permittivity and conductivity.

The knowledge of these two canonical geometries has been very important, not only for its own sake, but also for the insight it provides for other more general geometries. That is why new methods have been developed to extract NRs from arbitrary structures, such as the Cauchy method mentioned above. Other methods are the Singularity Expansion Method (SEM) [15] and the Prony's method, among others. An alternative approach, similar to SEM, would be to determine the NRs by searching the complex frequency plane for the zeros of the determinant of the Method of Moments (MoM) matrix, [50, 66]. All the methods mentioned provide the same set of resonances.

Unlike this type of resonances, the TCM provides other type of modes and resonances. As for conducting bodies, when compared to NRs, whose

resonances are generally complex, the resonances provided by CMA are all real. Although many design-related works have been published, particularly devoted to metallic antennas and scatterers, there are still theoretical aspects in dielectric antennas that are unknown and need to be clarified to provide correct interpretation of the characteristic mode solutions. In order to interpret these solutions, it is interesting to use NRs as a reference. In this regard, NRs are unique, regardless of the method considered to obtain them and the integral formulation approach used [70]. It is worth mentioning [102], where some insightful discussions about CMRs and NRs for conducting bodies led to greater clarity on this subject. However, with regard to dielectric bodies, there are still many issues to be clarified because the formulation derived in [29], if hastily interpreted, may lead to misunderstandings. In [5] is concluded that NRs and CMRs are very close to each other. Moreover, they found some spurious modes called *non-physical* modes. On the other hand, in [19] it is concluded that NRs and CMRs are in fact very different. This leads to opposite views. Due to this misunderstandings, [35] and [33] proposed an alternative generalized eigenvalue equation involving only the equivalent electric current on the surface. Starting from the PMCHWT operator, they obtained a modified matrix operator to form a new generalized eigenvalue equation from which CMs were calculated for dielectric bodies. Furthermore, in [59], five integral equation formulations were compared for CMA of dielectric resonators and concluded that PMCHWT cannot fully predict resonant frequency of dielectric resonators.

Linked to the *non-physical* modes topic, a difficulty appears when understanding the CMs solutions provided by the PMCHWT formulation [91], since this formulation provides two eigenvalues per mode. In [8] and [5], it appeared that some of the solutions did not fulfill the orthonormality relation for the characteristic fields proposed by Chang and Harrington in [29]. Furthermore, considering the increasing number of applications using the PMCHWT formulation, they advised to avoid these spurious solutions. These solutions were regarded as *non-physical*, and after [5], some articles have been published presenting new methods to avoid the *non-physical* modes. In [6] a characteristic mode tracking algorithm for dielectric bodies was developed based on the orthogonality condition for the fields eliminating the *non-physical* solutions. The same author presented after [4], enhancing its existing tracking algorithm [6], which is based on eigencurrent correlation and far zone eigenfield orthogonality. On the other hand, in [79] a post-processing algorithm based on basis function perturbation is developed to remove what they call non-real CMs , i.e.,

non-physical modes, but considering lossy materials. Moreover, in [80] they proposed a new postprocessing method capable of providing unique and real CMs in all physical media, including lossy magnetic and dielectric materials. The method removes the *non-physical* solutions, called now internal resonances of a structure by defining a minimum radiated power. Furthermore, in [81] and Miers and Lau [78] the extent of what they called internal resonance problem of the PMCHWT formulation in mixed conductor-dielectric structures is explored and a new method to remove them is presented. As a consequence, some researchers prefer to study DRA with the well-known VIE, [115], when using the TCM on dielectric bodies. In fact, FEKO [45] eliminates these solutions from its results. But, even if these *non-physical* solutions do not satisfy the orthonormality condition for the characteristic far fields, it is not demonstrated yet that their contribution can be discarded for the total field within the dielectric body when considering specific sources to excite them. So if it turns out that these *non-physical* modes do contribute to the electromagnetic field within the dielectric resonator, it would have been a mistake to name them that way, and it will be necessary to redefine them accordingly, given their physical meaning.

In this chapter, the conclusions drawn by [5] and [19] will be discussed and linked throughout the chapter. In addition, some aspects in the interpretation of the resonances provided by CMA are analyzed. This has been done using the analytical solution of the PMCHWT integro-differential operator for the infinite dielectric circular cylinder, and numerically by using also the PMCHWT formulation for the dielectric sphere. Firstly, NRs and CMRs are presented and compared. Secondly, it is demonstrated that CMRs are only close to the internal NRs and do not provide information at all about the external ones. Finally, it is shown that CMRs become closer to internal NRs as the relative permittivity of the dielectric cylinder is increased. Furthermore, it is also found that, for a given permittivity, each natural mode observed, provides a different error between the CMRs and the NRs. On the other hand, it is carried out an analysis concerning mainly the physical interpretation of the CMs of an infinite dielectric circular cylinder when a PMCHWT formulation is used. Given the canonical nature of the problem, the analysis leads to explicit analytical solutions, providing faster solutions and deeper knowledge than a purely numerical analysis. In addition, this analytical solution will serve as a reference to compare with numerical MoM solutions based on SIE. As part of the analysis, the contribution of each eigensolution to the total electric and magnetic equivalent currents is discussed. This discussion is carried out considering two situations: a normally incident

TM^z plane wave and an electric line source located inside the cylinder. This will help to clarify the role of all CMs provided by the PMCHWT formulation, and to clarify also the physical meaning of the so-called *non-physical* modes.

Since the intention of this chapter is to interpret the solutions in the TCM in dielectrics, the results obtained in this chapter will be considered in Chapter 5. There, a new design method will be presented and applied to a rectangular DRA.

4.2 The Infinite Dielectric Circular Cylinder

In this section, NRs and CMRs are compared through the PMCHWT formulation. Since we are dealing with an infinite circular cylinder, the PMCHWT operator can be written in its closed form for both the TM^z and the TE^z polarizations. [29] was followed to derive these analytical operators. Some of the steps to find its closed form solution are explained in the following. More detailed steps can be found in Appendix A.2.

Due to the rotational symmetry of the boundary surface, cylindrical harmonics $\{\cos(n\phi),\sin(n\phi)\}$ are selected as entire domain basis functions to represent the CMs. As Garbacz stated in [49], CMs have to be selected real and these modes are the appropriate basis functions for the circular cylinder. The n indicates the *n-th* mode order. For simplicity in the calculation, the set of cylindrical harmonics $\left\{e^{jn\phi}\right\}$ has been chosen to solve the equations. Then, for TM^z and TE^z cases we have

$$\left\{ \begin{array}{c} \mathbf{J} \\ \mathbf{M} \end{array} \right\}^{TM^z} = \sum_{n=-\infty}^{\infty} \left\{ \begin{array}{c} \alpha_n^{TM^z} \\ \beta_n^{TM^z} \end{array} \right\} e^{jn\phi} \left\{ \begin{array}{c} \widehat{z} \\ \widehat{\phi} \end{array} \right\} \tag{4.1}$$

$$\left\{ \begin{array}{c} \mathbf{J} \\ \mathbf{M} \end{array} \right\}^{TE^z} = \sum_{n=-\infty}^{\infty} \left\{ \begin{array}{c} \alpha_n^{TE^z} \\ \beta_n^{TE^z} \end{array} \right\} e^{jn\phi} \left\{ \begin{array}{c} \widehat{\phi} \\ \widehat{z} \end{array} \right\} \tag{4.2}$$

Thus the characteristic eigencurrents J_n and M_n have to be $\left\{e^{jn\phi}\right\}$. In (4.1) and (4.2) α_n and β_n are unknown Fourier coefficients to be found for a given excitation. Operators L_e, L_m and C from equation (2.66) involve the two-dimensional Green's function $G(\boldsymbol{\rho},\boldsymbol{\rho}') = \frac{1}{4j}H_0^{(2)}(k|\boldsymbol{\rho}-\boldsymbol{\rho}'|)$, where the Hankel

function of the second kind $H_0^{(2)}(k|\boldsymbol{\rho}-\boldsymbol{\rho}'|)$ can be rewritten in series form using the addition theorem of Hankel functions, [1]:

$$H_0^{(2)}(k|\boldsymbol{\rho}-\boldsymbol{\rho}'|) = \begin{cases} \displaystyle\sum_{m=-\infty}^{\infty} J_m(k_2\rho)H_m^{(2)}(k_2\rho')e^{jm(\phi-\phi')}, & \rho \leq \rho' \\ \displaystyle\sum_{m=-\infty}^{\infty} J_m(k_1\rho')H_m^{(2)}(k_1\rho)e^{jm(\phi-\phi')}, & \rho' \leq \rho \end{cases} \tag{4.3}$$

In (4.3), $J_m(x)$ are the Bessel functions of the first kind, and k_1 and k_2 are the outer and the inner wavenumbers, respectively. To obtain the matrix operator, a Galerkin method employing $e^{jn\phi}$ as basis and testing functions is used. The inner product involved is defined in (4.4).

$$\langle u^*, v\rangle = \int_0^{2\pi} u^*(\phi) \bullet v(\phi)\, d\phi \tag{4.4}$$

Where u^* is the complex conjugate of u. Inserting (4.1), (4.2) and (4.3) into (2.66), and applying a left scalar multiplication by $e^{-jn\phi}$, equation (4.5) can be obtained.

$$T_n' \begin{bmatrix} \alpha_n \\ \beta_n \end{bmatrix} = \left\langle \left[e^{-jn\phi}, e^{-jn\phi}\right], \begin{bmatrix} E^i \\ H^i \end{bmatrix} \right\rangle \tag{4.5}$$

where the matrix operator T_n' is defined as

$$T_n' = \begin{bmatrix} \langle J_n^*, L_e(J_n)\rangle & \langle J_n^*, -C(M_n)\rangle \\ \langle M_n^*, C(J_n)\rangle & \langle M_n^*, L_m(M_n)\rangle \end{bmatrix}_n \tag{4.6}$$

These solutions are calculated in Appendix A.2, and they are (A.35) and (A.43) for the TM_n^z modes, and (A.45) and (A.46) for the TE_n^z modes. Since the eigenfunctions of the integral operators L_e, L_m and C are used as basis and testing functions (Galerkin procedure), sub-matrices associated to each operator are diagonal. Therefore each *n-th* mode is decoupled from the others and can be solved separately. Furthermore, since the infinite circular cylinder is a canonical geometry, it is noteworthy to mention that n index dependence

in matrix operator (4.6) implies orthogonality between the n modes and they can be solved independently from each other. Introducing equations (A.35) and (A.43), or (A.45) and (A.46) in equation (4.5), the explicit expression (4.6) for T_n' can be obtained for the TM_n^z and TE_n^z modes, respectively. The sub-operators forming matrix (4.6) are presented by equations (4.7-4.10) and (4.11-4.14), and may be used for magnetic, dielectric, or magneto-dielectric bodies.

The sub-operators for the TM^z polarization are the following:

$$\langle J_n^*, L_e(J_n)\rangle = (\pi a)^2 \omega \left(\mu_2 J_n(k_2 a) H_n^{(2)}(k_2 a) + \mu_1 J_n(k_1 a) H_n^{(2)}(k_1 a)\right) \quad (4.7)$$

$$\langle J_n^*, -C(M_n)\rangle = j(\pi a)^2 \left(k_2 J_n'(k_2 a) H_n^{(2)}(k_2 a) + k_1 J_n(k_1 a) H_n'^{(2)}(k_1 a)\right) \quad (4.8)$$

$$\langle M_n^*, C(J_n)\rangle = -j(\pi a)^2 \left(k_2 J_n'(k_2 a) H_n^{(2)}(k_2 a) + k_1 J_n(k_1 a) H_n'^{(2)}(k_1 a)\right) \quad (4.9)$$

$$\langle M_n^*, L_m(M_n)\rangle = (\pi a)^2 \omega \left(\varepsilon_2 J_n'(k_2 a) H_n'^{(2)}(k_2 a) + \varepsilon_1 J_n'(k_1 a) H_n'^{(2)}(k_1 a)\right) \quad (4.10)$$

The sub-operators for the TE^z polarization are the following:

$$\langle J_n^*, L_e(J_n)\rangle = (\pi a)^2 \omega \left(\mu_2 J_n'(k_2 a) H_n'^{(2)}(k_2 a) + \mu_1 J_n'(k_1 a) H_n'^{(2)}(k_1 a)\right) \quad (4.11)$$

$$\langle J_n^*, -C(M_n)\rangle = j(\pi a)^2 \left(k_2 J_n'(k_2 a) H_n^{(2)}(k_2 a) + k_1 J_n(k_1 a) H_n'^{(2)}(k_1 a)\right) \quad (4.12)$$

$$\langle M_n^*, C(J_n)\rangle = -j(\pi a)^2 \left(k_2 J_n'(k_2 a) H_n^{(2)}(k_2 a) + k_1 J_n(k_1 a) H_n'^{(2)}(k_1 a)\right) \quad (4.13)$$

$$\langle M_n^*, L_m(M_n)\rangle = (\pi a)^2 \omega \left(\varepsilon_2 J_n(k_2 a) H_n^{(2)}(k_2 a) + \varepsilon_1 J_n(k_1 a) H_n^{(2)}(k_1 a)\right) \quad (4.14)$$

Equations (4.7-4.10) and (4.11-4.14) represent the analytical TM_n^z and TE_n^z PMCHWT matrix sub-operators, where a is the cylinder radius, $H_n^{(2)}(x)$ are the Hankel functions of the second kind, $J_n(x)$ the Bessel functions of the first kind, n the azimuthal mode order, k_j the wavenumber, and the pairs (ε_j, μ_j) are the permittivity and the permeability, respectively. The primes on the Bessel

and Hankel functions denote differentiation with respect to the entire argument. The subscripts $j = 1$ or $j = 2$ stands for outer and inner media, respectively.

The dielectric circular cylinder is shown in Fig. 4.1. The pairs (ρ, ϕ) and (ρ', ϕ') are observation and source point locations in polar coordinates, respectively.

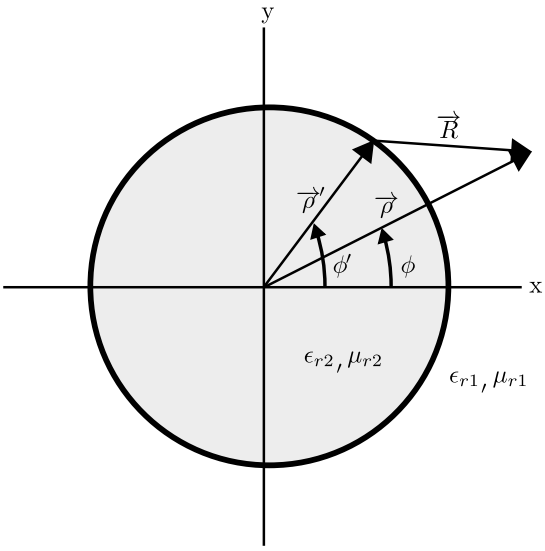

Fig. 4.1 Geometry and material of the considered infinite dielectric circular cylinder

4.2.1 Natural Resonances

NRs are extracted from the zeros of the determinant of the PMCHWT matrix operator, [50]. Thus, concerning the infinite dielectric circular cylinder, the determinant of the operator (4.6) have to be equal to zero to find its corresponding NRs. The cylinder under study is $\varepsilon_{r_2} = 9$ and $\mu_{r_2} = 1$, and the surrounding media is considered to be vacuum. Substituting these values in (4.6) after considering the corresponding sub-operators (4.7-4.10) and (4.11-4.14), some of the first natural resonances of the TE_n^z and TM_n^z modes for $n = 0, 1, 2, 3$ can be found, respectively. These resonances are shown in Fig. 4.2.

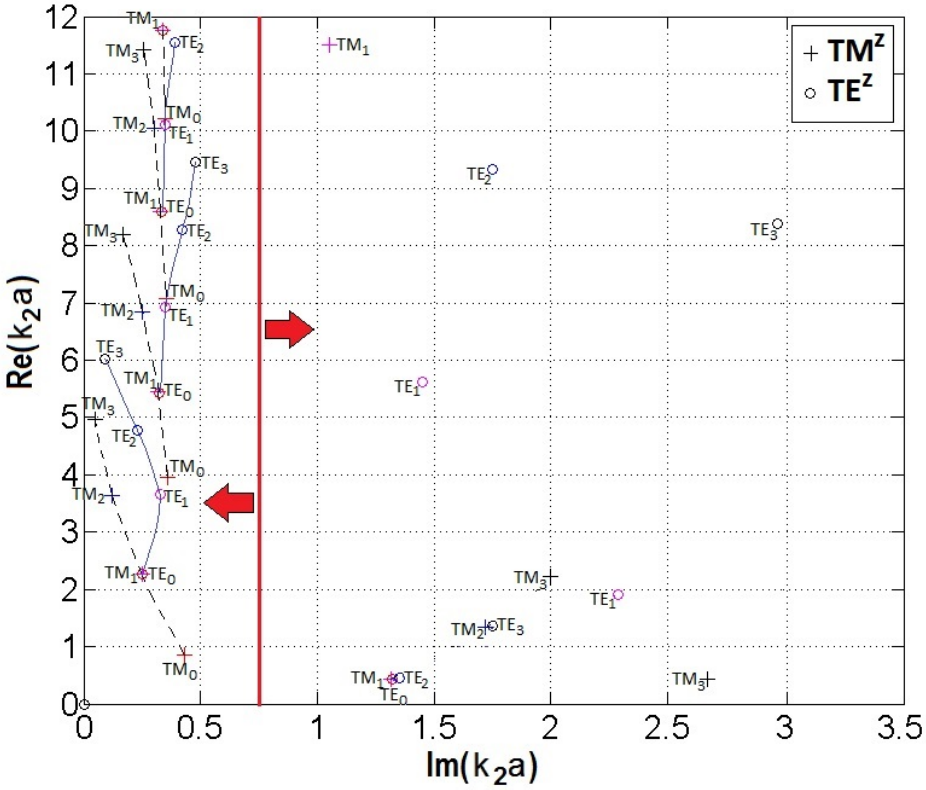

Fig. 4.2 NRs obtained from the SIE operator and the scattering coefficient of the harmonic series solution. Obtained values match perfectly. Placement of dividing vertical line at $Im(k_2a) = 0.75$ is arbitrary, with the only purpose of remarking where the internal/external NRs are located. Internal NRs are located to the left of the line, and external NRs to the right. The relative permittivity of the cylinder is $\varepsilon_2 = 9$ and the outer media is considered vacuum.

In order to determine the zeros of $\det(T_n'(k_2a))$, a standard zero-finding routine is used as in [50].

These resonances are located in the k_2a complex plane as done in [30] for the dielectric sphere. $k_2a = \omega\sqrt{\varepsilon_2\mu_2}$, ε_2 and μ_2 are the wave number, permittivity, and permeability of the inner media. The subscript "2" designates the inner media. In Fig. 4.2 TM_n^z and TE_n^z modes are marked with "+" and "∘",

respectively. The real part of the NRs provides the resonant frequency, and the imaginary part the damping factor. The damping factor provides information on how a given mode is leaking.

Considering the conclusions presented in [30], the same can be concluded here: the NRs can be separated into internal and external. The internal resonances are caused by the internal waves that experiment multiple internal reflections, whereas the external resonances are caused by creeping waves. These creeping waves propagate along the surface with attenuation due to the continuous radiation in tangent direction. In Fig. 4.2, the internal NRs are on the left-hand side of a vertical line, and the external NRs are located on the right-hand side, both indicated by arrows. The vertical line only serves to divide the graph between the internal and the external NRs, helping the understanding of the graph . Notice that unlike PEC cavities, internal resonances are complex-valued here. In order to differentiate between internal and external NRs, one can use the formulas given by [41], where a complete analysis for an infinite dielectric circular cylinder is shown to clearly distinguish between internal and external modes for both TM^z and TE^z polarization. For the TM^z polarization, the internal and external NRs can be found using the limits (4.17-4.19) and (4.20), respectively,

$$\lim_{\varepsilon_{r_2}\to\infty}[k_2a]_{n,m} = j_{n-1,m} \Rightarrow n \neq 0 \tag{4.17}$$

$$\lim_{\varepsilon_{r_2}\to\infty}[k_2a]_{0,m} = j_{1,m-1} \Rightarrow m \neq 1 \tag{4.18}$$

$$\lim_{\varepsilon_{r_2}\to\infty}[k_2a]_{0,1} = 0 \tag{4.19}$$

$$\lim_{\varepsilon_{r_2}\to\infty}[k_1a]_{n,m} = h_{n,m} \tag{4.20}$$

Regarding the TE^z polarization, the internal and external NRs can be found using equations (4.21) and (4.22), respectively.

$$\lim_{\varepsilon_{r_2}\to\infty}[k_2a]_{n,m} = j_{n,m} \tag{4.21}$$

$$\lim_{\varepsilon_{r_2}\to\infty}[k_1a]_{n,m} = h'_{n,m} \tag{4.22}$$

These equations provide the difference between internal and external resonances. When the relative permittivity tends to infinity, internal NRs, which start being complex valued, become real in the limit according to the corresponding definition. On the contrary, external resonances remain complex-valued. This allows one to distinguish between internal and external NRs.

To verify the correctness of equations (4.7-4.10) and (4.11-4.14) substituted on matrix (4.6), a comparison between the scattering coefficient poles of the harmonic series solution (4.23) and (4.24) is performed in Fig. 4.2.

$$TM^z \to \eta_2 J_n(k_2a)H_n^{\prime(2)}(k_1a) - \eta_1 J'_n(k_2a)H_n^{(2)}(k_1a) = 0 \tag{4.23}$$

$$TE^z \to \eta_2 J'_n(k_2a)H_n^{(2)}(k_1a) - \eta_1 J_n(k_2a)H_n^{\prime(2)}(k_1a) = 0 \tag{4.24}$$

An excellent agreement among both procedures can be seen.

4.2.2 Characteristic Mode Resonances

As in the case of NRs, the resonances provided by characteristic mode analysis are also classified in two types, internal and external. Nevertheless, as we will see in the next subsection, they are different from NRs.

The characteristic eigenvalues of a given *n-th* mode for the infinite dielectric circular cylinder are calculated by solving the weighted eigenvalue problem (2.73) on the operator defined by equation (4.6), but after the symmetrization presented by equation (2.67). That is to say:

$$T_n = \begin{bmatrix} \langle J_n^*, L_e(J_n)\rangle & -j\langle J_n^*, C(M_n)\rangle \\ -j\langle M_n^*, C(J_n)\rangle & \langle M_n^*, L_m(M_n)\rangle \end{bmatrix}_n \tag{4.25}$$

So therefore, the non-symmetric operator T_n' expressed by equation (2.66) becomes T_n, a symmetric one. As explained in Chapter 2, this is necessary to obtain real eigencurrents and eigenvalues after the characteristic mode diagonalization procedure.

Thus, since T_n is now symmetric, it can be expressed in terms of its Hermitian parts as $T_n = T_{n,re} + jT_{n,im}$, and the eigenvalue equation defining the CMs is

$$[T_{n,im}][\mathbf{f}_n] = \lambda_n [T_{n,re}][\mathbf{f}_n] \tag{4.26}$$

where $T_{n,2}$ and $T_{n,1}$ are the imaginary and the real part of the PMCHWT matrix operator T_n. In (4.26), λ_n are real characteristic eigenvalues and $\mathbf{f}_n$ the coefficients of the characteristic cylindrical modes $\{\cos(n\phi), \sin(n\phi)\}$, or CMs. These coefficients are also real numbers. By definition, if $\lambda_n = \pm\infty$ (asymptotic behavior) or $\lambda_n = 0$ it means that at those frequencies, there is a suspected internal or external characteristic resonance, respectively.

Let us consider the same example as for the previous section: a non-magnetic homogeneous cylinder with $\varepsilon_{r_2} = 9$. The characteristic eigenvalues obtained are shown in Fig. 4.10, in which the analytical eigenvalues are validated by comparing them with those obtained numerically by an in-house code interfaced with FEKO. Notice that a 1-dimensional periodic boundary condition and the surface equivalence principle were used to simulate the infinite cylinder with FEKO.

Fig. 4.3 shows an excellent agreement between the numerical and the analytical solutions. Those few points scattered outside the curve are due to numerical errors. As shown in Fig. 4.3, two eigenvalues are obtained per each mode, as it must be, given that PMCHWT is a 2×2 linear integro-differential operator. In Fig. 4.3, the eigenvalues with superscripts 1 and 2 are referred to as the physical and the *non-physical* characteristic eigenvalues, respectively. This notation is adopted after [5], where a more detailed explanation can be seen.

In addition, each eigenvalue has its associated subscript indicating the polarization type and the order of the cylindrical harmonic solution, i.e., TM_n^z, TE_n^z. It is interesting to note that eigenvalues corresponding to the TE_0^z and the TM_1^z coincide with each other. Now, turning to the *non-physical* modes, this term was adopted in [8] because they were declared of no relevance in

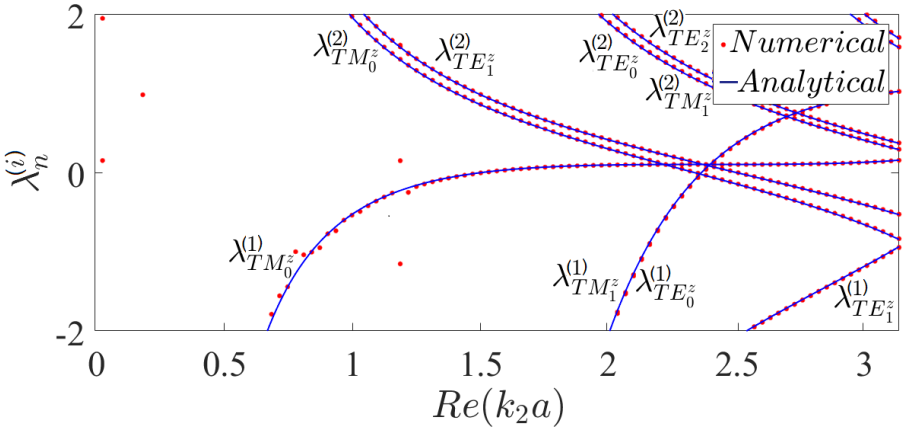

Fig. 4.3 Comparison between analytic and numerical characteristic eigenvalues for the infinite dielectric circular cylinder. The relative permittivity of the cylinder is $\varepsilon_{r_2} = 9$ and the outer media is considered vacuum.

CMA. Therefore, the next subsection only deals with resonances of the physical modes.

4.2.3 Natural Resonances vs Characteristic Mode Resonances

In this subsection the study concerns mainly the differences between NRs and CMRs. NRs were compared with CMRs for DRs in [5], and [19]. In [5] an isolated cylindrical dielectric resonator with $\varepsilon_r = 79.7$ was studied. They concluded that the CMRs occur at the same frequencies as the natural modes with an agreement between the two sets of frequencies within 4%. However, in [19], an infinite dielectric circular cylinder with $\varepsilon_{r_2} = 9$ was analytically analyzed concluding that CMRs were different from NRs, observing a larger difference than in [5], and stating that CMR can be seen as a different type of resonance. It is believed that the reason why [5] arrived at a different conclusion was probably because a high relative permittivity value was used. Here, however, it is observed that when lower relative permittivities are considered, the differences between CMRs and NRs are much larger. The results presented in this subsection are therefore crucial to the application of CMA to DRs and dielectric resonator antenna design.

The statements below will be demonstrated regarding the infinite dielectric circular cylinder:

1. CMRs are distinct from NRs.

2. Internal ($\lambda_n \to \pm\infty$) and external ($\lambda_n = 0$) CMRs provide values that are close to internal NRs only, while external ones are not accounted for by CMRs.

3. The gap found between CMRs and internal NRs differs depending on the electromagnetic mode considered. In other words, each characteristic mode differs from its corresponding natural mode in a different way when it is subjected to permittivity variations and is compared with other modes having different order.

To demonstrate that NRs are different from CMRs Table 4.1 and Table 4.2 show some of the resonances obtained by both procedures and plotted in Figs. 4.2 and 4.3, respectively. It is obvious that the real part of the NRs are completely different from their corresponding CMRs.

Table 4.1 NRs for the first and second modes $(m = 1,2)$, poles $(n = 0,1,2)$, for the infinite dielectric circular cylinder graphed in Fig. 4.2.

k_2a	NRs $m=1$		NRs $m=2$	
n	$TM^z_{n,1}$	$TE^z_{n,1}$	$TM^z_{n,2}$	$TE^z_{n,2}$
0	0.85+j0.43	2.27+j0.25	3.95+j0.36	5.44+j0.33
1	2.27+j0.25	3.65+j0.33	5.45+j0.32	6.93+j0.35
2	3.64+j0.12	4.78+j0.23	6.84+j0.25	8.27+j0.42

Table 4.2 External CMRs for the infinite dielectric circular cylinder obtained from $\lambda^1_{TM^z_n}$, $\lambda^2_{TM^z_n}$, $\lambda^1_{TE^z_n}$ and $\lambda^2_{TE^z_n}$ curves in Fig. 4.10. These values correspond to the zero crossings of the eigenvalue curves.

$Re(k_2a)$	CMRs λ^1_X		CMRs λ^2_X	
n	$TM^z_{n,1}$	$TE^z_{n,1}$	$TM^z_{n,1}$	$TE^z_{n,1}$
0	1.514	2.371	2.340	3.490
1	2.371	3.545	3.490	2.505

It is interesting to note that, unlike a shielded cavity, whose internal NRs are located on the real axis of frequencies, a dielectric cavity has its internal NRs on the complex frequency plane because their corresponding internal modes leak. This leakage is due to radiation losses through the cavity wall. For example, an infinite PEC circular cylinder exhibits its internal resonances at frequencies that meet conditions $J_n(ka) = 0$ (TM_n^z) and $J_n'(ka) = 0$ (TE_n^z), resulting in real frequencies. This can be seen from [102] where a thorough discussion regarding internal NRs and CMRs for a PEC circular cylinder was carried out.

As can be seen from Table 4.1, the dielectric cylinder has complex-valued internal resonances. On the other hand, we note that CMRs are represented on the real k_2a axis. Let us consider for instance TM_0^z mode as in [19] to check the closeness between CMRs and NRs and the possible relation between them. Fig. 4.4 shows CM eigenvalues as curves and NRs as circles (only internal NRs). Recall that CM external resonance occurs for $\lambda^1_{TM_0^z} = 0$ while the internal one is for $\lambda^1_{TM_0^z} \to \pm\infty$. Values are shown for three relative permittivity values of $\varepsilon_{r_2} = 9$ in **(a)**, $\varepsilon_{r_2} = 90$ in **(b)**, and $\varepsilon_{r_2} = 900$ in **(c)**.

From left to right, the blue circles correspond to the projection of the internal NRs on the real k_2a axis for TM_{01}^z, TM_{02}^z and TM_{03}^z poles, respectively. It is evident that depending on the relative permittivity used, the internal NRs can be more or less predicted from the characteristic eigenvalues $\lambda^1_{TM_0^z}$. The higher the relative permittivity, the closer the CMRs are to the NRs. This occurs because internal NRs are in different imaginary planes, $Im(k_2a) \neq 0$, for each permittivity, while CMRs are always located on $Im(k_2a) = 0$. It can be concluded that CMRs are relatively close to the internal NRs depending on the permittivity. The same applies to the RCS spectrum which also provides values that are close to NRs, [86]. Therefore, although different, internal NRs are more predictable using both internal and external CMRs as permittivity increases.

To end the demonstration on whether CMRs and internal NRs become closer as the relative permittivity increases, Figs. 4.5 and 4.6 show the percentage variation between CMRs and the real part of NRs. Fig. 4.5 shows the percentage difference between the two types of resonances for the TM_n^z $(n = 0)$. As permittivity decreases, the percentage difference increases significantly. The same applies to Fig. 4.6, where TE_n^z $(n = 0)$ mode behavior is shown. The percentage difference for TE_n^z mode is less significant than for TM_n^z mode because TE_n^z mode is located closer to $Re(k_2a)$ axis than TM_n^z is, i.e., the damping is lower. This can be seen in Fig. 4.2.

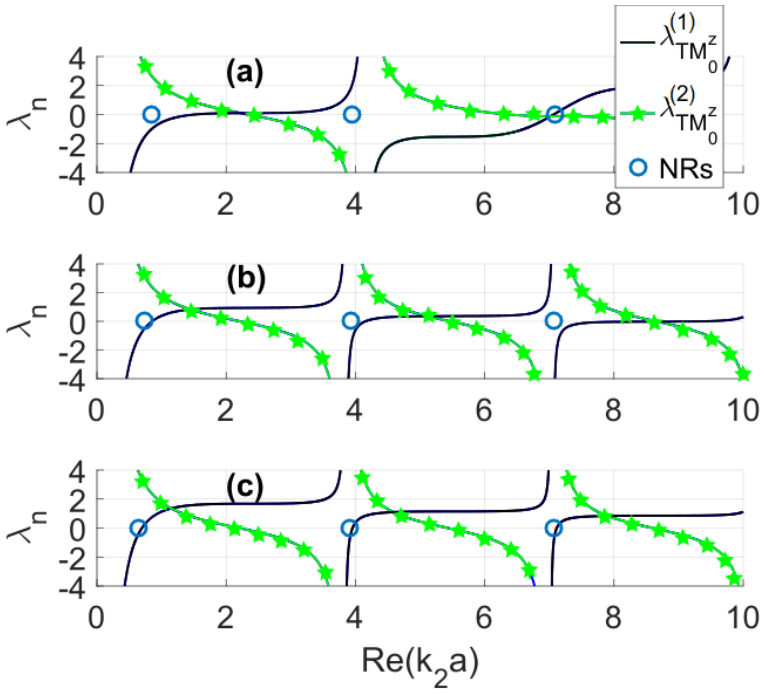

Fig. 4.4 A comparison between the characteristic eigenvalues and internal NRs (TM^z_{01}, TM^z_{02} and TM^z_{03}, circles from left to right, respectively) considering relative permittivity for the dielectric cylinder of $\varepsilon_{r_2} = 9$ in **(a)**, $\varepsilon_{r_2} = 90$ in **(b)**, and $\varepsilon_{r_2} = 900$ in **(c)**.

Why is this happening? The answer is simply because the higher the permittivity of the dielectric body, the closer to the $Re(k_2a)$ axis the internal resonances are, as explained by equations (4.17)-(4.22) above. That means the cavity modes have less leakage, and therefore the damping factor is lower. As a last evidence in this regard, Fig. 4.7 shows how TM^z_n and TE^z_n $(n = 0)$ resonances move into the complex k_2a plane as ε_{r_2} decreases. Number next to each pole in Fig. 4.7 is the corresponding ε_{r_2} value. As ε_{r_2} decreases, the damping becomes higher and so does radiation.

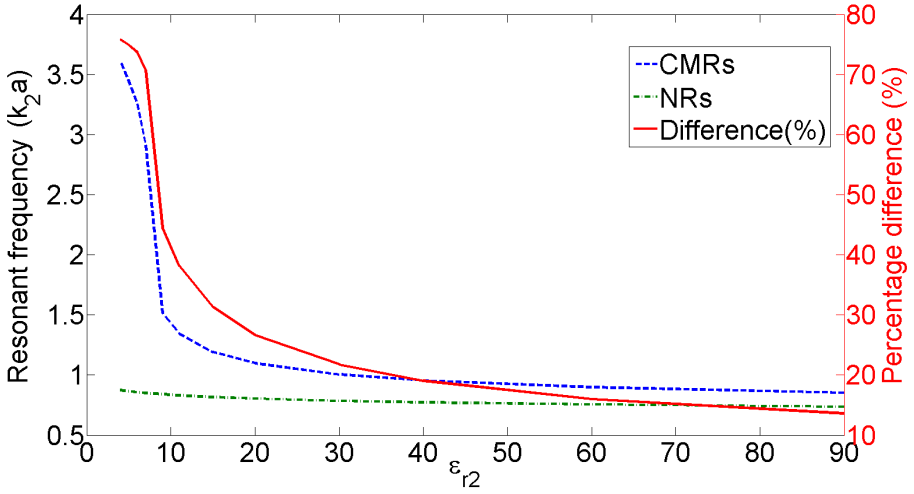

Fig. 4.5 Comparison between CMRs and NRs versus ε_{r_2} for TM^z $(n=0)$ mode.

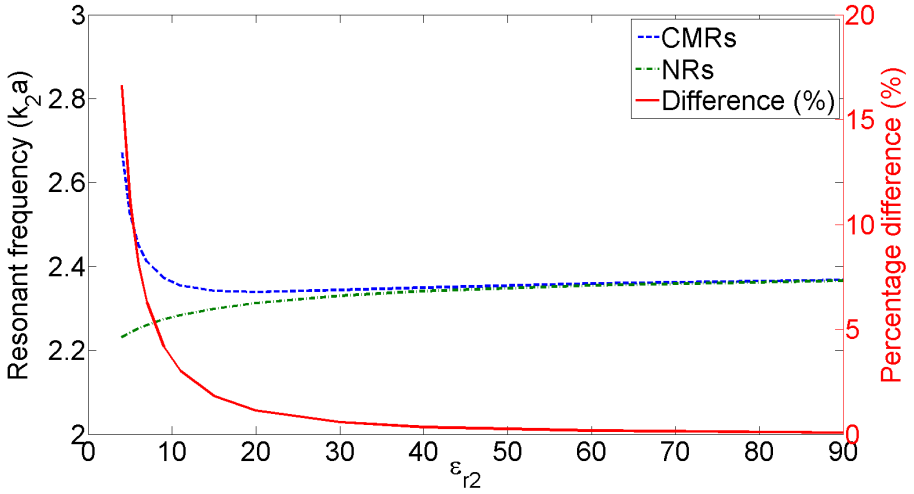

Fig. 4.6 Comparison between CMRs and the NRs versus ε_{r_2} for the TE^z $(n=0)$ mode.

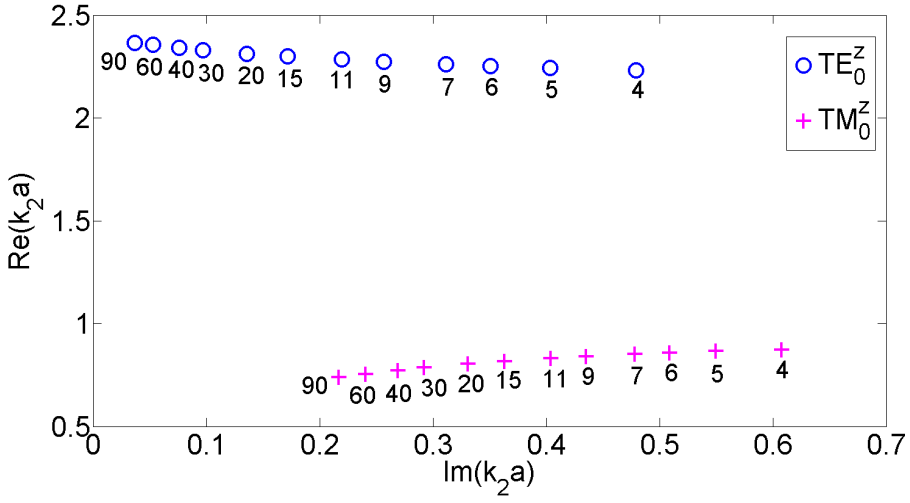

Fig. 4.7 Displacement of the NRs due to the variation of the permittivity for the TM^z and TE^z $(n = 0)$ mode. Numbers below the poles are its corresponding ε_{r_2}.

4.3 The Dielectric Sphere

In this section, the same analysis as the previously made for the infinite dielectric circular cylinder is briefly presented for the dielectric sphere. In this study, the aim is not only to present the relationship between NRs and CMRs, but also to show that the same conclusions can be reached for the dielectric sphere (3D analysis), as for the infinite circular dielectric cylinder (2D analysis).

Unlike the dielectric cylinder, for the dielectric sphere case it has not been necessary to analytically solve the PMCHWT formulation. For this reason, a numerical analysis has been performed to obtain the same conclusions as for the cylinder. In addition, solutions presented in [30] are also considered.

4.3.1 Natural Resonances

In [30] is presented a robust analysis for the NRs of the dielectric sphere. The method used in [30] is based on finding the zeros of the following equations:

$$TE^r \rightarrow \eta_2 \mathbb{J}_n(k_2 a)\mathbb{H}_n^{\prime(2)}(k_1 a) - \eta_1 \mathbb{J}_n^{\prime}(k_2 a)\mathbb{H}_n^{(2)}(k_1 a) = 0 \tag{4.27}$$

$$TM^r \rightarrow \eta_2 \mathbb{J}_n^{\prime}(k_2 a)\mathbb{H}_n^{(2)}(k_1 a) - \eta_1 \mathbb{J}_n(k_2 a)\mathbb{H}_n^{\prime(2)}(k_1 a) = 0 \tag{4.28}$$

These equations are the denominators of the scattering coefficients obtained via Mie series solution [77]. Note that equations (4.23) and (4.24) for the infinite dielectric cylinder have the same form as equations (4.27) and (4.28), but instead of Bessel and Hankel functions, they are defined by using Riccati-Bessel and Riccati-Hankel functions.

As demonstrated in Fig. 4.2 for the dielectric cylinder, NRs obtained from (4.23) and (4.24) are exactly the same as the NRs obtained from the PMCHWT analytical operator (4.6) when substituting the sub-operators (4.7-4.10) and (4.11-4.14) for the TM_n^z and TE_n^z modes, respectively. Thus, in the analysis presented here for the dielectric sphere, NRs obtained by equations (4.27) and (4.28) will be enough to present the solutions aimed.

Let us consider a non-magnetic sphere with $\varepsilon_{r_2} = 9$, as presented in [30]. The NRs obtained from equations (4.27) and (4.28) are presented in Fig. 4.8 In Fig. 4.8 TM_n^r and TE_n^r natural mode resonances are marked with "+" and "$\circ$", respectively. As can be seen, these resonances are located in the $k_2 a$ complex plane as done for the dielectric cylinder in Fig. 4.2. The real part of the NRs provides the resonant frequency, and the imaginary part the damping factor. These NRs can also be separated in internal and external. Internal NRs are on the left-hand side of the graph, and the external NRs are located on the right-hand side, indicated by the name "surface wave poles". Notice that unlike the PEC sphere, internal NRs are here complex valued due to the radiation losses, or leakage.

At this point, we can say that for NRs the same conclusions are reached as an infinite cylinder or a sphere. Let us see next what happens to the resonances obtained from the CMA.

4.3.2 Characteristic Mode Resonances

In this subsection, the characteristic eigenvalues for a dielectric sphere with relative permittivity $\varepsilon_{r_2} = 9$ are presented. This has been done to find the CMRs. Unlike the study for the infinite dielectric cylinder, in which its eigenvalues were extracted analytically, the characteristic eigenvalues of the dielectric sphere

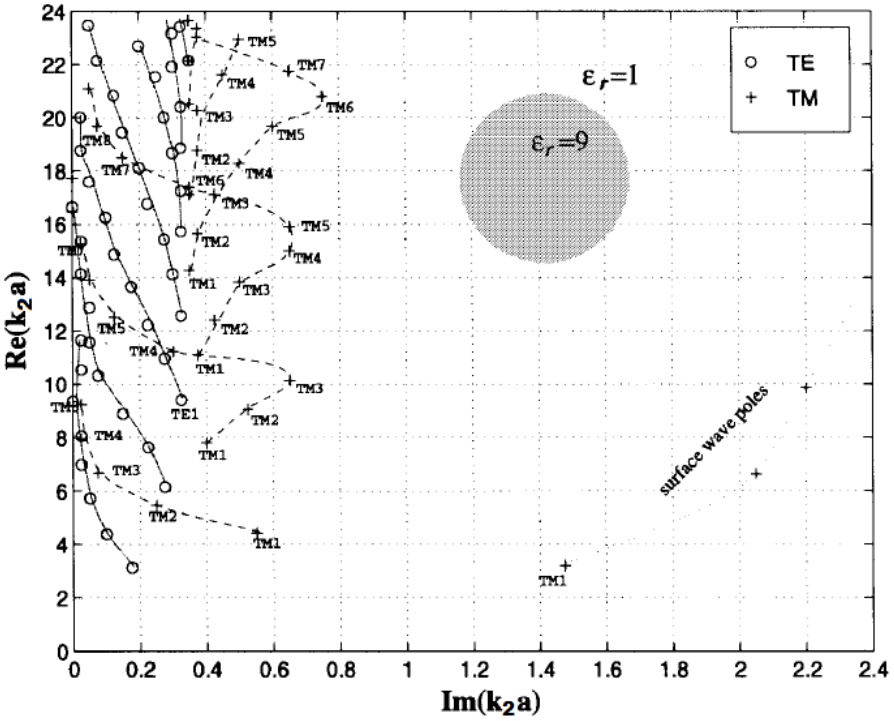

Fig. 4.8 NRs obtained from the scattering coefficient of the Mie series solution. Internal NRs are located to the left and external NRs on the right (surface wave poles). The relative permittivity of the sphere is $\varepsilon_{r_2} = 9$ and the outer media is considered vacuum. [30].

have been extracted numerically. To carry out this study, FEKO software and a MATLAB interface program have been used, since using only FEKO would generate only one of the two families of characteristic eigenvalues obtained when using the PMCHWT formulation. The characteristic eigenvalues obtained are shown in Fig. 4.9.

As in the case of NRs, the resonances provided by characteristic mode analysis are also classified in two types, internal and external. Nevertheless, as we will see in the next subsection, they are different from NRs. On the other hand, it is noteworthy that in the same way as what happens with the characteristic eigenvalues of the PEC cylinder (Fig. 3.4) and the PEC sphere

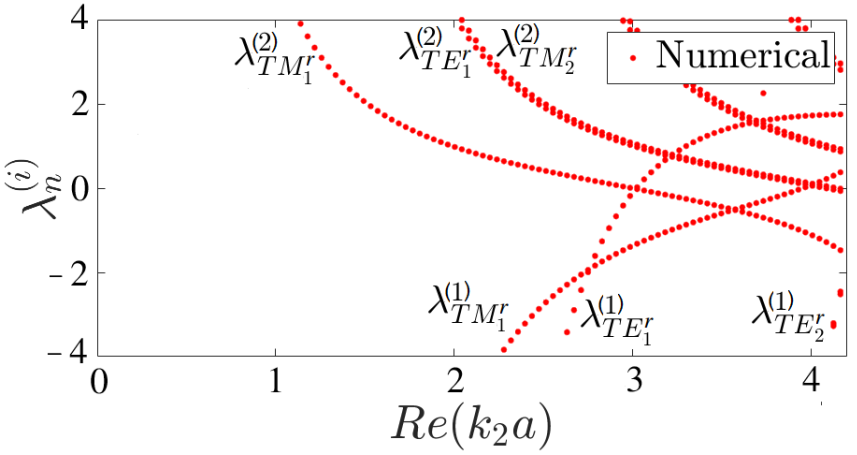

Fig. 4.9 Numerical characteristic eigenvalues for the dielectric sphere. The relative permittivity of the sphere is $\varepsilon_{r_2} = 9$ and the outer media is considered vacuum.

(Fig. 3.7), the same applies when comparing the characteristic eigenvalues of the dielectric cylinder (Fig. 4.10) and the dielectric sphere (Fig. 4.9). They have the same form. Thus, this shows that the same conclusions can be drawn for 3D dielectric bodies from the analysis of the infinite dielectric circular cylinder, i.e., a 2D analysis.

4.3.3 Natural Resonances vs Characteristic Mode Resonances

To demonstrate that NRs are different from CMRs, Table 4.3 shows some of the resonances obtained by both procedures plotted in Figs. 4.8 and 4.9.

Table 4.3 NRs $Re(k_2a)$ for the first mode $(m = 1)$, poles $(n = 1,2)$, for the dielectric sphere graphed in Fig. 4.8.. External CMRs for the dielectric sphere obtained from $\lambda_{TM_n^r}^{(1)}$, $\lambda_{TM_n^r}^{(2)}$, $\lambda_{TE_n^r}^{(1)}$ and $\lambda_{TE_n^r}^{(2)}$ curves in Fig. 4.9.

$Re(k_2a)$	NRs $m = 1$		CMRs $\lambda_X^{(1)}$		CMRs $\lambda_X^{(2)}$	
n	$TM_{n,1}^r$	$TE_{n,1}^r$	$TM_{n,1}^r$	$TE_{n,1}^r$	$TM_{n,1}^r$	$TE_{n,1}^r$
1	4.37	3.05	3.95	3.02	2.99	4.08
2	5.32	4.37	5.28	4.32	4.15	XXX

These external CMRs correspond to the zero crossings of the characteristic eigenvalues. As can be seen from Table 4.3 the real part of the NRs are different from their corresponding CMRs. The difference decreases as the mode considered is of greater order.

To end up with this analysis, a sphere of radius $r = 1\ cm$ studied in [68] is compared with the CMRs obtained for $\varepsilon_r = 10$ and $\varepsilon_r = 100$. This shows the dependence between the relative permittivity used and the existing percentage difference between the NRs and the CMRs for the first mode, $TE^r_{1,1}$

Table 4.4 Percentage difference comparison between the NR frequency and the CMR frequency of the $TE^r_{1,1}$ mode.

$Re(k_2a)$	CMR (GHz)	NR (GHz)	Percentage Difference (%)
$\varepsilon_r = 10$	4.5468	4.4840	1.38
$\varepsilon_r = 100$	1.4881	1.4853	0.19

As the permittivity increases, the percentage difference decreases. It can be concluded that NRs and CMRs are different, and this difference depends on the relative permittivity used.

4.4 Non-physical Characteristic Mode Contribution

The objective of this section is to demonstrate that the so-called *non-physical* modes can contribute to the electromagnetic field. Thus, it will be enough to find a case for which these modes contribute to the total field, forcing us to rethink the physical interpretation of these modes. Therefore, the simplest case of a centered line source in the middle of the dielectric circular cylinder will suffice to this purpose.

As it will be discussed later, since the total electric and magnetic current distributions are function of their characteristic currents, it is useful to write equation (4.26) as a function of their electric and magnetic characteristic currents, $J_n^{\lambda_n^{(i)}}$ and $M_n^{\lambda_n^{(i)}}$ respectively.

$$\begin{bmatrix} X & N_{im} \\ N_{im}^t & B \end{bmatrix}_n \begin{bmatrix} J_n^{\lambda_n^{(i)}} \\ M_n^{\lambda_n^{(i)}} \end{bmatrix} = \lambda_n^{(i)} \begin{bmatrix} R & N_{re} \\ N_{re}^t & G \end{bmatrix}_n \begin{bmatrix} J_n^{\lambda_n^{(i)}} \\ M_n^{\lambda_n^{(i)}} \end{bmatrix} \tag{4.29}$$

In equation (4.29), X, B, R, G, N_{im} and N_{re} are the general tangential operators used from the PMCHWT formulation in [28]. It is important to emphasize that since each *n-th* mode has associated a system of two equations with two unknowns, it will involve two eigenvalues and two characteristic eigencurrents.

These two solutions can be obtained for each *n-th* mode independently of the other modes solving (4.29), where $i = 1,2$ is the index to distinguish the two solutions.

Now, let us consider as an example a non-magnetic cylinder of radius $a = 5$ mm and permittivity $\varepsilon_{r_2} = 9$. The outer media is assumed vacuum. See Fig. 4.1. Next, the characteristic eigenvalues of the cylinder will be studied to check whether the so-called *non-physical* modes contribute to the electromagnetic field, and whether or not removing these solutions influence the accuracy of the resulting fields.

The characteristic eigenvalues of the cylinder are shown in Fig. 4.10. These analytical eigenvalues $\lambda_n^{(i)}$, corresponding to matrix (4.25) using equations (4.7-4.10) and (4.11-4.14), are obtained using (4.29). $\lambda_n^{(i)}$ are compared with those obtained numerically using FEKO [45]. Note that a 1-dimensional periodic boundary condition and the surface equivalence principle were used to simulate an infinite cylinder with FEKO. Fig. 4.10 shows an excellent agreement between the numerical and the analytical solutions. Those few points scattered outside the curve are due to purely numerical errors, since they do not fit with the curves obtained analytically.

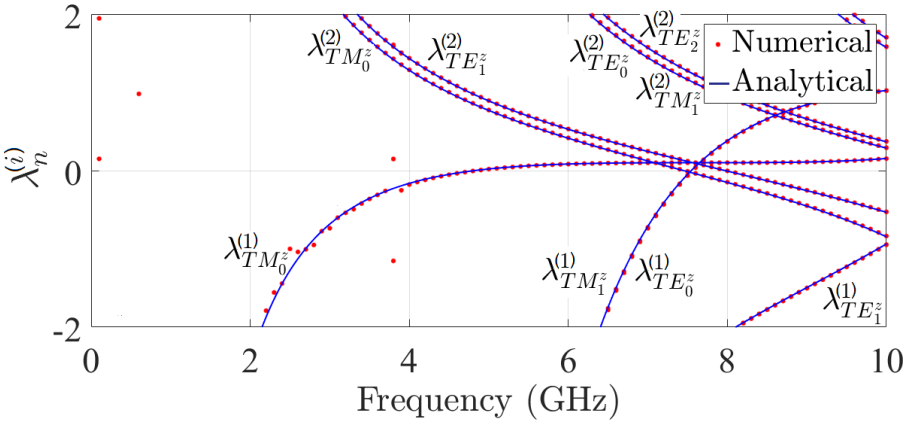

Fig. 4.10 Comparison between analytic and numerical characteristic eigenvalues for the infinite dielectric circular cylinder

As Fig. 4.10 shows, two types of curves can be clearly distinguished: curves with negative slope and curves with positive slope. Negative slope curves in this context are referred to as *non-physical* mode eigenvalues and positive slope

curves as the physical ones. To distinguish one eigenvalue from the other, superscripts (1) and (2) in $\lambda_n^{(1)}$ and $\lambda_n^{(2)}$, have been used for physical and *non-physical* modes, respectively. Furthermore, each eigenvalue has its associated subscript indicating the polarization type and the order of the cylindrical harmonic solution, e.g., TM_0^z. It is interesting to see that eigenvalues corresponding to TE_0^z and TM_1^z coincide. Turning to the *non-physical* modes, this term was adopted in [8] because they do not satisfy the far field orthonormality condition (4.30) associated to the scattered characteristic far fields $\mathbf{E}_n$ and $\mathbf{E}_m$.

$$\frac{1}{\eta}\iint \mathbf{E}_m \mathbf{E}_n^* ds = \delta_{m,n} \tag{4.30}$$

Rather than obtaining a value of unity when $m = n$, the researchers in [8] observed that the numerical evaluation of equation (4.30) on *non-physical* modes produced close-to-zero values instead.
However, this analytical study reveals that, at least for a 2D circular cylinder, an accurate computation of the far field under normal incidence leads to zero when computing equation (4.30) for all *non-physical* modes and for any given frequency. These results have been obtained using equations (4.31) for TM_n^z and (4.32) for TE_n^z incidence.

$$\begin{aligned} E_n^z = &-\sqrt{\frac{j}{8\pi k_1}}\frac{e^{-jk_1\rho}}{\sqrt{\rho}} \\ &\oint_0^{2\pi}\left(\omega\mu_0 \mathbf{J}_n\cdot\widehat{\mathbf{z}} - k_1\mathbf{M}_n\cdot\widehat{\boldsymbol{\phi}}\right)e^{-jk_1\rho' cos(\phi-\phi')}d\phi' \end{aligned} \tag{4.31}$$

$$\begin{aligned} E_n^\phi = &\sqrt{\frac{j}{8\pi k_1}}\frac{e^{-jk_1\rho}}{\sqrt{\rho}} \\ &\oint_0^{2\pi}\left(k_1\mathbf{M}_n\cdot\widehat{\mathbf{z}} + \omega\mu_0 \mathbf{J}_n\cdot\widehat{\boldsymbol{\phi}}\right)e^{-jk_1\rho' cos(\phi-\phi')}d\phi' \end{aligned} \tag{4.32}$$

In fact, what happens is that fields radiated by the equivalent electric and magnetic currents in (4.31) and (4.32) cancel each other for the *nonphysical* modes when $m = n$. So there is no field radiated by these *non-physical* modes. Therefore, as a first conclusion, it would be inappropriate to say that condition

(4.30) is not met for the *non-physical* modes since in reality there is no radiation at all from these modes.

As is well known [28], the scattered field can be expressed as the sum of the fields scattered by all characteristic currents. In view of previous result, the question arises about whether these modes contribute to the total field in the different regions involved and even whether the location of the source with respect to the dielectric body (inside or outside) may play a role in their contribution. As it will be demonstrated in the next section, the term *non-physical* may not be completely appropriate for these modes since it is found that they do contribute to the total electric field within the cylinder when the source is also within it.

4.4.1 On the Contribution to the Field of the Two PMCHWT Eigensolutions.

To understand better the eigencurrents associated to eigenvalues $\lambda_n^{(1)}$ and $\lambda_n^{(2)}$, it is necessary to go deeper into the formulation. The *i-th* eigenvector of equation (4.29) is related to the *i-th* eigenvalue. These eigenvectors form a weighted orthonormal set over the material body surface. Furthermore, the two eigenvectors of each n mode combine to get the total induced current distribution when an excitation field is considered. Depending on the location of the source (internal or external to the surface of the cylinder), the $i = 1$ and the $i = 2$ eigenvectors will be excited or not. Each *i-th* eigenvector is a characteristic mode. An expression for the total induced current distribution as a function of the CMs can be written as follows,

$$\begin{bmatrix} J \\ jM \end{bmatrix} = \sum_{n=-\infty}^{\infty} \sum_{i=1}^{2} \gamma_i^n \begin{bmatrix} J_n^{\lambda_n^{(i)}} \\ jM_n^{\lambda_n^{(i)}} \end{bmatrix} \{\cos(n\phi), \sin(n\phi)\} \tag{4.33}$$

where the excitation coefficients are

$$\gamma_i^n = \frac{\begin{bmatrix} J_n^{\lambda_n^{(i)}} & jM_n^{\lambda_n^{(i)}} \end{bmatrix} \begin{bmatrix} E^{inc} \\ jH^{inc} \end{bmatrix}}{(1+j\lambda_n^{(i)})} \tag{4.34}$$

Thus, the total current is given by the corresponding excited CMs given by the two *i-th* solutions. Therefore both *i-th* eigenvectors and eigenvalues have to be taken into account. The analytical results for the total current distribution considering equation (4.33) for an external or an internal incident field are presented below.

On the one hand, Figs. 4.11(a) and 4.11(b) show the total electric and magnetic equivalent currents obtained for a TM^z plane wave impinging normally on the dielectric cylinder surface at $f = 4$ GHz. To calculate the total current distribution using equation (4.33), the incident plane wave was written in terms of cylindrical wave functions.

$$\mathbf{E}^{inc} = E_0 \sum_{n=-\infty}^{+\infty} j^{-n} J_n(k_1\rho) e^{jn\phi} \widehat{z} \tag{4.35}$$

$$\mathbf{H}^{inc} = E_0/\eta_1 \sum_{n=-\infty}^{+\infty} j^{-(n+1)} J_n'(k_1\rho) e^{jn\phi} \widehat{\phi} \tag{4.36}$$

Either in Fig. $4.11(a)$ or $4.11(b)$, the contribution of the *non-physical* solution to the total current is found to be exactly zero. It can be seen that when the TM^z excitation is considered, only the solution with $i = 1$ contributes to the total current distribution. Although obvious, it is important to point out that since the contribution of *non-physical* modes to the total current is zero, their contribution to the electromagnetic field will equally be zero, either inside or outside the cylinder.

Let us consider now an electric line source within the cylinder. The source is located along the z-axis for simplicity. As in the example above, equation (4.33) is used, but now the incident electric and magnetic fields are,

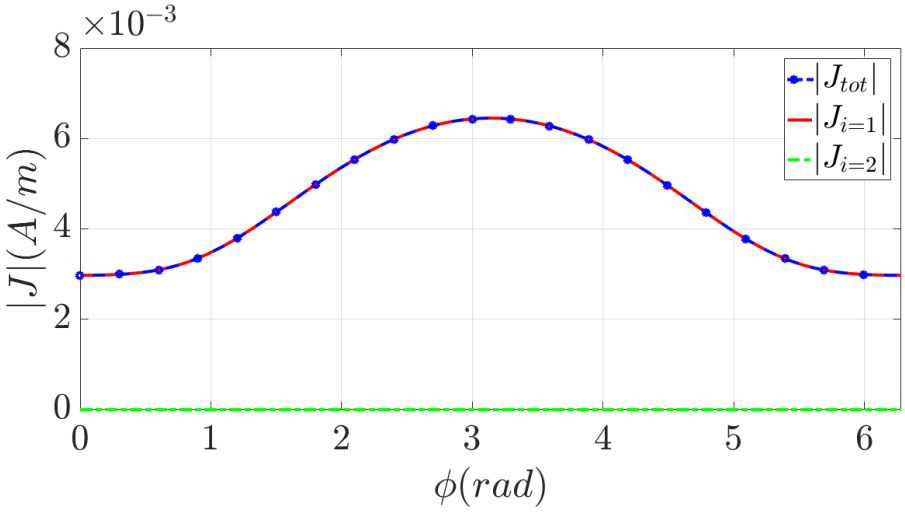

((a))

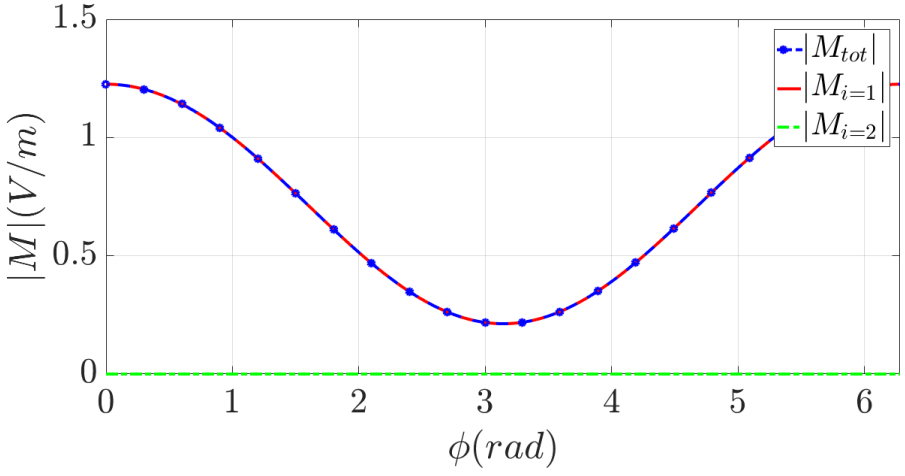

((b))

Fig. 4.11 Contribution of each eigensolution when impinging by a normally incident TMz plane wave: (a) To the total electric current. (b) To the total magnetic current.

$$\mathbf{E}^{inc} = -\frac{k_2\eta_2 I}{4}H_0^{(2)}(k_2\rho)\widehat{z} \tag{4.37}$$

$$\mathbf{H}^{inc} = \frac{k_2 I}{4j}H_1^{(2)}(k_2\rho)\widehat{\phi} \tag{4.38}$$

The goal is to know whether *non-physical* modes are excited or not. Since the excitation is rotationally symmetric, so are the equivalent currents and only TM_0^z mode contributes to the total field. Table 4.5 shows amplitude and phase of the total electric and magnetic equivalent currents obtained for this case. Results were obtained for a frequency of 4 GHz. Unlike for a plane wave, in this case both characteristic mode solutions, $i = 1$ and $i = 2$, do contribute to total equivalent currents. Both modes are meaningful under this sort of excitation. Letter X in Table 4.5 is used to simplify notation and stands for electric, $\mathbf{J}$, or magnetic current, $\mathbf{M}$.

Table 4.5 Contribution of each eigensolution to the total electric $\mathbf{J}$ and magnetic current $\mathbf{M}$ for an electric line source excitation located on the z-axis. Abs (A/m) and Phase (rad).

[Abs, Phase]	$X = \mathbf{J}$	$X = \mathbf{M}$
$\gamma_1^0 X_0^{\lambda_0^{(1)}}$	[2.8732e+10, 2.9148]	[4.5211e+12, 1.3441]
$\gamma_2^0 X_0^{\lambda_0^{(2)}}$	[3.1861e+08, 1.8454]	[5.6004e+11, 0.2746]
$\sum_{i=1}^{2} \gamma_i^0 X_0^{\lambda_0^{(i)}}$	[2.8887e+10, 2.9052]	[4.8154e+12, 1.2419]

Now, the electric field radiated by the physical ($i = 1$) and *non-physical* ($i = 2$) solutions produced by the currents in Table 4.5 are obtained. Equations (4.39) and (4.40) are the scattered outer and inner electric fields, respectively. These fields are obtained in terms of the CMs $i = 1$ and $i = 2$.

$$E^z_{scat,out} = \frac{\eta_1 \pi k_1 a}{2} J_0(k_1 a) H_0^{(2)}(k_1 \rho) \sum_{i=1}^{2} \gamma_i^0 J_0^{\lambda_0^{(i)}} + \frac{k_1 \pi a}{2j} J_1(k_1 a) H_0^{(2)}(k_1 \rho) \sum_{i=1}^{2} \gamma_i^0 M_0^{\lambda_0^{(i)}} \tag{4.39}$$

$$E^z_{scat,in} = -\frac{\eta_2 \pi k_2 a}{2} J_0(k_2 \rho) H_0^{(2)}(k_2 a) \sum_{i=1}^{2} \gamma_i^0 J_0^{\lambda_0^{(i)}} - \frac{k_2 \pi a}{2j} J_0(k_2 \rho) H_1^{(2)}(k_2 a) \sum_{i=1}^{2} \gamma_i^0 M_0^{\lambda_0^{(i)}} \tag{4.40}$$

Figs. 4.12(a), 4.12(b) and 4.12(c) show these fields graphically as a function of the radial distance to the origin, ρ. Fig. 4.12(a) shows the total electric field. It includes the contribution of the line source and the equivalent currents. As expected, the field is continuous at the surface interface, $\rho = 5$ mm. Figs. 4.12(b) and 4.12(c) show the scattered electric field generated by the equivalent currents $i = 1$ and $i = 2$, respectively. Notice that a different scale was used in Fig. 4.12(c) for clarity. It is worth noticing that the outer scattered field radiated by the equivalent current corresponding to $i = 2$ is zero. This current only contributes to the inner scattered field, $\rho < 5$ mm.

For the sake of completeness, it is also interesting to show the behavior of the magnetic field radiated by the physical ($i = 1$) and *non-physical* ($i = 2$) solutions produced by the currents in Table 4.5, as done for the electric field. Equations (4.41) and (4.42) are the scattered outer and inner magnetic fields, respectively. These fields are obtained in terms of the CMs $i = 1$ and $i = 2$.

$$
\begin{aligned}
H^z_{scat,out} = &-\frac{\pi k_1 a}{2j} J_0(k_1 a) H_0^{\prime(2)}(k_1\rho) \sum_{i=1}^{2} \gamma_i^0 J_0^{\lambda_0^{(i)}} \\
&+\frac{k_1 \pi a}{2\eta_1} J_1(k_1 a) H_0^{\prime(2)}(k_1\rho) \sum_{i=1}^{2} \gamma_i^0 M_0^{\lambda_0^{(i)}}
\end{aligned}
\tag{4.41}
$$

$$
\begin{aligned}
H^z_{scat,in} = &\frac{\pi k_2 a}{2j} J_0^{\prime}(k_2\rho) H_0^{(2)}(k_2 a) \sum_{i=1}^{2} \gamma_i^0 J_0^{\lambda_0^{(i)}} \\
&-\frac{k_2 \pi a}{2\eta_2} J_0^{\prime}(k_2\rho) H_1^{(2)}(k_2 a) \sum_{i=1}^{2} \gamma_i^0 M_0^{\lambda_0^{(i)}}
\end{aligned}
\tag{4.42}
$$

The same behaviour can be observed for the magnetic field. Figs. 4.13(a), 4.13(b) and 4.13(c) show these fields graphically as a function of the radial distance to the origin, ρ.

Following the discussion in previous section, these results support the motive for which the so-called *non-physical* modes do not comply with the orthonormality condition (4.30). There is no electromagnetic radiation from *non-physical* characteristic mode outside the cylinder surface. Therefore they should be named more properly as *non-radiating* modes instead, since they do contribute to inner fields when source is inside.

These analytical results allow us to understand better the characteristic eigenvalues obtained numerically from the PMCHWT formulation in previous studies, when analyzing an infinite dielectric circular cylinder. These conclusions are independent of frequency, material or radius used for the cylinder.

Due to the presented similarities between the infinite circular dielectric cylinder and the dielectric sphere provided in this Chapter, it is expected that the problem of a dielectric sphere with a spherical point source centered on its interior can also excite *non-physical* modes. It is therefore important to perform a review of excitation mechanisms in dielectric resonators whose source is inside when using the PMCHWT formulation. Since if one of the two families of solutions obtained by the theory of CMs is eliminated, it is very probable

that an error is made in the total equivalent currents **J** and **M**, and therefore, an error in its associated total electromagnetic field.

The resonances of the *non-physical* modes have not been considered in the next chapter, since the excitation used is a slot, and this is not located within the surface defined by the dielectric resonator.

4.5 Conclusions

In summary, it has been shown that CMRs are different from NRs, for both an infinite circular cylinder and a dielectric sphere. At most, and depending on the relative permittivity considered, CMRs might be used as a first guess in an internal NR search in the complex frequency plane. In addition, CMRs only predict internal NRs because of their proximity to the $Re(k_2 a)$ axis. The differences between CMRs and internal NRs depend on relative permittivity. Large ε_{r_2} provide closer values. This is due to a decrease in the dumping factor of a given particular mode. Besides, it has been observed that the difference between both CMRs and internal NRs also depends on the particular electromagnetic mode considered. The analysis has been performed analytically for the cylinder and numerically for the sphere. the analytic one provides the accurate analytical solutions required to establish reliable observations. Notice that subtle resonance differences between the two families of modes has led other authors to misinterpretations.

On the other hand, the object of this chapter has been to analyze accurately and to clarify the underlying physics of the two characteristic mode solutions provided by the PMCHWT formulation for dielectric bodies. For that purpose, the dielectric cylinder has been studied to take advantage of the fact that we had its analytical solution, furthermore, it is worth mentioning that this study could not have been done numerically using the electromagnetic suite FEKO [45] because *non-physical* solutions are no longer available in its software. For such canonical problem, the analytical solution cuts out from the results interpretation any shadow associated to numerical errors. Thanks to that, it has been possible to demonstrate that all solutions provided by the PMCHWT formulation have indeed a physical meaning. This was necessary since, to date, there has been doubts on certain mathematical solutions of this formulation which were classified as *non-physical*. In reality so-called *non-physical* modes

do contribute to the field within the cylinder when the excitation is also in it. Therefore it would be more appropriate to qualify them as *non-radiating* modes.

It is important to emphasize that the results obtained in this chapter do not contradict the key finding in [8] regarding the *non-radiating* nature of their *non-physical* modes for 3D arbitrary geometries, only that these solutions do not have to be eliminated. In fact it supports it and clarifies the cause behind these modes not satisfying the field orthogonality relation. Likewise, it is reasonable to infer that *non-radiating* modes will also contribute too to the field within a 3D arbitrary structure when the source is within it, as they do for the cylinder, since the cause of it lays on the properties of the PMCHWT integro-differential operator, not in the geometry itself. Certainly this statement will require a numerical proof but this is left for future work.

After the conclusions obtained in this chapter, it is of interest to develop a DRA design method in which to design with low permittivities does not become a problem. Moreover, it is also of interest to present a method in which the CMRs include part of the feeding. This can be done in order to obtain more realistic resonances compared with those obtained from the S11 antenna parameter, which also considers the feeding. This will be presented in the next chapter.

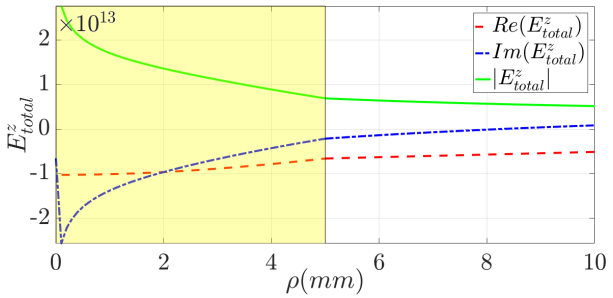

((a))

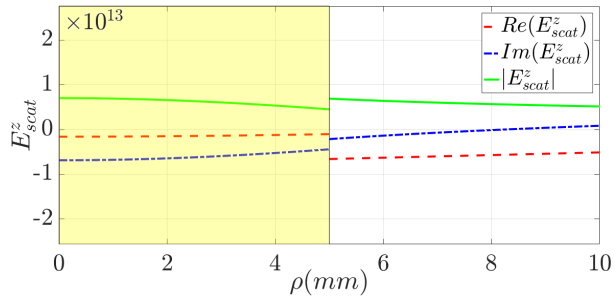

((b))

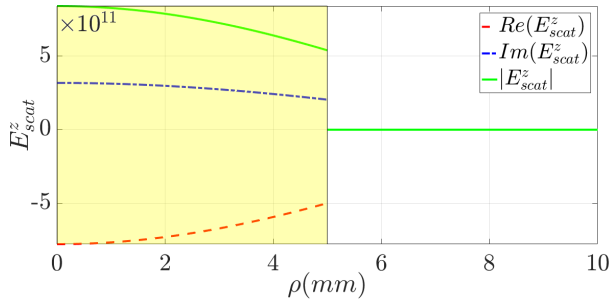

((c))

Fig. 4.12 Electric field contribution inside and outside the cylinder by the two equivalent currents when fed by an electric line source in the z-axis ($f = 4$ GHz, $a = 5$ mm, $\varepsilon_{r_2} = 9$): (a) Total electric field . (b) Scattered field due to the $i = 1$ equivalent currents. (c) Scattered field due to the $i = 2$ equivalent currents (*non-physical* modes solution).

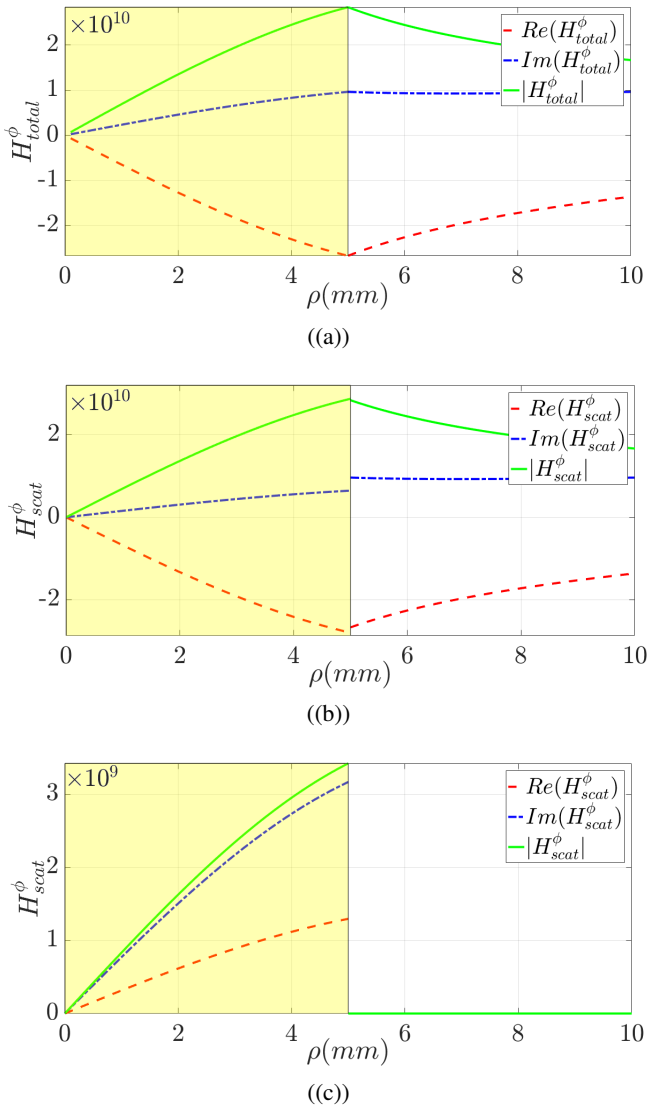

Fig. 4.13 Magnetic field contribution inside and outside the cylinder by the two equivalent currents when fed by an electric line source in the z-axis ($f = 4$ GHz, $a = 5$ mm, $\varepsilon_{r_2} = 9$). (a) Total magnetic field. (b) Scattered field due to the $i = 1$ equivalent currents. (c) Scattered field due to the $i = 2$ equivalent currents (*non-physical* modes solution).

Chapter 5

Dielectric Resonator Antenna Design

In this chapter, two methods to design a rectangular dielectric resonator antenna (RDRA) are presented. These methods are based on the TCM. The first method designs a RDRA using the VIE formulation and uses as excitation a slot-coupled to a microstrip line. The method is fairly straightforward and intuitive but leads to somehow inaccurate results due to errors in determining DR resonance for low permittivities. The second method is more robust and designs a RDRA using the concept of substructure characteristic modes. PMCHWT formulation will be used for the DR while the planar multilayer Green's function (PGF) formulation is used on the feeding slot in a ground plane (called bellow as SGP). Unlike the first method, the slot is excited now by a coplanar waveguide (CPW). Both designs have been realized to work for the ISM-band at 60 GHz. Both methods excites the same TE^{y}_{111} mode inside the RDRA. This has been done in order to force radiation as a magnetic dipole. Moreover, both methods are applied on low permittivity DRs. It is worth mentioning that the antennas are designed assuming the manufacturing characteristics of the LTCC technology, with the purpose of manufacturing later in a single sintering process. So therefore, the design procedure have been adapted to fully exploit the possibilities of the LTCC technology. Additionally, the topics covered in the previous chapter will be discussed in practice. It will be seen that the non-radiating modes do not impair the interpretation of the solutions in these more complex structures.

Also, it will become clear the shift in resonance frequency of the resonances obtained from the characteristic eigenvalues with respect to the internal NRs.

5.1 Introduction

In recent years, research in wireless communications technology at 60 GHz is increasing to meet the demand of shared gigabytes between mobile devices. Applications require miniaturization, portability, low cost in the manufacturing process and high packaging grade. Especially at these frequencies, the dielectric resonator antenna (DRA), introduced by Long in 1983 [76], allows these characteristics and avoid losses in the metal produced by millimeter waves. In addition, the DRA have other features as greater bandwidth, easy feeding, high radiation efficiency and easy fabrication [96]. They are mounted on a ground plane or on a grounded dielectric substrate of lower permittivity. Furthermore, DRAs can be fed with different excitation mechanisms such as slots [64], coaxial probes [63], waveguides [2], and image lines [3].

As a multilayer mass production and low cost technology, low temperature sinterized ceramic (LTCC, low temperature cofired ceramics) might be an option for manufacturing these antennas [51]. DRAs are usually manufactured with ceramic materials and the possibility to include the DRA in the same manufacturing process becomes interesting [52]. LTCC offers many features and possibilities as vertical integration of an arbitrary number of layers. The low loss nature of these substrates at microwave and millimeter-wave frequencies makes LTCC a very interesting manufacturing technology. Moreover, this manufacturing process allows us to fabricate the model at very low permittivies compared to what is usually employed for DRAs. The benefits of using low permittivities is to have the possibility of widening the impedance bandwidth [95].

To date, the design of DRAs has been done mainly through the magnetic-wall model (MWM) [85]. This model uses a formula that relates the DR dimensions to its resonant frequency. However, it is a model that is limited to canonical geometries and, in addition, an error of up to 20 % can be expected when it is intended to design on low permittivities (around $\varepsilon_r = 10$). This model has been widely used for the design of filters, whose permittivities are much higher. Along with the MWM, there are also other conventional procedures

to design DRAs. For example, numerical methods, as the eigenmode solver based on the finite element method (FEM) [17] and integral equations methods based on the MoM [61], among others. These methods are more precise than the MWM, and have the possibility to extend the models to more general geometries. In recent years, however, DRA has begun to be designed with the help of TCM. It is noteworthy that after the success in recent years designing conducting antennas with TCM [24], this theory is currently being extended to the design of DRAs [18, 20, 46, 47]. So far, there are not many examples, but they are growing every day because TCM plays an important role when looking for the resonances of dielectric cavities, or just to understand better their radiating nature. The fact is that, unlike the rest of methods, CM provides a physical interpretation of the radiation for a given structure. Therefore, the TCM becomes promising because it is not necessary to study the resonances in the complex frequency plane, since its solutions are on the real axis. In addition, the extension to other non-canonical geometries is straightforward. Another advantage of designing with the TCM is the flexibility it provides when it comes to manipulating its matrix operators. Yet, although there has been some difficulties in interpreting their solutions in dielectrics as discussed in previous chapters, it still is an appealing tool for antenna engineers. Therefore, if these difficulties are solved, the TCM will become even more interesting for dielectric-based antennas design.

The main difficulties encountered throughout this thesis have been solved in this chapter, and they are the following:

- Some *non-radiating modes* appear when using the PMCHWT formulation and it is important to know their exact role before proceed to design.

  As shown in chapter 4, the *non-radiating modes* do not have to be removed because due to their non-radiating nature, they contribute only to the DR inner field, and only in the case it is fed from the inside. So, as far as this subject is concerned, this issue is resolved.

- For low permittivities the resonances provided by the TCM are very different to the NRs. This resonance frequency shift can be solved as follows:

  It is possible to circumvent this problem using the concept of characteristic modes of substructures that was first proposed in [43]. Here, it is

applied to DRA design. This concept allows us to determine accurately the characteristic modes of a given structure pertubed by the surrounding structures. In this way, a more realistic computation of resonances is done in comparison with the isolated DR case. To carry out this procedure, use is made of the characteristic modes of the Schur complement of the DR and the SGP sub-matrices of the impedance matrix obtained from MoM. This extension takes into account the behavior of the SGP in the presence of the DR, and vice versa. Therefore it is possible to design the DR and the SGP at the same time. Moreover, it gives information about the DRA that with the VIE-method, or other conventional methods, cannot be obtained.

5.2 VIE-Method

The method involves two parts. In the first part the isolated DR is designed by the TCM based on the VIE formulation. The DR is assumed to be on an infinite ground plane. The second part of the method includes the other components that conform the antenna. These are a slot, a substrate, and the microstrip line. These will be added after the CMA design of the isolated DR.

5.2.1 Rectangular DR Design Procedure

The EFIE-VIE integro-differential operator presented in Section 2.3 will be used. For that purpose the electromagnetic software FEKO and MatLab have been linked to extract in Matlab the characteristic eigenvalues, eigenvectors and eigenfields. This can be done from the impedance matrix provided by FEKO, since FEKO internally uses the EFIE-VIE.

The design procedure is sketched in Fig. 5.1.

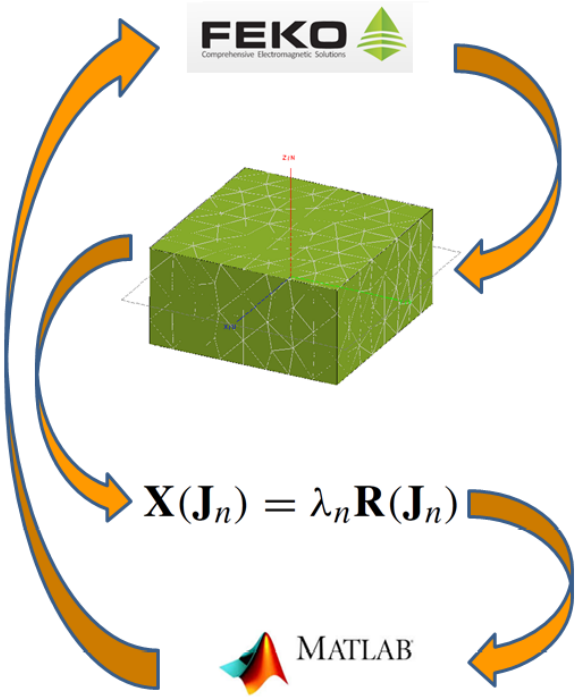

Fig. 5.1 Numerical procedure used to find the characteristic eigenvalues and eigenmodes of the rectangular DR.

The steps taken for the DR design are summarized in the following:

1. A model is created in FEKO defining the frequency, materials, and the 3D geometry of the DR. Selection is made of the solver, VIE in this case. The DR is meshed with tetrahedral volume elements.

2. MATLAB imports the data from the impedance matrix calculated by FEKO. Data is post-processed using the equation that governs the TCM, (2.37). Perform the same procedure for each frequency. Graph the characteristic eigenvalues to check whether the eigenvalue of the main mode is in the required frequency range. If this goal is not achieved, return to FEKO (Step 1) and change the design parameters at your convenience to center the eigenvalue curve at the design frequency. Repeat this procedure as many times as necessary.

3. Observation is made of the associated characteristic currents of a particular eigenvalue, the characteristic vector associated with a characteristic eigenvalue is imported from MATLAB to FEKO by selecting it at a given frequency. With this, it is possible to visualize the current distribution in POSTFEKO. After introducing the characteristic currents in FEKO it is also possible to see its radiated far fields. If currents or fields do not have the desired distribution, change the geometry of the DR in FEKO (Step 1) and redesign it. This has to be done to try to meet the specifications of the antenna. Steps 2 and 3 go hand in hand.

4. The design process ends once the DR design goals are achieved.

Following the above design steps, the RDRA is designed with the initial specifications given below. Since the idea is to adapt the design procedure such that the possibilities of the LTCC technology is fully exploit with a minimum required number of layers, the DR has to show the same relative permittivity as the microstrip substrate, because both has to be fabricated in the same sintering process. Thus, the DR permittivity used is LTCC Ferro A6-M with $\varepsilon_r = 5.9$ and $tan\delta = 0.001$. Furthermore, the DR is designed for ISM-band at 60 GHz.

As shown in Fig. 5.2, the radiating element is designed on an infinite ground plane, as it will be present later when fed through a slot. The length, width and height of the DR are L, W and h, respectively. Note that the infinite PEC ground plane works as a mirror according to the Method of Images, and the DR height has to be reduced to half.

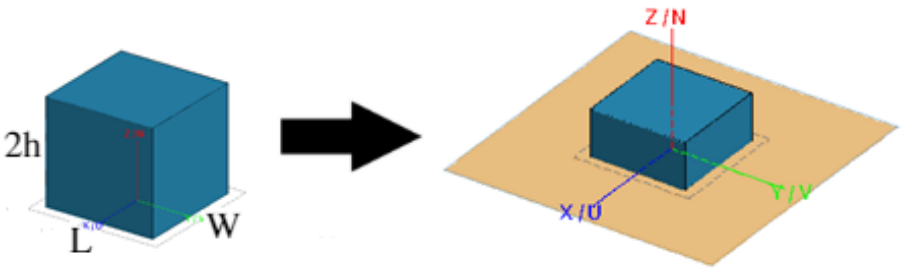

Fig. 5.2 Transformation of the DR to a half height DR on an infinite ground plane.

This trick allows us to reduce the computation procedure since the impedance matrix is reduced. Furthermore, in doing so, those electric modes parallel to the ground plane are eliminated. Therefore, the impedance matrix operator obtained from VIE will only have the information of interest related to the DR.

The next step now is to calculate the impedance matrix from the Matlab interface program and diagonalize them for each frequency. For the diagonalization we make use of the characteristic equation (2.37). The eigenvalues found are represented in Fig. 5.3.

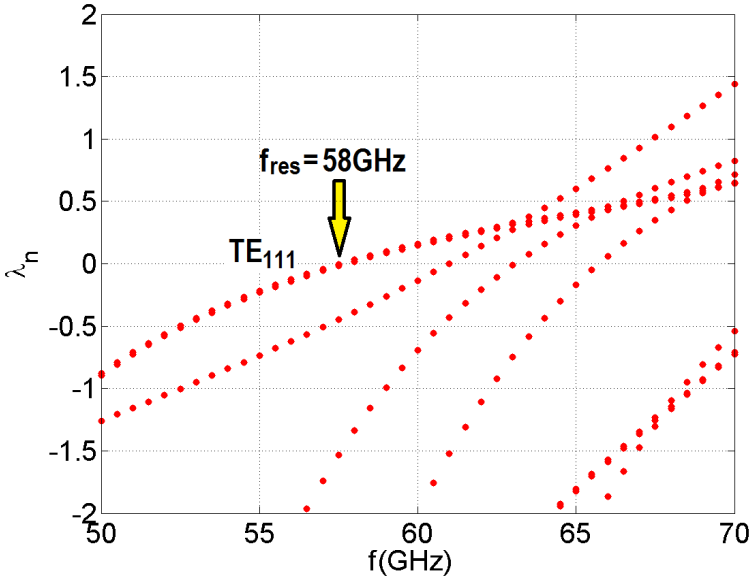

Fig. 5.3 Characteristic eigenvalues for the rectangular DR.

By definition, the resonant frequency can be found when $\lambda_n = 0$. Fig. 5.3 shows the TE_{111} mode resonating at 58 GHz. The final dimensions obtained from the eigenvalues for this rectagular DR are $L = W = 3$ mm and $h = 0.6$ mm (6 LTCC layers).

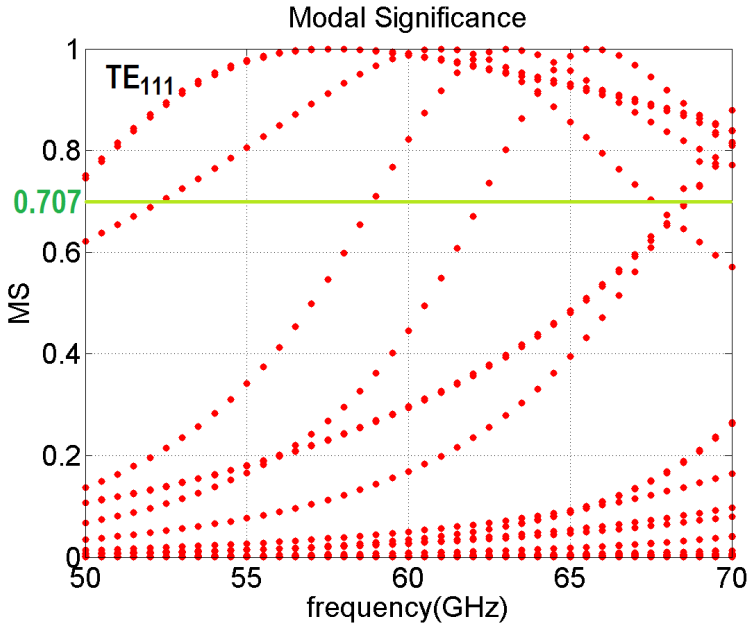

Fig. 5.4 Modal significance curves for the rectangular DR.

According to [85], the rectangular DR can have degenarated modes depending on the involved symmetries. In this case the height is smaller than the base dimensions, so the TE_{111} eigenvalue shown in Fig. 5.3 belongs to the TE^x_{111} and TE^y_{111} modes, since the TE^z_{111} will be resonating at upper frequencies. Thus, the eigenvalues for TE^x_{111} and TE^y_{111} modes are the same, and therefore they are degenerated.

Another useful way to see the resonances from the eigenvalues is using the modal significance defined by equation (2.12).

Fig. 5.4 represents the normalized amplitudes for the characteristic currents, independently of the excitation. As shown in Fig. 5.4, up to the horizontal green line located at $MS = 0.707$ the current modes radiate half the power. Because of this, it is easy to see the wide bandwidth for the degenerated TE^x_{111} and TE^y_{111} modes in relation to the other modes.

Let us see now the volumetric distribution currents for the TE^x_{111} and TE^y_{111} modes at 58 GHz.

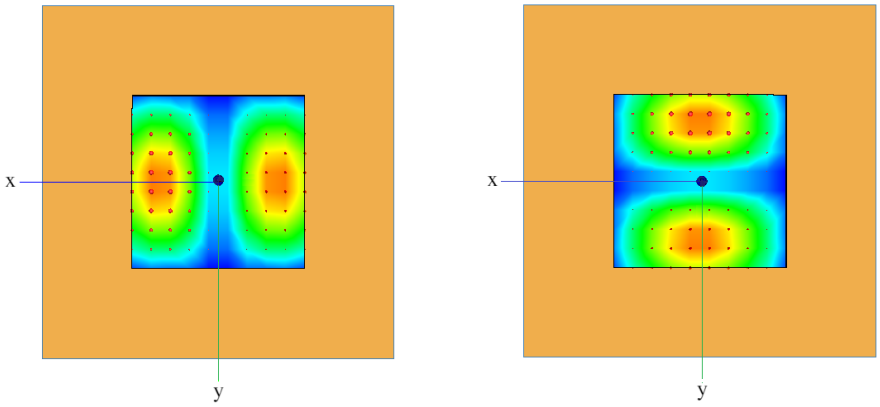

Fig. 5.5 Volumetric current distribution **J** at 58 GHz: Left TE^{y}_{111} mode. Right TE^{y}_{111}

Since the modes are degenerated, i.e. they share the same eigenvalue, their distribution currents have to be orthogonal to each other. Fig. 5.5 shows the electric currents **J**, of these two modes . If mode TE^{y}_{111} is selected, a proper location and orientation of the slot must be decided. For that, the easiest way is observing the orientation of the magnetic field at the ground level. Fig. 5.6 shows the electric and magnetic characteristic fields produced by the volumetric current distribution **J** at 58 GHz. Therefore, it is clear that the slot must be placed at the center of the DR and oriented along the *y*-axis.

5.2.2 RDRA Design Procedure

Let us now turn to the second part of the design in which we have to introduce a slot, the dielectric substrate and the microstrip waveguide responsible to feed the slot. Since the objective is to excite the TE^{y}_{111} mode we used a rectangular slot on the infinite ground plane to avoid the excitation of other modes. The interesting thing here is that the variables to be optimized have been reduced with the previous analysis of characteristic modes. And now the only task left is to match the microstrip line and the slot to the DR. It should not be forgotten that since an LTCC fabrication is in mind, the substrate will exhibit the same permitivity as the DR, and the height of the substrate will depend on the height of the layers after the co-firing, since LTCC is a technology of multi-layer packaging.

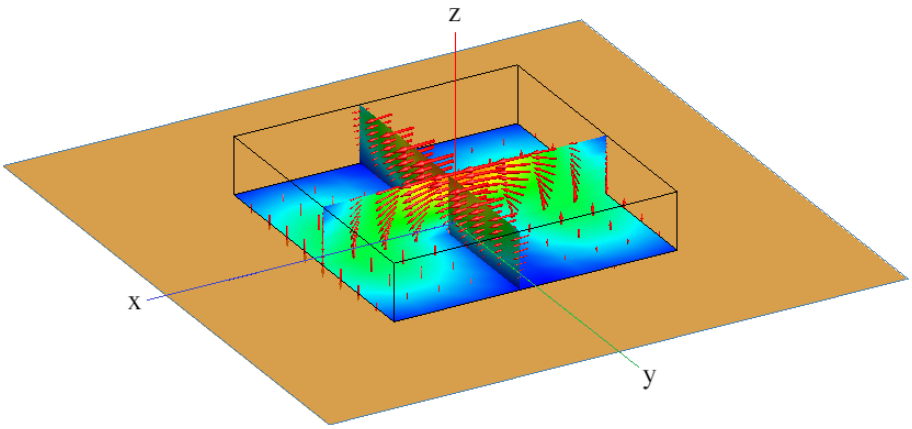

(a)

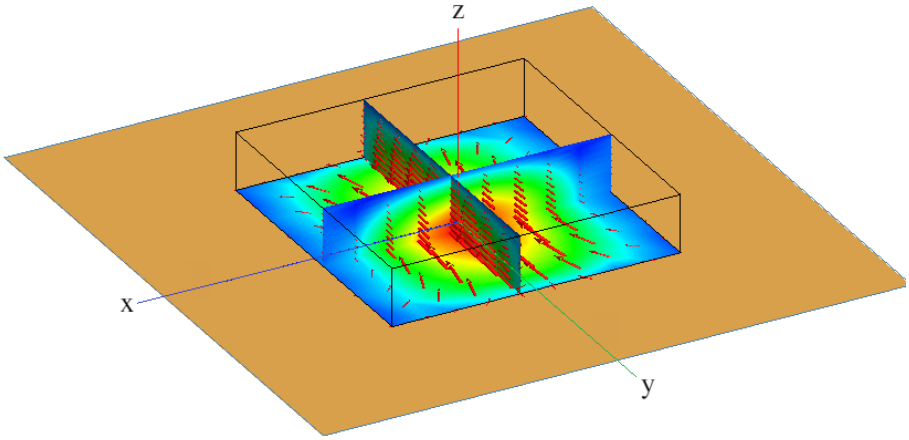

(b)

Fig. 5.6 Inner characteristic fields of the TE_{111} mode at 58 GHz. a) Electric field. b) Magnetic field.

Fig. 5.7 shows the FEKO scheme of a conventional slot-coupled RDRA. It can be seen that the microstrip line is oriented along the x-axis to couple the maximum amount of energy to the slot.

The substrate used is LTCC Ferro A6-M with $\varepsilon_r = 5.9$ and $tan\delta = 0.001$. After optimizing the antenna the height of the substrate is $d = 0.1$ mm (1 LTCC layer), the 50 Ω microstrip line has a width $W_m = 0.14$ mm, and the length for the stub is $L_s = 0.77$ mm. The slot dimensions are length $L_s = 1.5$ mm and width $W_s = 0.2$ mm. Therefore, considering the height of the DR, the whole antenna is constructed on a 7-layer LTCC model.

The simulated results are obtained with FEKO program. In Fig. 5.8, the reflection coefficient and the realized gain are shown. Due to the low permittivity of the RDRA, the bandwidth covers from 60 GHz to 70 GHz for $S_{11} < -10$ dB, reaching an impedance bandwidth of 33 % and covering the ISM band at 60 GHz. Fig. 5.9 illustrates the total electric and magnetic fields obtained after feeding through the microstrip coupled-slot at 58 GHz. We achieve the TE^{y}_{111} mode selected by using the TCM. Finally, the far field pattern for both, the *xz*-plane and the *yz*-plane are shown. This radiation pattern is that of a magnetic dipole as expected.

Finally, it is worth highlighting the difference between the resonance computed for the DR from the TCM at 58 GHz, and the one finally obtained for the DRA from the S_{11}, which is at 63 GHz. This difference is due to two causes. On the one hand, the previous chapter showed that using low permitivities the TCM produce an error with respect to the NR. The lower the permittivity the greater the difference between the two. On the other hand, since a slot, a substrate, and a microstrip line are added to the DR, a perturbation on the resonance of the DR appears. Of course, there is a big difference between these two resonances. While the resonances of the TCM are independent of the excitation, those provided by the S_{11} do depend on it. Anyway, how could we bring the characteristic resonance closer to that of the S_{11}? The answer to this question will be given in the next section.

A final point is that the same DRA design procedure, could have been carried out using a PMCHWT-SIE formulation instead of VIE. Since the eigenvalues obtained with the VIE formulation can be seen as a subset of those obtained with PMCHWT-SIE, exactly the same results would have been obtained. This is clearly shown in Fig. 5.11.
Unlike SIE solution, VIE provides one eigenvalue per mode for dielectrics. It is easy to see that in Fig. 5.11 the solution from VIE is contained in SIE.

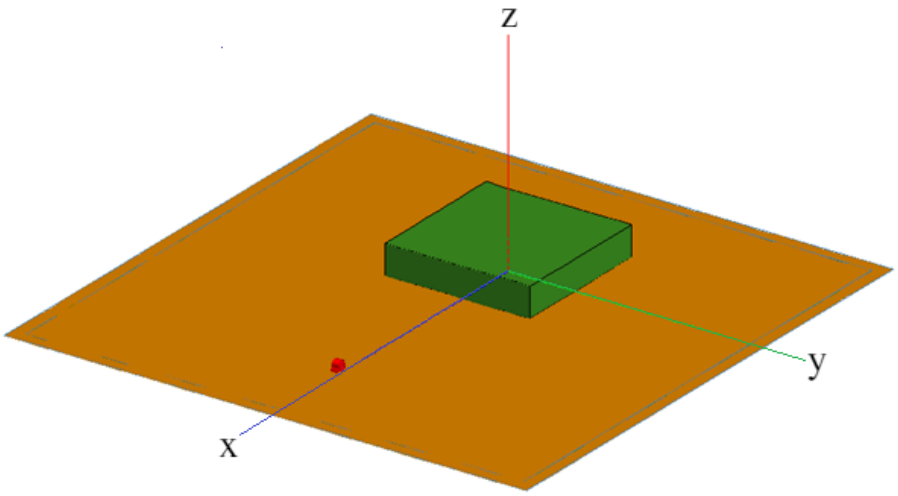

(a) Profile view

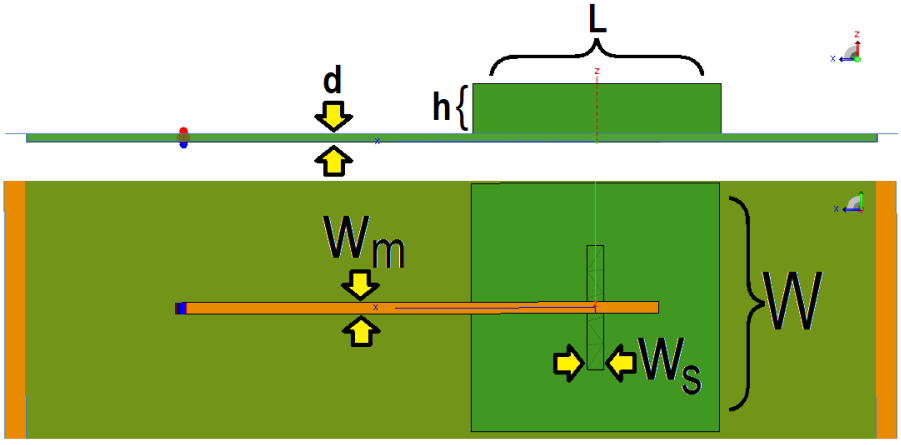

(b) Scheme

Fig. 5.7 Profile view and scheme of the microstrip slot-coupled RDRA

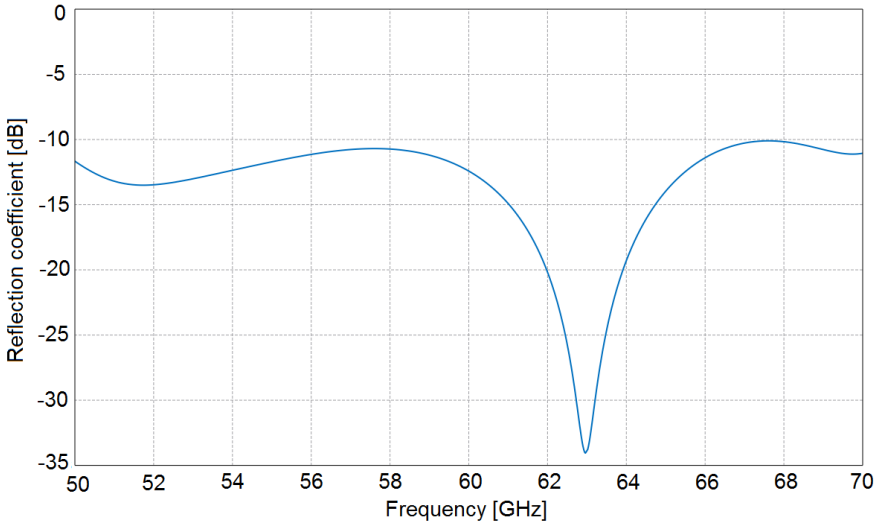

(a) Reflection coefficient

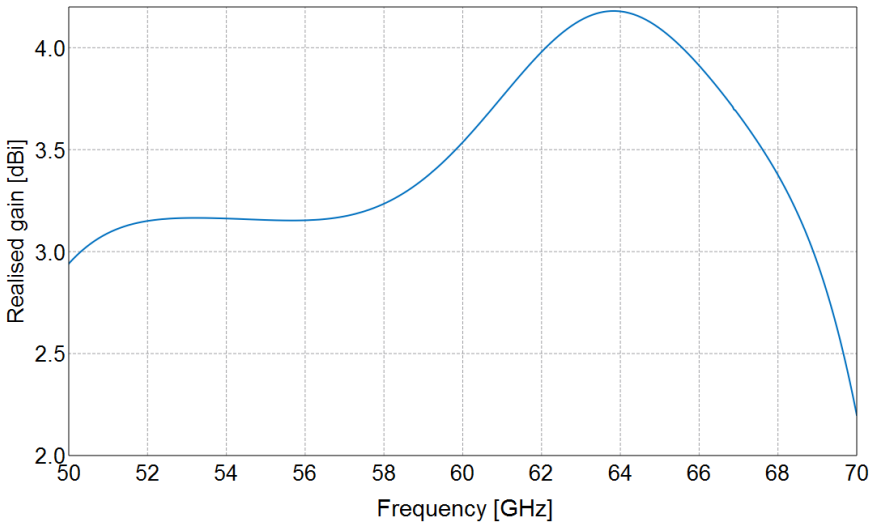

(b) Realised gain

Fig. 5.8 S11 and realized gain after considering the optimized parameters for the RDRA

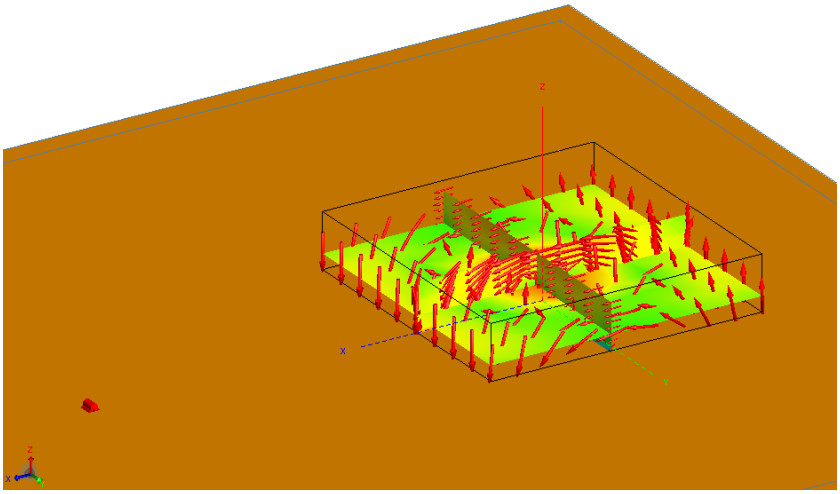

(a) Electric

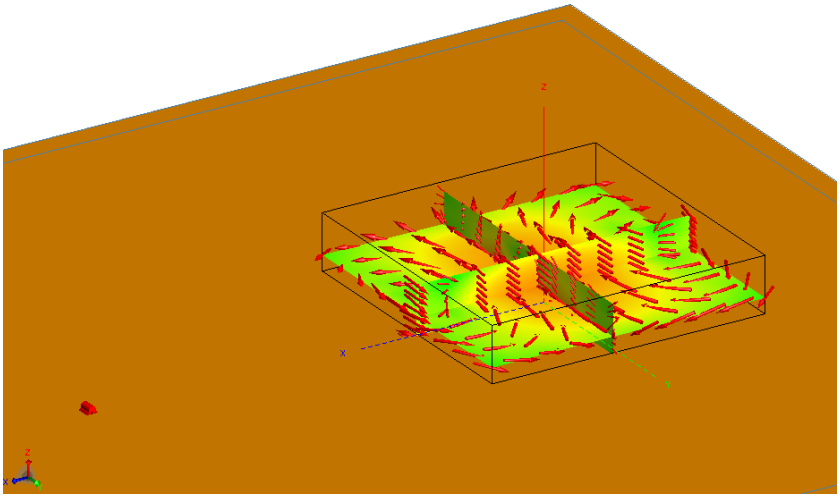

(b) Magnetic

Fig. 5.9 Total electric and magnetic fields excited by the microstrip coupled-slot at 58 GHz.

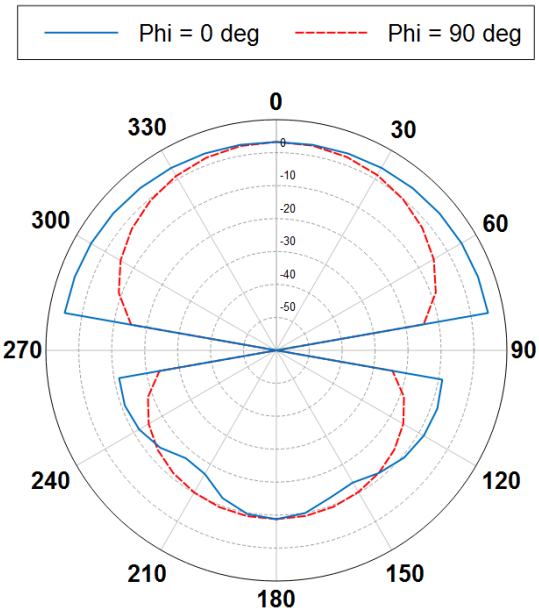

Fig. 5.10 Realized gain for xz-plane ($\phi = 0$) and y-z plane ($\phi = 90$)

Thus, the same eigenvalues can be obtained for VIE as for SIE and thus the same resonance frequencies. Exception is made for the modes corresponding to eigenvalues with negative slope. These eigenvalues corresponds to the *non-radiating* modes studied in the previous chapter and are not present in VIE. Anyway, as the slot is outside the DR the *non-radiating* modes will not be excited, and therefore they will not contribute to the electromagnetic field.

5.3 Substructures Characteristic Mode Method

A new design procedure for slot-coupled RDRA using CMs is applied here for the first time. This study allows to optimize the radiation bandwidth in the same analysis process for both the DR and the SGP. This procedure consists of two parts. First, a DR and a SGP are designed with the PMCHWT formulation and the planar Green's function, respectively. During the second part of the method a CPW will be add. This represents a difference with respect to the previous design method. The reason is that it was found that the CPW transmission

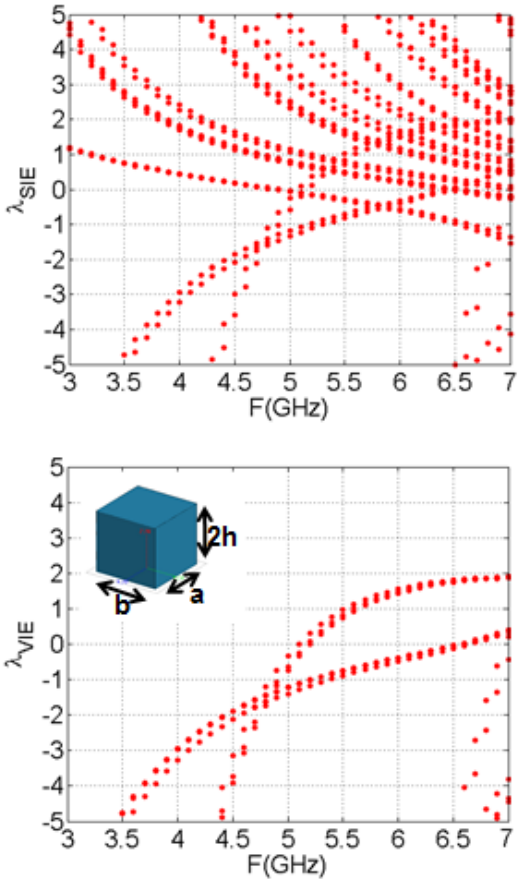

Fig. 5.11 Comparison between SIE (top) and VIE (down) characteristic eigenvalues for a RDR ($\varepsilon_r = 10.2$) with dimensions $a = b = 15$ mm and $h = 7$ mm

line could be more appropriate for the frequency band involved an the LTCC technology.

5.3.1 Rectangular DR Design Procedure

The numerical procedure to design a DR is the same as the one presented in Fig. 5.1 except when considering the impedance matrices and their post-processing. Here, instead of considering only the impedance matrix of an

isolated DR with an infinite ground plane, the slot and the dielectric substrate, called SGP, are considered as part of the impedance operator too. The main idea here is to calculate the characteristic modes of a DR in the presence of a slot and vice versa. Therefore, the total impedance matrix, Z_{Total}, has to be inspected to know which components of the matrix belong to the DR, and which others belong to the SGP set. These components are related with the basis functions used in the surface meshing employed by the MoM. Once these components are known the corresponding blocks to these two objects will be post-processed and diagonalized. Furthermore, in comparison with the previous design method, it will be seen that the resonance frequencies obtained with this design method are closer to the real ones when considering low permittivities.

Theory

Let us see Z_{Total} in Fig. 5.12. This matrix is obtained with $FEKO$ by using the MoM. On the one hand, we use the Planar Green's Functions for Multilayered Media function to define the SGP. On the other hand, we use the SIE formulation based on the PMCHWT for solving the DR. After running the simulations, the operator Z_{Total} is obtained and opened from Matlab.
In Z_{Total}, Z_d and Y_d are the impedance and admittance block matrices corresponding to the isolated dielectric, Y_s the admittance block matrix for the isolated SGP, and the C, L and K are the matrices of the corresponding mutual coupling blocks.

Due to the antisymmetries appeared in Z_{Total}, we perform the same change as Harrington proposed in [29], leaving a completely symmetric matrix. Otherwise, the characteristic eigenvalues and eigenfunctions would not be real but complex.

As discussed below, certain conditions should be met to preserve the hermiticity of our operators. The new matrix takes the following form,

$$Z'_{Total} = \left[\begin{array}{cc|c} Z_d & -jC & -jL \\ -jC^t & Y_d & K \\ \hline -jL^t & K^t & Y_s \end{array}\right] \tag{5.1}$$

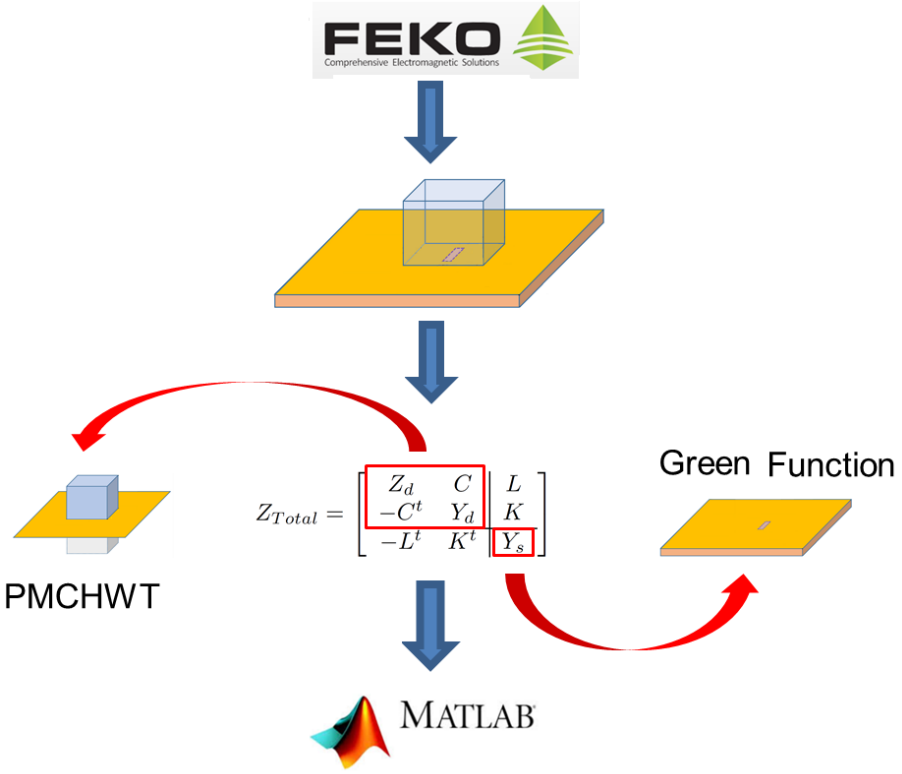

Fig. 5.12 Graphical explanation about the information contained in the MoM operator Z_{Total}.

Once the matrix is made symmetric, we rename it by blocks,

$$Z'_{Total} = \left[\begin{array}{c|c} D & M \\ \hline M^t & S \end{array}\right] \tag{5.2}$$

In equation (5.2) D is the block containing the impedance matrix of the isolated DR, S is the block containing the admittance matrix of the SGP, and M the block which contains the information about the mutual coupling between the SGP and the DR. Our goal now is to calculate the characteristic modes for the

SGP in the presence of the DR, and vice versa, through the Schur complement of our operator Z'_{Total}.

Let us consider the complete system of equations governed by MoM in which the operator (5.2) has been calculated,

$$\begin{bmatrix} D & M \\ M^t & S \end{bmatrix} \begin{bmatrix} \mathbf{f} \\ j\mathbf{M} \end{bmatrix}_{tan} = \begin{bmatrix} \mathbf{g}^{inc} \\ j\mathbf{H}^{inc} \end{bmatrix}_{tan} \tag{5.3}$$

This reduced system of equations has exactly the same form as (2.66). In (5.3) the j factor has been also included in $\mathbf{M}$ and $\mathbf{H}^{inc}$ as in the operator (5.1). This has been done to preserve the equality of the original equation system. The $\mathbf{f}$ currents and the $\mathbf{g}^{inc}$ excitation vector are defined in (2.69). On the other hand, $\mathbf{M}$ is the equivalent magnetic current for the slot, and $\mathbf{H}^{inc}$ its magnetic field excitation vector.

Now, since CMs are independent of any excitation it is possible to solve the following equation system,

$$\begin{bmatrix} D & M \\ M^t & S \end{bmatrix} \begin{bmatrix} \mathbf{f} \\ j\mathbf{M} \end{bmatrix}_{tan} = \begin{bmatrix} 0 \\ 0 \end{bmatrix}_{tan} \tag{5.4}$$

From where a homogeneous system of two equations and two unknowns can be extracted (Rename $j\mathbf{M} = \mathbf{h}$)

$$D(\mathbf{f}) + M(\mathbf{h}) = 0 \tag{5.5}$$

$$M^t(\mathbf{f}) + S(\mathbf{h}) = 0 \tag{5.6}$$

Solving for $\mathbf{f}$ in (5.5), $\mathbf{f} = -D^{-1}M(\mathbf{h})$. Substituting in (5.6), a single equation in $\mathbf{h}$ is obtained,

$$\left[S - M^t(D^{-1}M)\right]\mathbf{h} = 0 \tag{5.7}$$

If we do the same on $\mathbf{h}$, the following relation is obtained,

$$\left[D - M(S^{-1}M^t)\right]\mathbf{f} = 0 \tag{5.8}$$

Note that both **f** and **h** have been decoupled. Now **f** and **h** have new operators acting on them. The method of extraction of this operators is called extraction of the Schur complements of an operator. In addition, these two new operators are known as substructure operators in the context of characteristic mode theory because they give us the possibility to know how one structure is affected by the other and vice versa.

Once the concept is understood, it is possible to calculate the Schur complements directly from the total impedance matrix Z'_{Total}, (5.2).

The Schur complements are related to the dielectric block D and the SGP block S, as shown below.

- Schur complement of S in Z'_{Total}:

$$[D]_{sub} = D - MS^{-1}M^t \qquad \text{if } S^{-1} \text{ exist} \tag{5.9}$$

- Schur complement of D in Z'_{Total}:

$$[S]_{Sub} = S - M^t D^{-1}M \qquad \text{if } D^{-1} \text{ exist} \tag{5.10}$$

Equations (5.9) and (5.10) present the substructure operators corresponding to the DR and the SGP, respectively. These are the new operators to be diagonalized with the TCM. The importance of extracting the $[S]_{Sub}$ operator is that after diagonalizing it will provide the characteristic modes of the substructure SGP under the influence of the DR. In other words, the substructure operator play the role of a numerical specialized Green's function of the SGP that takes into account the boundary condition of a nearby DR. Therefore, we can see how the resonances are altered by having a SGP isolated, or in the presence of the dielectric resonator, just including or not the DR. Similarly, the same can be said about the DR in the presence of the SGP, block $[D]_{Sub}$.

Matrix $[D]_{Sub}$ contains the information of how the DR behaves in the presence of the SGP, while matrix $[S]_{Sub}$ contains the information of how the SGP

behaves in the presence of the DR. And that is why we can study their disturbed resonances.

As the Schur complement theory is being applied to our operators, the following conditions must be met, [22]:

- $Re(Z'_{Total})$ is positive semidefinite if and only if $Re(D)$ and $Re([D]_{Sub})$ are both positive semidefinite.

- $Re(Z'_{Total})$ is positive semidefinite if and only if $Re(D)$ and $Re([D]_{Sub})$ are both positive semidefinite.

- $Re(Z'_{Total})$ is positive semidefinite if and only if $Re(S)$ and $Re([S]_{Sub})$ are both positive semidefinite.

- If $Re(D)$ is positive semidefinite, then $Re(Z'_{Total})$ will be positive semidefinite if and only if $Re([D]_{Sub})$ is positive semidefinite.

- If $Re(S)$ is positive semidefinite, then $Re(Z'_{Total})$ will be positive semidefinite if and only if $Re([S]_{Sub})$ is positive semidefinite.

These conditions are crucial for both eigenvalues and eigenfunctions to be real. Here lies the importance of the symmetrization carried out in (5.1). With this, the power radiated by the equivalent surface currents will always be greater than or equal to zero, as they must be.

Now we can apply the generalized eigenvalue problem to the matrices $[D]_{Sub}$ and $[S]_{Sub}$, to obtain the equations that will allow us to calculate the characteristic modes.

$$Im([D]_{Sub})I_n^D = \lambda_n^D Re([D]_{Sub})I_n^D \tag{5.11}$$

$$Im([S]_{Sub})I_n^S = \lambda_n^S Re([S]_{Sub})I_n^S \tag{5.12}$$

Where λ_n are the characteristic eigenvalues and I_n the characteristic eigencurrents.

The problem at hand is more complex than the conventional TCM PEC problem. Therefore care must be taken in interpreting the physical meaning of the eigenvalues of the substructures. These are shown below

$$\lambda_n^D \to \pm\infty \quad \text{Internal resonance} \tag{5.13}$$

$$\lambda_n^D, \lambda_n^S = 0 \quad \text{External resonance} \tag{5.14}$$

$$\lambda_n^D > 0, \lambda_n^S < 0 \quad \text{Inductive behavior} \tag{5.15}$$

$$\lambda_n^D < 0, \lambda_n^S > 0 \quad \text{Capacitive behavior} \tag{5.16}$$

The definition of the eigenvalues are as in chapters 3 and 4. Concerning λ_n^D, the external and internal resonances are close to natural resonances of the DR disturbed by the SGP. And for λ_n^S, the external CMRs approach to the external NRs of the SGP perturbed by the DR. For the case of the SGP there is no internal resonance because is not a closed surface. Furthermore, it is important to note the change in sign of λ_n^S with respect to electric current eigenvalues since now characteristic currents are magnetic.

At this point, it is of interest to do some comments related to the information that can be obtained from the eigenvalues previously presented. Let us study λ_n^S, for instance, since as it will be presented later in the DRA design it plays an important role in the SCM method. As Fig. 5.13 presents, there are several antenna configurations named as A, B, C and D. These configurations consider the following:

- **A** An infinite ground plane with a slot (isolated slot)
- **B** An infinite ground plane with dielectric substrate below (thickness "h1")
- **C** An infinite ground plane with a dielectric substrate below (thickness "h1"), plus a dielectric substrate of infinite thickness from above.
- **D** An infinite ground plane with dielectric substrate below (thickness "h1"), plus a dielectric substrate of thickness "h2" above.
- **E** An infinite ground plane with dielectric substrate below ("h1" thickness), plus a DR above the "h2" height and a square base with "a" by "a".

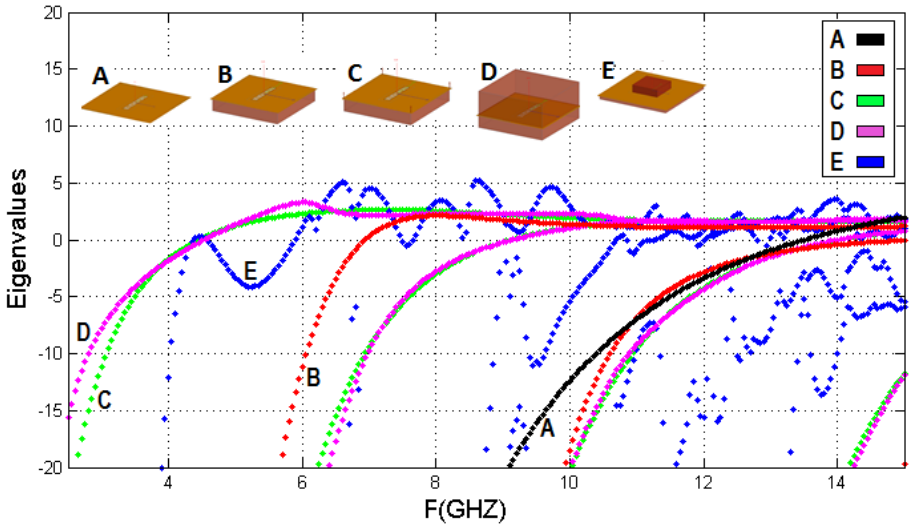

Fig. 5.13 A comparison between slot eigenvalues for different configurations with some dielectric insertions

As can be seen, several dielectric inclusions have been considered in Fig. 5.13, from the isolated slot (A) to the DRA (D). This has been realized to show the potential of this method. Resonances will be those in which $\lambda_n^S = 0$

In A, λ_n^S resonates around 14 GHz. When introduced a substrate in B, as done if microstrip or coplanar waveguides were used, the slot resonates at 6.9 GHz. If we now use an infinite dielectric medium above the slot, λ_n^S resonates at a lower frquency as expected, 4.5 GHz (C). So far there is nothing new here. But in D, λ_n^S starts to show some perturbation effect at 6 GHz when the infinite dielectric media above the slot is limited in the x and y directions. This limits are the same as the aquare base dimmensions of the DR, i.e., "a" by "a". And the resonance is about 4.4 GHz. And finally in E, the fact to reduce the dielectric that is above the slot until the high of the DR produces many perturbations in λ_n^S, and furthermore, two resonances at 4.3 GHz and 4.6 GHz due to the first two modes that can be excited in the DR. The last, is the most important effect that can be extracted from λ_n^S. Because in addition to see the resonances of the slot in the presence of the dielectric, λ_n^S gives information of how a slot increase the bandwidth when introducing a DR on it. This method is

very interesting because we can clearly see the change that occurs in the slot response when dielectrics are included or not.

Application of the Theory

In the following we apply the theory developed in the previous section, and interpret the results with the purpose of designing a DRA fed by a coplanar waveguide slot. See a sketch in Fig. 5.14.

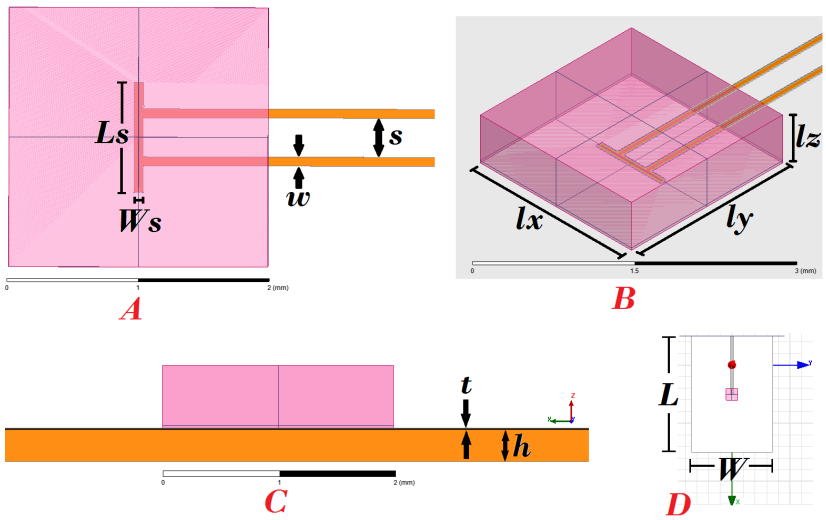

Fig. 5.14 Antenna parameters and scheme.

For the SGP and the DR design, we will use equations (5.11) and (5.12) using a characteristic mode MATLAB interface created between *MATLAB* and *FEKO*. This is the same procedure as described previously for the VIE formulation. The only difference is that two operators have to be diagonalized here. After the diagonalization, it is possible to see the eigenvalues, eigenvectors and eigenfields. The results obtained for the eigenvalues are shown in Fig. 5.15.

Fig. 5.15 shows the results for λ_n^D and λ_1^S for those parameters that maximize the radiation bandwidth for the DRA and the slot. As shown in Fig. 5.15 left, the points A and B show the resonances given by the TE_{111} mode, also known as magnetic dipole mode. Unlike the VIE method presented before, in which the TE_{111} eigenvalue shown in Fig. 5.3 exhibited two degenerated eigenvalues, TE_{111}^y and TE_{111}^x, due to the symmetry between the xz-plane and

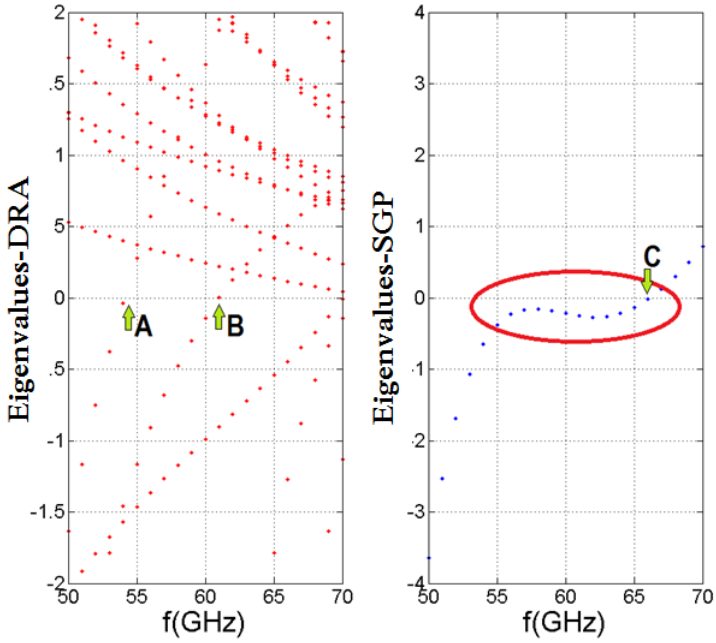

Fig. 5.15 Characteristic eigenvalues. Left: λ_n^D. Right: λ_1^S

yz-plane, here things are different. Modes passing through *A* and *B* are those of the TE_{111}^y and TE_{111}^x, respectively. However, to our surprise, the system provides us a more realistic case in terms of characteristic modes, and therefore in terms of resonances. The two modes appear now non-degenerate. The reason for the non-degeneration is because the underlying symmetry has been broken by an external perturbation, the slot in this case. This phenomenon can only be appreciated by using this method. This causes the splitting in the degenerate eigenvalues and that is why they resonate at different frequencies. This information provided by this model is very interesting when it comes to design, because unlike the model of magnetic walls, whose $f_{res} = 64$ GHz for the same parameters of the DRA, or the VIE method presented before, this model is more accurate and gives the possibility of separately viewing modes TE_{111}^y and TE_{111}^x as two distinct modes. Finally, notice the modes with negative slope. These are the non-radiating modes,which do not impair the interpretation given above.

Regarding to the SGP eigenvalues shown in Fig. 5.15 right, they are $\lambda_1^S \approx 0$ for the desired frequency range, meaning that the slot in fact radiates efficiently at these frequencies. Point *C* is the resonant frequency of the SGP, but because of the presence of the DRA the whole curve deformes with respect to the usual eigenvalue curve for slots or dipoles and approaches to zero in a wide range of frequencies. With this approach, we have found that there is a slot width for which the bandwidth of the antenna is maximized. Thus, a considerable radiation bandwidth is achieved. In addition, as we shall see later in the S11 parameter, the eigenvalue curve of the slot is centered at 60 GHz. This is due to having chosen a slot length that makes it resonate at 66 GHz (point C in Fig. 5.15), and a DR size that in which the TE^y_{111} mode resonates at 54 GHz (point A in Fig. 5.15). In this way, the resonance of the complete structure, the DRA, can be centered at 60 GHz, and this is why this method provides more realistic values than when studying isolated DRs.

Once the eigenvalues are studied, let us see the characteristic currents associated to them. Figs. 5.16 and 5.17 show the electric (right) and magnetic (left) characteristic currents for the TE^y_{111} and TE^x_{111} modes, respectively. Unlike in the previous method the fields appear to be significantly different despite they are two degenerate modes. The effect of the perturbing slot is clearly the cause. Therefore a more reliable design can be expected from this method since it provides the actual field distribution in the presence of the surrounding media.

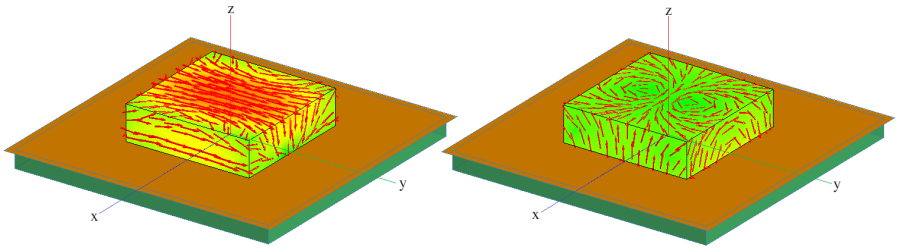

Fig. 5.16 Characteristic eigencurrents TE^y_{111}. Left: Magnetic. Right: Electric.

The optimum dimensions found for the DR and the SGP shown in Fig. 5.14 are the following: the length of the slot, $L_s = 850$ μm, the width of the slot, $W_s = 70$ μm, the width and the length of the DR, $l_x = l_y = 2$ mm, height of the DR, $l_z = 548$ μm (6-layer LTCC) and the substrate thickness, $h = 274$ μm

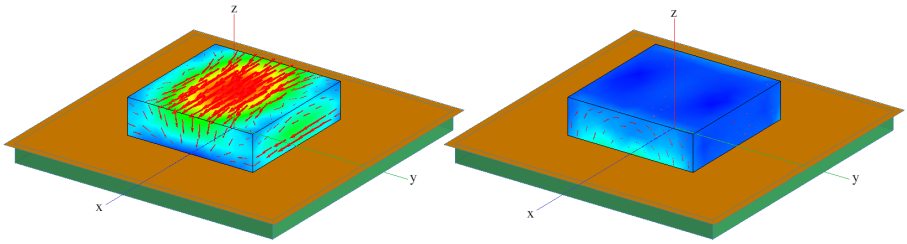

Fig. 5.17 Characteristic eigencurrents TE^{x}_{111}. Left: Magnetic. Right: Electric.

(3-layer LTCC). The material we used in this design is HL2000 from Heraeus $\varepsilon_r = 7.3$ and $\tan\delta = 0.0026$.

5.3.2 RDRA Design Procedure

Once we have the optimal parameters for the DR and the SGP designed with the TCM, we can model in *HFSS* the complete antenna. Now we will include the CPW, and we will optimize only the parameters corresponding to the CPW design. This has been realized to excite properly the TE^{y}_{111} mode of the DRA.

The model constructed in *HFSS* is shown in Fig. 5.14, where the parameters involved in the modeling are shown. In the upper left part of the figure, *A*, the top view of the DRA is displayed with the CPW. The CPW parameters after optimization are the following: the center of the coplanar waveguide, $s = 0.36$ mm, and the gap, $w = 70$ μm. Finally, the bottom right, *D*, displays the parameters of the ground plane, length and width, $L = 20$ mm y $W = 14$ mm, respectively. The CPW is adapted to 50 Ω at 60 GHz. Note that no optimization was required for the DRA after the characteristic mode design. And note also that unlike the VIE procedure, here we included a finite ground plane. Only the CPW and the ground plane were optimized in order to match the complete antenna. This method help us to reduce the optimization process and to understand the physics behind the figures that with other methods would not be possible to address.

After computation, we can check whether the electric and magnetic fields in the cavity correspond to the electrical and magnetic current characteristics presented in Fig. 4.33. The result of the electric and magnetic fields inside the DRA at 60 GHz is shown in Fig. 5.18. As we can see, the TE^{y}_{111} mode is excited as expected.

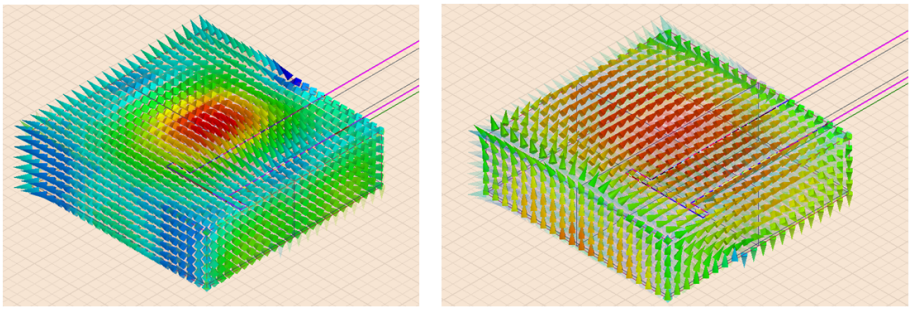

Fig. 5.18 Fields inside the cavity at 60 GHz. Left: Magnetic. Right: Electric.

The far field radiated by the TE^{y}_{111} is shown in Fig.5.19. We can see the cuts in the E-plane, perpendicular to the slot, and the H-plane in the direction of the slot. Note that both plots are normalized to their respective maximum values.

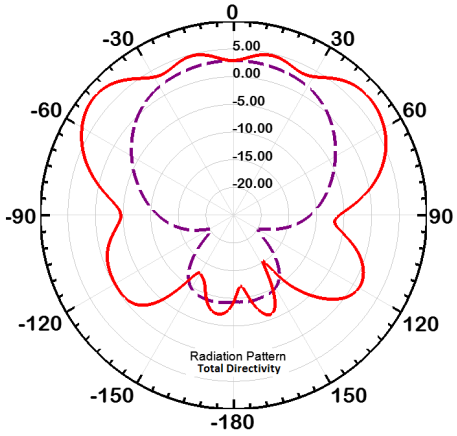

Fig. 5.19 Far field radiated by the TE^{y}_{111} at 60 GHz

Finally, Fig. 5.20 provides the results of the reflection coefficient of the antenna. As we can see, a bandwidth that remains below -10 dB from 56 GHz approximately to more than 70 GHz is achieved , i.e., more than 23 %.

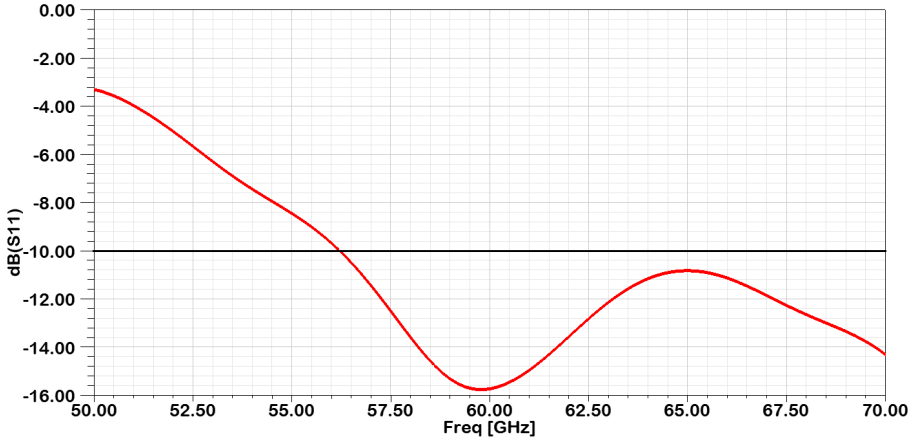

Fig. 5.20 Reflection coefficient of the RDRA.

5.4 Conclusions

We have investigated a new way to design a rectangular DR coupled to a CPW-fed slot. This new approach allows us to understand how the slot behaves in the presence of the DRA, and vice versa. It simplifies the DR-slot-ground plane design in the same procedure. Unlike other design methods, the Substructure Characteristic Mode method explains why the slot increases its bandwidth when a DR is placed on it. Furthermore, it is also concluded that even using low permittivities it is possible to design DRAs in an efficient manner. On the other hand, the intended LTCC manufacturing technology have been taken into account in the design to have the possibility to performe the feeding mechanism and DRA in the same sintering process. Due to the low permittivity of the DRA the bandwidth is 23 %, covering completely the 60 GHz ISM band. We have managed to select mode TE^{y}_{111} with the TCM, and then it was verified that it could be fed efficiently by the CPW. Finally, we have presented the radiation patterns for the E- and H-planes.

Chapter 6

Conclusions and Future Work

6.1 Conclusions

The main objective of this thesis has been to interpret solutions of the theory of characteristic modes applied on metallic and dielectric bodies, to later develop a new method to design dielectric resonator antennas. It is worth noticing that this thesis is the first to link natural modes and characteristic modes for conducting and dielectric materials, and specifically for DRA.

Since the theory of characteristic modes is being widely used for the antenna design, the task carried out in this thesis becomes relevant. Currently, DRAs are designed based on known natural modes for isolated DR without any considerations of the excitation mechanisms or the infinite ground plane. So, without a solid knowledge, optimization techniques or 'trial and error' based on full wave analysis software with proper initial design, mainly depend on designer's experience to provide a proper design for these antennas. This thesis helps in making the proper design including the excitation and nearby surrounding. Such a procedure will provide the proper design tool for antenna engineering. The studies and conclusions presented in the thesis are detailed below:

In Chapter 3, a comparison has been made between the resonances obtained by the TCM and the natural resonances. This study has been performed for both an infinite circular cylinder and a PEC sphere. The object of this study has been to demonstrate that these two sets of resonances are different. This conclusion is important because publications have been found that confuse these resonances. In addition to this study, the comparison between the two families of resonances

for an electric dipole is also presented. It is concluded that since the natural resonances are the only ones specific to the object and with physical meaning, the characteristic mode resonances are just close to them. The lower the damping factor of the natural resonances, the closer the TCM resonances will be to the natural ones. The confusion between the two has occurred because for flat antennas both families of external resonances are very close to each other, since there are no natural internal resonances. In contrast, in the case of conducting closed bodies that can give rise to cavities, while the internal resonances are equal, because the damping factor is zero, the external characteristic resonances and external natural resonances are completely different because the last have a considerable damping factor. In addition, only after introducing complex values on *ka* argument into the characteristic eigenvalues, both for the cylinder and for the sphere, external natural resonances could be obtained from the characteristic mode procedure. It is important to mention that the same conclusions have been drawn for the cylinder (2D analysis) as for the sphere (3D analysis).

Chapter 3 also presented a *geometrical* relation between complex natural resonances and characteristic mode resonances. It was concluded that the theory of characteristic modes diagonalizes the phase angle of the characteristic impedance. Indeed, that is why in the definition of the characteristic eigenvalue it is related to the storage of electric and magnetic energy, for λ_n less than zero and λ_n greater than zero, respectively.

Additionally, it is shown that in fact, for $\lambda_n = 0$, characteristic modes do not radiate maximum field nor the total current becomes maximum when they are on an external characteristic resonance mode. This fact is based on the same idea as before. For flat antennas there seems to be a maximum of electric current, and radiated field when $\lambda_n = 0$ because both resonant families, external natural and external characteristic are very close to each other. Only on the complex natural frequency the phenomenon of resonance really happens.

Finally, Chapter 3 presented a method for extracting the dispersion diagram of a circular PEC waveguide. This has been possible after analytically solving the EFIE considering oblique incidence. In this way, the dependence of k_z is in the impedance matrix Z. The idea was to look for internal characteristic resonances of Z matrix for different values of k_z. The results are exactly the same as those obtained by the conventional method.

In Chapter 4, an analysis of natural resonances and characteristic mode resonances was presented. This analysis studied the infinite dielectric circular cylinder and the dielectric sphere. With respect to the study of the infinite

dielectric circular cylinder, the PMCHWT formulation has been analytically solved. While for the study of the dielectric sphere the study has been purely numerical, also based on the PMCHWT formulation. The analytical study allowed us to draw conclusions that would be impossible by a numerical analysis. In fact, thanks to the analytical solutions it has been possible to do variations on the dielectric constant and to use complex frequencies, that could not have been possible to extract with FEKO. Regarding the cylinder analysis, it has been demonstrated that the resonances defined by the characteristic eigenvalues, internal and external, are not the same as the internal and external natural ones. It has been observed that when λ_n is either zero or infinite, the associated frequencies are close to the internal natural resonances for different modes. This means that for an eigenvalue obtained with the value of the order $n = 0$, for instance, each successive $\lambda_n = 0$ and $\lambda_n = \pm\infty$, corresponds to the pole $m = 1$ in the first case and $m = 2$ in the second, and so forth. So the conclusion is that the characteristic mode resonances give only frequency values which are close but not equal to internal natural resonances. And also that the proximity between characteristic mode resonances and internal natural resonances *depends on the relative permittivity* of the dielectric cylinder. As the permittivity decreases, the difference between both resonances becomes larger. For example, it was found that for $\varepsilon_r = 10$ the first characteristic resonance of the TM_0^z mode differed from the natural one around 40%. However, for $\varepsilon_r = 90$ this difference was about 15%. Likewise, for a given permittivity, as the mode order increases the internal natural resonances get usually closer to the real frequency axis, as a rule. Therefore, the difference between characteristic and internal natural resonances will become smaller. For example, the TE_0^z mode exhibits a difference between the two families of resonances of about 4% for $\varepsilon_r = 10$. That means the difference also depends on the mode that is being compared. This differences have to be considered when one intends to design DRAs with the theory of characteristic modes, since it could be possible to make a mistake in the design. The same conclusions have been reached for the dielectric sphere, meaning that the conclusions arrived at in this chapter could be extended to any 3D geometry.

In addition, Chapter 4 also examined the contribution to the total current and the total field of the *non-radiating* modes. Here, the analytical solution have played an important role, since there is no chance to observe these types of modes in FEKO. As already explained in Chapter 4, the *non-physical* terminology is being currently accepted to such extent that numerical procedures

have been developed and inplemented in commercial solvers for getting rid of these modes. What has been shown here is that these modes are only modes that do not radiate to the exterior of the cylinder surface but they do contribute to the field inside the dielectric cylinder when excited properly. In this case, the infinite dielectric cylinder has been fed by an infinite electric wire source located in the center of the cylinder. The result has been that when properly excited, they do contribute to the total electric and magnetic field. Therefore, the *non-physical* modes have physical meaning and it is proposed to rename them as *non-radiating* modes.

In Chapter 5, a method based on characteristic modes of substructures has been proposed. This method has been compared with a more conventional EFIE-VIE method for the design of a RDRA with very low permittivity. This has been done in order to show that the CMRs provide better results when considering also the surrounding media, not only the isolated DR. This study has been done because for low permittivities the resonances provided by the characteristic eigenvalues differ significantly from the internal natural resonances. Furthermore, unlike the VIE method, the Substructure based method offers the possibility of differentiating non-degenerate modes. When the surrounding media is included in the design the DR symmetries are broken and eigenvalues viewed as degenerated with the VIE method, can be viewed as non-degenerate with the Substructure based method. The results obtained from Substructure based method provides resonances which are closer to what they really should be. Therefore, it provides a more realistic view of what physically happens in the antenna.

Finally, with regard to the antennas that have been designed: A RDRA excited by a microstrip feeder with a rectangular coupled slot has been designed with the VIE method. The antenna has been designed with Ferro A6-M material ($\varepsilon_r = 5.9, tan_\delta = 0.001$), and for ISM-band at $60GHz$. The proposed antenna has an impedance bandwidth of 33% for $S_{11} < -10$ dB. Also, a RDRA fed by a coplanar waveguide and a slot have been designed with the Substructure method. The results obtained show that the proposed antenna radiation bandwidth determined by 10-dB return loss can be as wide as 14 GHz, more than 23% centered at about 60 GHz. The material used was HL2000 from Heraeus ($\varepsilon_r = 7.3, tan_\delta = 0.0026$). Both designs have been realized to fully exploit the fabrication characteristics of the LTCC with the minimum required number of layers, and in the same sintering process. The first antenna have been designed with 7 layers, and the second with 6 layers.

6.2 Future Work

During the realization of this thesis, new questions and research lines have emerged with interest in what relates to antenna design through the theory of characteristic modes.

First of all, it is worth mentioning the study of closed waveguides. In the thesis it was presented for the first time how to extract the dispersion diagram from the characteristic eigenvalues in an analytic way. Taking into account that the analysis with characteristic modes is being extended to other design areas, this would be a promising area of application. As future work it is proposed to extract the currents and characteristic fields inside the waveguide, and to study the advantages that would contribute against the conventional design method. Considering that this theory is built on the MoM, guides with arbitrary section could be studied.

Linked to this, a waveguide can be seen as a periodic structure on the propagation axis. It could be said that this is a one-dimensional periodic structure with a wave vector k_z, oriented in the direction of propagation z. In the same way as for the circular waveguide, in which it has been possible to extract the dispersion diagram, it will also be possible to extract it considering periodicity in k_y and/or k_z, i.e., in a 2D or 3D periodic structure. This means that it is possible to extract the band diagram of periodic structures from the theory of characteristic modes. The key is to study the way in which it is calculated from the MoM, $det(Z) = 0$, and from what is explained in this thesis find the resonances of the characteristic eigenvalues that construct the band diagram. It would also be important to relate the Floquet modes with the characteristic modes.

In addition, as studied for the PEC cylinder and the PEC sphere, it would be interesting to study to find the natural resonances for the straight wire, the dielectric cylinder and the dielectric sphere. Concerning the infinite dielectric cylinder, some different aspects were found in comparison with the PEC cylinder and the PEC sphere. Unlike the latter ones, the analytical eigenvalues after considering complex ka values were complex valued, not real numbers. And the real part of both eigenvalues, the non-radiating and the radiating modes, converged on their corresponding natural resonances. This study is not yet solved, since the PMCHWT formulation do not meet the relation presented for conducting bodies (3.20). The PMCHWT formulation is a more complicated problem and in order to understand more its eigenvalues, a relation between the

natural modes and the characteristic modes would help to understand more the behavior and interpretation of characteristic modes in dielectric materials.

On the other hand, there is a rather interesting future work in regard to the study of the dielectric sphere. Try to excite the *non-radiating* modes through a point source inside. In this thesis it has been shown that for both the eigenvalues and their resonances the sphere and the cylinder follow the same physics. It could be questioned that since one case is 2D and the other is 3D its results could be different. But after the analysis made, it has been observed that they follow the same pattern, and that regardless of the geometry, the differences appear when using different integral-differential formulations, as seen in Fig. 5.11. That is why it is thought that in the same way as for the dielectric cylinder, excited from an infinite conductor wire, for the sphere could also be the case through a point source inside. This would lead us to conclude with absolute validity that non-physical modes do have physical meaning in other 3D geometries. And therefore, in DR fed from the inside the *non-physical* modes play an important role.

Finally, it is important to note that as future work it is would be interesting to design Multiple Input Multiple Output (MIMO) DRA with the Substructure based-PMCHWT method. Since the orthogonal modes of a unique DRA can behave as different channels for sending information. And since to excite these modes different mechanisms of excitation are needed this method becomes interesting. In addition to mention the final master thesis [106] arising from the Substructure based-PMCHWT method presented here.

References

[1] Abramowitz, M., Stegun, I. A., et al. (1966). Handbook of mathematical functions. *Applied Mathematics Series*, 55:62.

[2] Al Salameh, M., Antar, Y. M., and Seguin, G. (2002). Coplanar-waveguide-fed slot-coupled rectangular dielectric resonator antenna. *IEEE Transactions on Antennas and Propagation*, 50(10):1415–1419.

[3] Al-Zoubi, A. S., Kishk, A. A., and Glisson, A. W. (2007). Analysis and design of a rectangular dielectric resonator antenna fed by dielectric image line through narrow slots. *Progress In Electromagnetics Research*, 77:379–390.

[4] Alroughani, H. (2017). An enhanced algorithm in tracking characteristic modes of dielectric objects. In *Applied Computational Electromagnetics Society Symposium-Italy (ACES), 2017 International*, pages 1–2. IEEE.

[5] Alroughani, H. (Master thesis, University of Ottawa, 2013). An appraisal of the characteristic modes of composite objects.

[6] Alroughani, H., Ethier, J., and McNamara, D. (2016a). Numerical experiments in tracking the characteristic modes of dielectric objects. In *Wireless Information Technology and Systems (ICWITS) and Applied Computational Electromagnetics (ACES), 2016 IEEE/ACES International Conference on*, pages 1–2. IEEE.

[7] Alroughani, H., Ethier, J., and McNamara, D. A. (2016b). Orthogonality properties of sub-structure characteristic modes. *Microwave and Optical Technology Letters*, 58(2):481–486.

[8] Alroughani, H., Ethier, J. L., McNamara, D., et al. (2014a). Observations on computational outcomes for the characteristic modes of dielectric objects. In *Antennas and Propagation Society International Symposium (APSURSI), 2014 IEEE*, pages 844–845. IEEE.

[9] Alroughani, H., Ethier, J. L., McNamara, D., et al. (2014b). On the classification of characteristic modes, and the extension of sub-structure modes to include penetrable material. In *Electromagnetics in Advanced Applications (ICEAA), 2014 International Conference on*, pages 159–162. IEEE.

[10] Antonino-Daviu, E., Cabedo-Fabres, M., Ferrando-Bataller, M., and Herranz-Herruzo, J. (2004a). Analysis of the coupled chassis-antenna modes in mobile handsets. In *Antennas and Propagation Society International Symposium, 2004. IEEE*, volume 3, pages 2751–2754. IEEE.

[11] Antonino-Daviu, E., Cabedo-Fabres, M., Ferrando-Bataller, M., and Valero-Nogueira, A. (2004b). Resonant modes in antenna handsets. In *Joint COST 273/284 Workshop*.

[12] Barber, P., Owen, J., and Chang, R. (1982). Resonant scattering for characterization of axisymmetric dielectric objects. *IEEE Transactions on Antennas and Propagation*, 30(2):168–172.

[13] Baum, C. E. (1975). On the eigenmode expansion method for electromagnetic scattering and antenna problems, part i: some basic relations for eigenmode expansions and their relation to the singularity expansion. *Interaction Note*, 229:13.

[14] Baum, C. E. (1976). Emerging technology for transient and broad-band analysis and synthesis of antennas and scatterers. *Proceedings of the IEEE*, 64(11):1598–1616.

[15] Baum, C. E. (2012). *The singularity expansion method in electromagnetics: a summary survey and open questions*. Lulu. com.

[16] Baum, C. E., Rothwell, E. J., Chen, K.-M., and Nyquist, D. P. (1991). The singularity expansion method and its application to target identification. *Proceedings of the IEEE*, 79(10):1481–1492.

[17] Benomar, A., Hacene, N. B., Megnafi, H., and Vaudon, P. (2011). Cylindrical dielectric resonator antenna for dual band application. In *Mediterranean Microwave Symposium (MMS), 2011 11th*, pages 42–46. IEEE.

[18] Bernabeu-Jimenez, T., Valero-Nogueira, A., Vico-Bondia, F., Antonino-Daviu, E., and Cabedo-Fabres, M. (2014). A 60-ghz ltcc rectangular dielectric resonator antenna design with characteristic modes theory. In *Antennas and Propagation Society International Symposium (APSURSI), 2014 IEEE*, pages 1928–1929. IEEE.

[19] Bernabeu-Jiménez, T., Valero-Nogueira, A., Vico-Bondia, F., and Kishk, A. A. (2015). Relation between characteristic modes and complex natural resonances. In *Antennas and Propagation & USNC/URSI National Radio Science Meeting, 2015 IEEE International Symposium on*, pages 452–453. IEEE.

[20] Bernabeu Jimenez, T., Valero Nogueira, A., Vico Bondia, F., Vila Jimenez, A., Sanchez Escuderos, D., and Gallee, F. (2015). A 60-ghz coplanar-waveguide-fed slot-coupled rectangular dra design using the theory of characteristic modes. In *Antennas and Propagation (EuCAP), 2015 9th European Conference on*. IEEE.

[21] Bernabeu-Jimenez, T., Vico-Bondia, F., Valero-Nogueira, A., Cabedo-Fabres, M., Gallee, F., and Antonino-Daviu, E. (2013). Understanding the analytical formulation of the characteristic modes. In *IEEE International Symposium on Antennas and Propagation and USNC-URSI National Radio Science Meeting, 2013*, page 526.3. IEEE.

[22] Boyd, S. and Vandenberghe, L. (2004). *Convex optimization*. Cambridge university press.

[23] Cabedo Fabres, M. (2008). *Systematic design of antennas using the theory of characteristic modes*. PhD thesis, U. Politècnica de València, Valencia.

[24] Cabedo-Fabres, M., Antonino-Daviu, E., Valero-Nogueira, A., and Bataller, M. F. (2007). The theory of characteristic modes revisited: A contribution to the design of antennas for modern applications. *Antennas and Propagation Magazine, IEEE*, 49(5):52–68.

[25] Cabedo-Fabres, M., Antonino-Daviu, E., Valero-Nogueira, A., and Ferrando-Bataller, M. (2004). Optimization of the polarization of reflectarrays using characteristic modes. In *Antennas and Propagation Society International Symposium, 2004. IEEE*, volume 1, pages 13–16. IEEE.

[26] Cabedo-Fabres, M., Valero-Nogueira, A., and Ferrando-Bataller, M. (2002). Systematic study of elliptical loop antennas using characteristic modes. In *Antennas and Propagation Society International Symposium, 2002. IEEE*, volume 1, pages 156–159. IEEE.

[27] Capek, M., Losenicky, V., Jelinek, L., and Gustafsson, M. (2017). Validating the characteristic modes solvers. *IEEE Transactions on Antennas and Propagation*.

[28] Chang, Y. and Harrington, R. (1977). A surface formulation for characteristic modes of material bodies. *Antennas and Propagation, IEEE Transactions on*, 25(6):789–795.

[29] Chang, Y. and Harrington, R. F. (1974). A surface formulation for characteristic modes of material bodies. Technical report, DTIC Document.

[30] Chen, C.-C. (1998). Electromagnetic resonances of immersed dielectric spheres. *Antennas and Propagation, IEEE Transactions on*, 46(7):1074–1083.

[31] Chen, Y. and Wang, C.-F. (2012). Synthesis of platform integrated antennas for reconfigurable radiation patterns using the theory of characteristic modes. In *Antennas, Propagation & EM Theory (ISAPE), 2012 10th International Symposium on*, pages 281–285. IEEE.

[32] Chen, Y. and Wang, C.-F. (2014a). Shipboard nvis radiation system design using the theory of characteristic modes. In *Antennas and Propagation Society International Symposium (APSURSI), 2014 IEEE*, pages 852–853. IEEE.

[33] Chen, Y. and Wang, C.-F. (2014b). Surface integral equation based characteristic mode formulation for dielectric resonators. In *Antennas and Propagation Society International Symposium (APSURSI), 2014 IEEE*, pages 846–847. IEEE.

[34] Chen, Y. and Wang, C.-F. (2015a). *Characteristic modes: Theory and applications in antenna engineering*. John Wiley & Sons.

[35] Chen, Y. and Wang, C.-F. (2015b). *Characteristic modes: Theory and applications in antenna engineering*. John Wiley & Sons.

[36] Chen, Y. and Wang, C.-F. (2015c). Hf band shipboard antenna design using characteristic modes. *IEEE Transactions on Antennas and Propagation*, 63(3):1004–1013.

[37] Cohn, S. B. (1968). Microwave bandpass filters containing high-q dielectric resonators. *IEEE Transactions on Microwave Theory and Techniques*, 16(4):218–227.

[38] Conwell, P. R., Barber, P. W., and Rushforth, C. K. (1984). Resonant spectra of dielectric spheres. *JOSA A*, 1(1):62–67.

[39] Dai, Q. I., Wu, J. W., Meng, L. L., Chew, W. C., and Sha, W. E. (2014). Multilevel fast multipole algorithm for characteristic mode analysis. *arXiv preprint arXiv:1412.1756*.

[40] Daviu, E. A. (2008). *Analysis and design of antennas for wireless communications using modal methods*. PhD thesis, Universitat Politècnica de València, Valencia.

[41] Dettmann, C., Morozov, G., Sieber, M., and Waalkens, H. (2009). Systematization of all resonance modes in circular dielectric cavities. In *2009 11th International Conference on Transparent Optical Networks*, pages 1–4. IEEE.

[42] Elghannai, E. A., Raines, B. D., and Rojas, R. G. (2015). Multiport reactive loading matching technique for wide band antenna applications using the theory of characteristic modes. *IEEE Transactions on Antennas and Propagation*, 63(1):261–268.

[43] Ethier, J. and McNamara, D. (2012). Sub-structure characteristic mode concept for antenna shape synthesis. *Electronics letters*, 48(9):471–472.

[44] Famdie, C. T., Schroeder, W. L., and Solbach, K. (2006). Numerical analysis of characteristic modes on the chassis of mobile phones. In *Antennas and Propagation, 2006. EuCAP 2006. First European Conference on*, pages 1–6. IEEE.

[45] FEKO, E. (2015). Simulation software.

[46] Gallée, F., Bernabeu-Jimenez, T., Cabedo-Fabres, M., Antonino-Daviu, E., Valero-Nogueira, A., and Person, C. (2013a). Conception d'une antenne de type dra à 60ghz avec la théorie des modes caractéristiques. *JNM 2013: 18èmes Journées Nationales Microondes*.

[47] Gallée, F., Bernabeu-Jiménez, T., Cabedo-Fabres, M., Antonino-Daviu, E., and Valero-Nogueira, A. (2013b). Application of the theory of characteristic modes to the design of compact metallic strip antenna with multilayer technology (ltcc). In *Antennas and Propagation (EuCAP), 2013 7th European Conference on*, pages 1891–1895. IEEE.

[48] Garbacz, R. (1965). Modal expansions for resonance scattering phenomena. *Proceedings of the IEEE*, 53(8):856–864.

[49] Garbacz, R. J. (1968). *A Generalized Expansion for Radiated and Scatered Fields*. PhD thesis, The Ohio State University, Columbus.

[50] Glisson, A. W., Kajfez, D., and James, J. (1983). Evaluation of modes in dielectric resonators using a surface integral equation formulation. *IEEE transactions on microwave theory and techniques*, 31(12):1023–1029.

[51] Golonka, L. (2006). Technology and applications of low temperature cofired ceramic (ltcc) based sensors and microsystems. *Bull Polish Acad Sci Tech Sci*, 54(2).

[52] Guo, Y.-X. and Chu, H. (2013). 60-ghz ltcc dielectric resonator antenna array. In *Antennas and Propagation Society International Symposium (APSURSI), 2013 IEEE*, pages 1874–1875. IEEE.

[53] Harrington, R. and Mautz, J. (1971a). Computation of characteristic modes for conducting bodies. *Antennas and Propagation, IEEE Transactions on*, 19(5):629–639.

[54] Harrington, R. and Mautz, J. (1971b). Theory of characteristic modes for conducting bodies. *Antennas and Propagation, IEEE Transactions on*, 19(5):622–628.

[55] Harrington, R., Mautz, J., and Chang, Y. (1972). Characteristic modes for dielectric and magnetic bodies. *Antennas and Propagation, IEEE Transactions on*, 20(2):194–198.

[56] Harrington, R. F. and Harrington, J. L. (1996). *Field computation by moment methods*. Oxford University Press.

[57] Harrington, R. F. and Mautz, J. R. (1970). Theory and computation of characteristic modes for conducting bodies. Technical report, DTIC Document.

[58] Harrison, W. H. (1968). A miniature high-q bandpass filter employing dielectric resonators. *IEEE Transactions on Microwave Theory and Techniques*, 16(4):210–218.

[59] Hu, F.-G. and Wang, C.-F. (2016). Integral equation formulations for characteristic modes of dielectric and magnetic bodies. *IEEE Transactions on Antennas and Propagation*, 64(11):4770–4776.

[60] Jin, J.-M. (2015). *The finite element method in electromagnetics*. John Wiley & Sons.

[61] Junker, G. P., Kishk, A. A., and Glisson, A. W. (1994). Input impedance of dielectric resonator antennas excited by a coaxial probe. *IEEE Transactions on Antennas and Propagation*, 42(7):960–966.

[62] Kajfez, D., Glisson, A. W., and James, J. (1984). Computed modal field distributions for isolated dielectric resonators. *IEEE transactions on Microwave Theory and Techniques*, 32(12):1609–1616.

[63] Kishk, A. A. (2001). A triangular dielectric resonator antenna excited by a coaxial probe. *Microwave and Optical Technology Letters*, 30(5):340–341.

[64] Kishk, A. A. (2005). Experimental study of broadband embedded dielectric resonator antennas excited by a narrow slot. *IEEE Antennas and Wireless Propagation Letters*, 4(1):79–81.

[65] Kishk, A. A., Auda, H. A., and Ahn, B. C. (1989). Radiation characteristics of cylindrical dielectric resonator antennas with new applications. *IEEE Antennas and Propagation Society Newsletter*, 31(1):6–16.

[66] Kishk, A. A., Glisson, A., and Kajfez, D. (1993). Computed resonant frequency and far fields of isolated dielectric discs. In *Antennas and Propagation Society International Symposium, 1993. AP-S. Digest*, pages 408–411. IEEE.

[67] Kotlyar, V., Kovalev, A., and Kozlov, D. (2016). Calculating the resonance radius of a dielectric cylinder under illumination by a plane te-wave. *Optik-International Journal for Light and Electron Optics*, 127(8):3803–3808.

[68] Kulkarni, S. and Makarov, S. (2005). Accuracy of mom vie eigenmode solution obtained with edge basis functions. In *2005 IEEE Antennas and Propagation Society International Symposium*.

[69] Kunz, K. S. and Luebbers, R. J. (1993). *The finite difference time domain method for electromagnetics*. CRC press.

[70] Larison, P. D. (1989). Evaluation of system identification algorithms for aspect-independent radar target classification. Technical report, DTIC Document.

[71] Lee, W., Sarkar, T. K., Moon, H., Lamperez, A. G., and Salazar-Palma, M. (2013). Effect of material parameters on the resonant frequencies of a dielectric object. *IEEE Antennas and Wireless Propagation Letters*, 12:1311–1314.

[72] Lee, W., Sarkar, T. K., Moon, H., and Salazar-Palma, M. (2012). Computation of the natural poles of an object in the frequency domain using the cauchy method. *IEEE Antennas and Wireless Propagation Letters*, 11:1137–1140.

[73] Li, H., Miers, Z. T., and Lau, B. K. (2014). Design of orthogonal mimo handset antennas based on characteristic mode manipulation at frequency bands below 1 ghz. *IEEE Transactions on Antennas and Propagation*, 62(5):2756–2766.

[74] Maci, S., Sipus, Z., Freni, A., Mazzinghi, A., and Skokic, S. (2014). *Advanced mathematics for antenna analysis*. Lecture notes of the European School of Antennas course book.

[75] Manteuffel, D. (2015). Characteristic mode based antenna design—a straight forward approach to small form factor antenna integration. In *Antennas and Propagation (EuCAP), 2015 9th European Conference on*, pages 1–5. IEEE.

[76] McAllister, M., Long, S. A., and Conway, G. (1983). Rectangular dielectric resonator antenna. *Electronics Letters*, 19(6):218–219.

[77] Mie, G. (1908). Beiträge zur optik trüber medien, speziell kolloidaler metallösungen. *Annalen der physik*, 330(3):377–445.

[78] Miers, Z. and Lau, B. K. (2016a). Antenna design using characteristic modes for arbitrary materials. In *Antennas and Propagation (APSURSI), 2016 IEEE International Symposium on*, pages 9–10. IEEE.

[79] Miers, Z. and Lau, B. K. (2016b). Post-processing removal of non-real characteristic modes via basis function perturbation. In *Antennas and Propagation (APSURSI), 2016 IEEE International Symposium on*, pages 419–420. IEEE.

[80] Miers, Z. T. and Lau, B. K. (2016c). Computational analysis and verifications of characteristic modes in real materials. *IEEE Transactions on Antennas and Propagation*, 64(7):2595–2607.

[81] Miers, Z. T. and Lau, B. K. (2016d). Effects of dielectrics and internal resonances on modal analysis of terminal chassis. In *Antennas and Propagation (EuCAP), 2016 10th European Conference on*, pages 1–5. IEEE.

[82] Moffatt, D. et al. (1976). Natural resonances of radar targets via prony's method and target discrimination. *IEEE Transactions on Aerospace and Electronic Systems*, (5):583–589.

[83] Mohamed-Hicho, N. M., Antonino-Daviu, E., Cabedo-Fabrés, M., Ciafardini, J. P., Bava, J. A., and Ferrando-Bataller, M. (2017). Characteristic modes of slotted planar antennas. In *Antennas and Propagation (EUCAP), 2017 11th European Conference on*, pages 2668–2672. IEEE.

[84] Mohamed-Hicho, N. M., Antonino-Daviu, E., Cabedo-Fabrés, M., and Ferrando-Bataller, M. (2016). Characteristic modes in slot antennas etched in a finite ground plane. In *Antennas and Propagation (APSURSI), 2016 IEEE International Symposium on*, pages 7–8. IEEE.

[85] Mongia, R. K. and Ittipiboon, A. (1997). Theoretical and experimental investigations on rectangular dielectric resonator antennas. *IEEE Transactions on Antennas and Propagation*, 45(9):1348–1356.

[86] Moser, P. J., Überall, H., and Morgan, M. A. (1989). Finite element computation of complex resonant frequencies for penetrable axisymmetric bodies. *Journal of electromagnetic waves and applications*, 3(2):129–142.

[87] Murray, K. and Austin, B. (1994). Synthesis of vehicular antenna nvis radiation patterns using the method of characteristic modes. *IEE Proceedings-Microwaves, Antennas and Propagation*, 141(3):151–154.

[88] Obeidat, K. A. (2010). *Design methodology for wideband electrically small antennas (ESA) based on the theory of characteristic modes (CM)*. PhD thesis, The Ohio State University.

[89] Owen, J., Barber, P., Messinger, B., and Chang, R. (1981). Determination of optical-fiber diameter from resonances in the elastic scattering spectrum. *Optics letters*, 6(6):272–274.

[90] Peterson, A. F., Ray, S. L., Mittra, R., of Electrical, I., and Engineers, E. (1998). *Computational methods for electromagnetics*, volume 2. IEEE press New York.

[91] Poggio, A. J. and Miller, E. K. (1973). *Integral equation Solution of Three-dimensional Scattering Problems, Computer techniques in electromagnetics, R. Mittra*. Pergamon Press, Oxford, pp. 159-261.

[92] Pozar, D. M. (2009). *Microwave engineering*. John Wiley & Sons.

[93] Rabah, M. H. (2015). *Design methodology of antennas based on metamaterials and the theory of characteristic modes: application to cognitive radio*. PhD thesis, Lille 1.

[94] Raines, B. D. (2011). *Systematic design of multiple antenna systems using characteristic modes*. PhD thesis, The Ohio State University.

[95] Rashidian, A. and Klymyshyn, D. M. (2008). Strip-fed excitation of very low permittivity dielectric resonator antennas. In *Microwave Conference, 2008. APMC 2008. Asia-Pacific*, pages 1–4. IEEE.

[96] Rashidian, A. and Klymyshyn, D. M. (2009). Very low permittivity slot-fed dielectric resonator antennas with improved bandwidth for millimetre-wave applications. In *Antennas and Propagation, 2009. EuCAP 2009. 3rd European Conference on*, pages 3554–3557. IEEE.

[97] Rayleigh, L. (1918). Xli. the dispersal of light by a dielectric cylinder. *The London, Edinburgh, and Dublin Philosophical Magazine and Journal of Science*, 36(215):365–376.

[98] Rezaiesarlak, R. and Manteghi, M. (2014). On the application of characteristic modes for the design of chipless rfid tags. In *Antennas and Propagation Society International Symposium (APSURSI), 2014 IEEE*, pages 1304–1305. IEEE.

[99] Rezaiesarlak, R. and Manteghi, M. (2015). Design of chipless rfid tags based on characteristic mode theory (cmt). *IEEE Transactions on Antennas and Propagation*, 63(2):711–718.

[100] Richtmyer, R. (1939). Dielectric resonators. *Journal of Applied Physics*, 10(6):391–398.

[101] Rojas, R., Elfrgani, A., and Elghannai, E. (2013). Distributed impedance matching with foster and non-foster elements. In *Antennas and Propagation (EuCAP), 2013 7th European Conference on*, pages 3015–3018. IEEE.

[102] Sarkar, T. K., Mokole, E. L., and Salazar-Palma, M. (2016). An expose on internal resonance, external resonance, and characteristic modes. *IEEE Transactions on Antennas and Propagation*, 64(11):4695–4702.

[103] Sarkar, T. K. and Pereira, O. (1995). Using the matrix pencil method to estimate the parameters of a sum of complex exponentials. *IEEE Antennas and Propagation Magazine*, 37(1):48–55.

[104] Shih, T.-Y. and Behdad, N. (2016). Bandwidth enhancement of platform-mounted hf antennas using the characteristic mode theory. *IEEE Transactions on Antennas and Propagation*, 64(7):2648–2659.

[105] Shu, S., Goggans, P., and Kiskh, A. (1993). Computation of cutoff wavenumbers for partially filled waveguide of arbitrary cross section using surface integral formulations and the method of moments. *IEEE transactions on microwave theory and techniques*, 41(6):1111–1118.

[106] Staver, V. (Master thesis, Universitat Politècnica de València,2016). Design of a mimo dielectric resonator antenna with characteristic modes theory for lte base stations.

[107] Surittikul, N. (2006). *Pattern reconfigurable printed antennas and time domain method of characteristic modes for antenna analysis and design*. PhD thesis, The Ohio State University.

[108] Surittikul, N. and Rojas, R. (2004). Analysis of reconfigurable printed antenna using characteristic modes: Fdtd approach. In *Antennas and Propagation Society International Symposium, 2004. IEEE*, volume 2, pages 1808–1811. IEEE.

[109] Swaminathan, M., Arvas, E., Sarkar, T. K., and Djordjevic, A. R. (1990). Computation of cutoff wavenumbers of te and tm modes in waveguides of arbitrary cross sections using a surface integral formulation. *IEEE transactions on microwave theory and techniques*, 38(2):154–159.

[110] Swaminathan, M., Sarkar, T., and Adams, A. T. (1992). Computation of tm and te modes in waveguides based on a surface integral formulation. *IEEE transactions on microwave theory and techniques*, 40(2):285–297.

[111] Tesche, F. and Giri, D. (2011). On the natural oscillation frequencies of a straight wire. *Interaction Notes, Note*, 621.

[112] Van Bladel, J. (1977). Resonant scattering by dielectric cylinders. *Microwaves, Optics and Acoustics, IEE Journal on*, 1(2):41–50.

[113] Vico, F., Greengard, L., and Gimbutas, Z. (2014). Boundary integral equation analysis on the sphere. *Numerische Mathematik*, 128(3):463–487.

[114] Warnick, K. F. (2008). *Numerical analysis for electromagnetic integral equations*. Artech House.

[115] Yang, B. and Adams, J. J. (2017). Quality factor calculations for the characteristic modes of dielectric resonator antennas. In *Radio Science Meeting (USNC-URSI NRSM), 2017 United States National Committee of URSI National*, pages 1–2. IEEE.

Appendix A

Analytical Solutions

The two analytical solutions presented in this appendix have contributed to the main theoretical concepts presented in this thesis. These analytical solutions have helped to obtain solutions that with a conventional EM software will be impossible, or very difficult due to the time-consuming computation. The novelty to present these analytical solutions can help to explore even more numerical solutions in CMA or the MoM. Furthermore, these analytical solutions can be used to find a precise quantity of interest over a whole range of parameters. With this a better physical insight can be easily gained.

A.1 The Infinite PEC Circular Cylinder Considering Oblique Incidence

In this section an infinite PEC circular cylinder is analytically solved considering oblique incidence in the EFIE formulation. This solution will help to find the dispersion diagram of the propagating modes in a metallic circular waveguide through the characteristic modes eigenvalues. This analytical solution is introduced here for the first time.

Let us consider an incident electric field $\mathbf{E}^i = \widetilde{\mathbf{E}}^i e^{-jk_z}$, with e^{-jk_z} dependence. The EFIE presented in Chapter 2 can be obtained by considering the following boundary conditions, the tangent total electric field is zero on the surface of the PEC body:

$$\mathbf{n} \times \left(\mathbf{E}^i + \mathbf{E}^s\right) = 0 \tag{A.1}$$

$$\left(\mathbf{E}^i + \mathbf{E}^s\right)|_{tan} = 0 \tag{A.2}$$

$$\mathbf{E}^i|_{tan} = -\mathbf{E}^s|_{tan} \tag{A.3}$$

Next, subscript tan is dropped for simplicity, and $\mathbf{E}^s = -j\omega\mathbf{A} - \nabla\phi$. To analytically solve the EFIE (A.3) considering oblique incidence, the electric current (A.4) has to be used.

$$\mathbf{J}(\mathbf{r}') = J_{z'}\mathbf{u}'_z + J_{\phi'}\mathbf{u}_{\phi'} = \sum_{n=-\infty}^{\infty}\left(\alpha_n e^{jn\phi'}\mathbf{u}'_z + \beta_n e^{jn\phi'}\mathbf{u}_{\phi'}\right)e^{-jk_z z'} \tag{A.4}$$

Moreover, both $\mathbf{A}$ and ϕ have to include the term $e^{jk_z z}$ in the cylindrical harmonic expansion of the Green function. Solving first for the magnetic vector potential $\mathbf{A}$, we have:

$$\mathbf{A} = \mu \iint_S \mathbf{J}(\mathbf{r}')G(\mathbf{r},\mathbf{r}')dS' =$$

$$\mu a \int_0^{2\pi} \sum_{n=-\infty}^{\infty} \alpha_n e^{jn\phi'} e^{-jk_z z'}\mathbf{u}'_z \frac{1}{4j} \sum_{m=-\infty}^{\infty} J_m\left(k_t r'\right) H_m^{(2)}\left(k_t r\right) e^{jm\phi} e^{-jm\phi'} e^{jk_z z} d\phi' +$$

$$\mu a \int_0^{2\pi} \sum_{n=-\infty}^{\infty} \beta_n e^{jn\phi'} e^{-jk_z z'}\mathbf{u}'_\phi \frac{1}{4j} \sum_{m=-\infty}^{\infty} J_m\left(k_t r'\right) H_m^{(2)}\left(k_t r\right) e^{jm\phi} e^{-jm\phi'} e^{jk_z z} d\phi' = \tag{A.5}$$

Now, to integrate, the primed unitary vectors have to be substituted as a function of the non-primed unitary vectors. That is $\mathbf{u}'_z = \mathbf{u}_z$ and $\mathbf{u}'_\phi = sin(\phi - \phi')\mathbf{u}_r + cos(\phi - \phi')\mathbf{u}_\phi$. To simplify the calculus in (A.5) the above unitary vector $\mathbf{u}_r$ is not considered because the solution only consider the tangential components. Moreover, it is important to use that $cos(\phi - \phi') = \frac{1}{2}\left(e^{j(\phi-\phi')} + e^{-j(\phi-\phi')}\right)$. Thus, substituting formulas and rearranging equation (A.5), it is obtained the following equation,

$$
\begin{aligned}
&\mathbf{A} = \\
&\frac{\mu a}{4j} e^{-jk_z z'} e^{jk_z z} \mathbf{u}_z \sum_{n=-\infty}^{\infty} \alpha_n \sum_{m=-\infty}^{\infty} J_m\left(k_t r'\right) H_m^{(2)}\left(k_t r\right) e^{jm\phi} \int_0^{2\pi} e^{jn\phi'} e^{-jm\phi'} d\phi' + \\
&\frac{\mu a}{4j} e^{-jk_z z'} e^{jk_z z} \mathbf{u}_\phi \sum_{n=-\infty}^{\infty} \beta_n \sum_{m=-\infty}^{\infty} J_m\left(k_t r'\right) H_m^{(2)}\left(k_t r\right) \cdot \\
&\frac{1}{2}\left[e^{j(m+1)\phi} \int_0^{2\pi} e^{jn\phi'} e^{-j(m+1)\phi'} d\phi' + e^{j(m-1)\phi} \int_0^{2\pi} e^{jn\phi'} e^{-j(m-1)\phi'} d\phi' \right] = \\
&\frac{2\pi\mu a}{4j} e^{-jk_z z'} e^{jk_z z} \sum_{m=-\infty}^{\infty} \Bigg(\alpha_m J_m\left(k_t r'\right) H_m^{(2)}\left(k_t r\right) e^{jm\phi} \mathbf{u}_z + \\
&\qquad\qquad J_m\left(k_t r'\right) H_m^{(2)}\left(k_t r\right) \frac{1}{2}\left(\beta_{m+1} e^{j(m+1)\phi} + \beta_{m-1} e^{j(m-1)\phi} \right) \mathbf{u}_\phi \Bigg)
\end{aligned}
\tag{A.6}
$$

Where the Kronecker Delta function definition (A.7) has been used to solve the above integrals.

$$
\int_0^{2\pi} e^{j(m\mp 1)\phi} e^{-jn\phi} d\phi = 2\pi \delta_{m\mp 1, n} \tag{A.7}
$$

Let us solve for the gradient of the electric scalar potential $\nabla\phi$:

$$
\begin{aligned}
\nabla\phi = \frac{1}{\varepsilon} \nabla \iint_S \frac{1}{-j\omega} \nabla' \mathbf{J}(\mathbf{r}') G(\mathbf{r}, \mathbf{r}') dS' = \\
\frac{a}{-j\omega\varepsilon} \nabla \int_0^{2\pi} \nabla' \left[\sum_{n=-\infty}^{\infty} \alpha_n e^{jn\phi'} e^{-jk_z z'} \mathbf{u}_z' + \beta_n e^{jn\phi'} e^{-jk_z z'} \mathbf{u}_\phi' \right] \cdot \\
\frac{1}{4j} \sum_{m=-\infty}^{\infty} J_m\left(k_t r'\right) H_m^{(2)}\left(k_t r\right) e^{jm\phi} e^{-jm\phi'} e^{jk_z z} d\phi' =
\end{aligned}
\tag{A.8}
$$

$$= \frac{a}{-j\omega\varepsilon}\nabla\int_0^{2\pi}\sum_{n=-\infty}^{\infty}\left(\alpha_n e^{jn\phi'}(-jk_z)e^{-jk_z z'} + \beta_n\frac{jn}{r'}e^{jn\phi'}e^{-jk_z z'}\right)\cdot$$

$$\frac{1}{4j}\sum_{m=-\infty}^{\infty}J_m\left(k_t r'\right)H_m^{(2)}\left(k_t r\right)e^{jm\phi}e^{-jm\phi'}e^{jk_z z}d\phi' =$$

$$\frac{a}{-j\omega\varepsilon}\nabla\left[\sum_{n=-\infty}^{\infty}\left(\alpha_n(-jk_z)e^{-jk_z z'} + \beta_n\frac{jn}{r'}e^{-jk_z z'}\right)\cdot\right.$$

$$\left.\frac{1}{4j}\sum_{m=-\infty}^{\infty}J_m\left(k_t r'\right)H_m^{(2)}\left(k_t r\right)e^{jm\phi}e^{jk_z z}\int_0^{2\pi}e^{jn\phi'}e^{-jm\phi'}d\phi'\right] =$$

$$\frac{2\pi a}{-j\omega\varepsilon}(-jk_z)\frac{1}{4j}\nabla\left[\sum_{m=-\infty}^{\infty}\alpha_m e^{-jk_z z'}J_m\left(k_t r'\right)H_m^{(2)}\left(k_t r\right)e^{jm\phi}e^{jk_z z}\right] +$$

$$\frac{2\pi a}{-j\omega\varepsilon}\frac{1}{4j}\nabla\left[\sum_{m=-\infty}^{\infty}\beta_m\frac{jm}{r'}e^{-jk_z z'}J_m\left(k_t r'\right)H_m^{(2)}\left(k_t r\right)e^{jm\phi}e^{jk_z z}\right] =$$

$$\frac{2\pi a}{-j\omega\varepsilon}(-jk_z)\frac{1}{4j}\sum_{m=-\infty}^{\infty}\alpha_m J_m\left(k_t r'\right)H_m^{(2)}\left(k_t r\right)e^{-jk_z z'}e^{jk_z z}e^{jm\phi}\left(jk_z\mathbf{u}_z + \frac{jm}{r}\mathbf{u}_\phi\right) +$$

$$\frac{2\pi a}{-j\omega\varepsilon}\frac{1}{4j}\sum_{m=-\infty}^{\infty}\beta_m\frac{jm}{r'}J_m\left(k_t r'\right)H_m^{(2)}\left(k_t r\right)e^{-jk_z z'}e^{jk_z z}e^{jm\phi}\left(jk_z\mathbf{u}_z + \frac{jm}{r}\mathbf{u}_\phi\right) \tag{A.9}$$

Once $\mathbf{A}$ and $\nabla\phi$ are calculated, the impedance matrix operator components can be obtained through the inner product of these two operators with $e^{-jn\phi}$. Then, separately we have,

$$\left\langle e^{-jn\phi}, \mathbf{A} \right\rangle =$$

$$\frac{2\pi\mu a}{4j} e^{-jk_z z'} e^{jk_z z} \sum_{m=-\infty}^{\infty} \alpha_m J_m\left(k_t r'\right) H_m^{(2)}\left(k_t r\right) \mathbf{u}_z \int_0^{2\pi} e^{-jn\phi} e^{jm\phi} d\phi$$

$$+ \frac{2\pi\mu a}{4j} e^{-jk_z z'} e^{jk_z z} \sum_{m=-\infty}^{\infty} J_m\left(k_t r'\right) H_m^{(2)}\left(k_t r\right) \frac{1}{2} \mathbf{u}_\phi \left(\beta_{m+1} \int_0^{2\pi} e^{-jn\phi} e^{j(m+1)\phi} d\phi \right.$$

$$\left. + \beta_{m-1} \int_0^{2\pi} e^{-jn\phi} e^{j(m-1)\phi} d\phi \right) = \frac{(2\pi)^2 \mu a}{4j} e^{-jk_z z'} e^{jk_z z} J_n\left(k_t r'\right) H_n^{(2)}\left(k_t r\right) \alpha_n \mathbf{u}_z$$

$$+ \frac{(2\pi)^2 \mu a}{4j} e^{-jk_z z'} e^{jk_z z} \left[J_{m-1}\left(k_t r'\right) H_{n-1}^{(2)}\left(k_t r\right) + J_{m+1}\left(k_t r'\right) H_{n+1}^{(2)}\left(k_t r\right) \right] \frac{1}{2} \beta_n \mathbf{u}_\phi \tag{A.10}$$

$$\left\langle e^{-jn\phi}, \nabla\phi \right\rangle = \frac{2\pi a}{4\omega\varepsilon} \cdot$$

$$\left[k_z \sum_{m=-\infty}^{\infty} \alpha_m J_m\left(k_t r'\right) H_m^{(2)}\left(k_t r\right) e^{-jk_z z'} e^{jk_z z} \left(k_z \mathbf{u}_z + \frac{m}{r} \mathbf{u}_\phi \right) \int_0^{2\pi} e^{-jn\phi} e^{jm\phi} d\phi - \right.$$

$$\left. \sum_{m=-\infty}^{\infty} \beta_m \frac{m}{r'} J_m\left(k_t r'\right) H_m^{(2)}\left(k_t r\right) e^{-jk_z z'} e^{jk_z z} \left(k_z \mathbf{u}_z + \frac{m}{r} \mathbf{u}_\phi \right) \int_0^{2\pi} e^{-jn\phi} e^{jm\phi} d\phi \right] =$$

$$\frac{(2\pi)^2 a k_z}{4\omega\varepsilon} J_n\left(k_t r'\right) H_n^{(2)}\left(k_t r\right) e^{-jk_z z'} e^{jk_z z} \alpha_n \left(k_z \mathbf{u}_z + \frac{n}{r} \mathbf{u}_\phi \right) -$$

$$\frac{(2\pi)^2 a}{4\omega\varepsilon} \frac{n}{r'} J_n\left(k_t r'\right) H_n^{(2)}\left(k_t r\right) e^{-jk_z z'} e^{jk_z z} \beta_n \left(k_z \mathbf{u}_z + \frac{n}{r} \mathbf{u}_\phi \right) \tag{A.11}$$

Considering now equations (A.10) and (A.11) and reordering them, the following impedance matrix operator can be obtained:

$$Z = \frac{(2\pi)^2 a}{4\omega\varepsilon_0}.$$

$$\begin{bmatrix} k_t^2 J_n(k_t a) H_n^{(2)}(k_t a) & \frac{n}{a} k_z J_n(k_t a) H_n^{(2)}(k_t a) \\ \frac{n}{a} k_z J_n(k_t a) H_n^{(2)}(k_t a) & \frac{nk_z}{ak_t} J_n(k_t a) \frac{nk_z}{ak_t} H_n^{(2)}(k_t a) - k_0^2 J_n'(k_t a) H_n'^{(2)}(k_t a) \end{bmatrix} \tag{A.12}$$

This operator can be particularized for other cases of interest in this thesis. That is $k_z = 0$, what means the electromagnetic plane wave has normal incidence on the cylinder surface, i.e., we obtain the transverse electric and magnetic impedance operators for normal incidence. It can also been conclude that characteristic eigenvalues depend on the excitation incident angle, i.e., k_z.

$$Z^{EFIE,\ TM_n^z} = \frac{\eta\pi ka}{2} J_n(ka) H_n^{(2)}(ka) \tag{A.13}$$

$$Z^{EFIE,\ TE_n^z} = \frac{\eta\pi ka}{2} J_n'(ka) H_n'^{(2)}(ka) \tag{A.14}$$

These two operators coincide with the operators found in [114] and [90].

A.2 The Infinite Dielectric and/or Magnetic Circular Cylinder

In this section, the analytical solution for an infinite dielectric and/or magnetic circular cylinder is presented considering normal incidence. This solution is presented here for the first time, since no solutions in bibliography have been found considering the PMCHWT integro-differential equation.

Let us consider the PMCHWT-SIE formulation presented in section 2.4. The boundary conditions for the electric and magnetic fields are $\hat{n} \times \mathbf{E}_1 = \hat{n} \times \mathbf{E}_2$ and $\hat{n} \times \mathbf{H}_1 = \hat{n} \times \mathbf{H}_2$, respectively. Being the subscript 2 for the inner media, and subscript 1 for the surrounding media. Where the fields can be expressed as a function of their corresponding potentials and the incidents electric and magnetic fields,

$$\mathbf{E}_1 = -j\omega\mathbf{A}^{(1)} - \nabla\phi_e^{(1)} - \frac{1}{\varepsilon_1}\nabla\times\mathbf{F}^{(1)} + \mathbf{E}^{inc} \tag{A.15}$$

$$\mathbf{H}_1 = \frac{1}{\mu_1}\nabla\times\mathbf{A}^{(1)} - j\omega\mathbf{F}^{(1)} - \nabla\phi_m^{(1)} + \mathbf{H}^{inc} \tag{A.16}$$

$$\mathbf{E}_2 = -j\omega\mathbf{A}^{(2)} - \nabla\phi_e^{(2)} - \frac{1}{\varepsilon_2}\nabla\times\mathbf{F}^{(2)} \tag{A.17}$$

$$\mathbf{H}_2 = \frac{1}{\mu_2}\nabla\times\mathbf{A}^{(2)} - j\omega\mathbf{F}^{(2)} - \nabla\phi_m^{(2)} \tag{A.18}$$

Using the potentials defined as

$$\mathbf{A}^{(i)}(\mathbf{r}) = \frac{\mu_i}{4\pi}\iint_S \mathbf{J}_i(\mathbf{r'})G_i(|\mathbf{r}-\mathbf{r}'|)dS' \qquad \text{Magnetic vector potential} \tag{A.19}$$

$$\mathbf{F}^{(i)}(\mathbf{r}) = \frac{\varepsilon_i}{4\pi}\iint_S \mathbf{M}_i(\mathbf{r'})G_i(|\mathbf{r}-\mathbf{r}'|)dS' \qquad \text{Electric vector potential} \tag{A.20}$$

$$\phi_e^{(i)}(\mathbf{r}) = -\frac{1}{4\pi j\omega\varepsilon_i}\iint_S \nabla'\mathbf{J}_i(\mathbf{r'})G_i(|\mathbf{r}-\mathbf{r}'|)dS' \qquad \text{Electric scalar potential} \tag{A.21}$$

$$\phi_m^{(i)}(\mathbf{r}) = \frac{1}{4\pi j\omega\mu_i}\iint_S \nabla'\mathbf{M}_i(\mathbf{r'})G_i(|\mathbf{r}-\mathbf{r}'|)dS' \qquad \text{Magnetic scalar potential} \tag{A.22}$$

it is possible to introduce the Graf's additional theorem for cylindrical functions

$$G_i(\mathbf{r},\mathbf{r}') = \begin{cases} \displaystyle\sum_{m=-\infty}^{\infty} \frac{1}{4j} J_m(k_2 r) H_m^{(2)}\left(k_2 r'\right) e^{jm\phi} e^{-jm\phi'} & \mathbf{r} \le \mathbf{r}' \quad (i=2) \\ \displaystyle\sum_{m=-\infty}^{\infty} \frac{1}{4j} J_m\left(k_1 r'\right) H_m^{(2)}(k_1 r) e^{jm\phi} e^{-jm\phi'} & \mathbf{r} \ge \mathbf{r}' \quad (i=1) \end{cases} \tag{A.23}$$

and the corresponding cylindrical expansion for the electric and magnetic currents for the TM^z polarization

$$\mathbf{J}_i(\mathbf{r}') = \sum_{n=-\infty}^{\infty} \alpha_n e^{jn\phi'} \mathbf{u}'_z \tag{A.24}$$

$$\mathbf{M}_i(\mathbf{r}') = \sum_{n=-\infty}^{\infty} \beta_n e^{jn\phi'} \mathbf{u}_{\phi'} \tag{A.25}$$

Now, considering (2.50) and (2.51) we can also consider equations (A.26) and (A.27) to write equations $\hat{n} \times \mathbf{E}_1 = \hat{n} \times \mathbf{E}_2$ and $\hat{n} \times \mathbf{H}_1 = \hat{n} \times \mathbf{H}_2$ as a function of only one current, $\mathbf{J}_1$ and $\mathbf{M}_1$.

$$\mathbf{J}_1 = -\mathbf{J}_2 \tag{A.26}$$

$$\mathbf{M}_1 = -\mathbf{M}_2 \tag{A.27}$$

Let us then begin by solving the integral equation for the electric field, $\hat{n} \times \mathbf{E}_1 = \hat{n} \times \mathbf{E}_2$.

$$\left[-j\omega\mathbf{A}^{(1)} - \nabla\phi_e^{(1)} - \frac{1}{\varepsilon_1}\nabla \times \mathbf{F}^{(1)} + \mathbf{E}^{inc} \right]_{tan} = \left[-j\omega\mathbf{A}^{(2)} - \nabla\phi_e^{(2)} - \frac{1}{\varepsilon_2}\nabla \times \mathbf{F}^{(2)} \right]_{tan} \tag{A.28}$$

Dropping the subscript *tan*, which means the tangential components of the vectors involved, and reorganizing, the following expression can be directly obtained

$$\mathbf{E}^{inc} = j\omega\mathbf{A}^{(1)} + \nabla\phi_e^{(1)} + \frac{1}{\varepsilon_1}\nabla \times \mathbf{F}^{(1)} - j\omega\mathbf{A}^{(2)} - \nabla\phi_e^{(2)} - \frac{1}{\varepsilon_2}\nabla \times \mathbf{F}^{(2)} \tag{A.29}$$

Now, to simplify the calculus in (A.29) the unitary vector $\mathbf{u}_r$ is not considered because the solution only consider the tangential components. So therefore, substituting equations (A.19)-(A.22) in (A.29), and also using (A.26) and (A.27), equation (A.29) takes the form,

$$\mathbf{E}^{inc} = j\omega\mu_2 \iint_S \mathbf{J}_1(\mathbf{r}')G_2(\mathbf{r},\mathbf{r}')dS' - \frac{1}{j\omega\varepsilon_2}\nabla \iint_S \nabla'\mathbf{J}_1(\mathbf{r}')G_2(\mathbf{r},\mathbf{r}')dS' +$$

$$\nabla \times \iint_S \mathbf{M}_1(\mathbf{r}')G_2(\mathbf{r},\mathbf{r}')dS' + j\omega\mu_1 \iint_S \mathbf{J}_1(\mathbf{r}')G_1(\mathbf{r},\mathbf{r}')dS' -$$

$$\frac{1}{j\omega\varepsilon_1}\nabla \iint_S \nabla'\mathbf{J}_1(\mathbf{r}')G_1(\mathbf{r},\mathbf{r}')dS' + \nabla \times \iint_S \mathbf{M}_1(\mathbf{r}')G_1(\mathbf{r},\mathbf{r}')dS' \qquad (A.30)$$

Introducing expressions (A.23), (A.24), and (A.25) in (A.30), equation (A.31) is obtained.

$$\mathbf{E}^{inc} = \frac{a\omega\mu_2}{4}\int_0^{2\pi}\sum_{n=-\infty}^{\infty}\alpha_n e^{jn\phi'}\mathbf{u}_{z'}\sum_{m=-\infty}^{\infty}J_m(k_2 r)H_m^{(2)}(k_2 r')e^{jm\phi}e^{-jm\phi'}d\phi' +$$

$$\frac{a}{4\omega\varepsilon_2}\nabla\int_0^{2\pi}\nabla'\left(\sum_{n=-\infty}^{\infty}\alpha_n e^{jn\phi'}\mathbf{u}_{z'}\right)\sum_{m=-\infty}^{\infty}J_m(k_2 r)H_m^{(2)}(k_2 r')e^{jm\phi}e^{-jm\phi'}d\phi' +$$

$$\frac{a}{4j}\nabla\times\int_0^{2\pi}\sum_{n=-\infty}^{\infty}\beta_n e^{jn\phi'}\mathbf{u}_{\phi'}\sum_{m=-\infty}^{\infty}J_m(k_2 r)H_m^{(2)}(k_2 r')e^{jm\phi}e^{-jm\phi'}d\phi' +$$

$$\frac{a\omega\mu_1}{4}\int_0^{2\pi}\sum_{n=-\infty}^{\infty}\alpha_n e^{jn\phi'}\mathbf{u}_{z'}\sum_{m=-\infty}^{\infty}J_m(k_1 r')H_m^{(2)}(k_1 r)e^{jm\phi}e^{-jm\phi'}d\phi' +$$

$$\frac{a}{4\omega\varepsilon_1}\nabla\int_0^{2\pi}\nabla'\left(\sum_{n=-\infty}^{\infty}\alpha_n e^{jn\phi'}\mathbf{u}_{z'}\right)\sum_{m=-\infty}^{\infty}J_m(k_1 r')H_m^{(2)}(k_1 r)e^{jm\phi}e^{-jm\phi'}d\phi' +$$

$$\frac{a}{4j}\nabla\times\int_0^{2\pi}\sum_{n=-\infty}^{\infty}\beta_n e^{jn\phi'}\mathbf{u}_{\phi'}\sum_{m=-\infty}^{\infty}J_m(k_1 r')H_m^{(2)}(k_1 r)e^{jm\phi}e^{-jm\phi'}d\phi' \qquad (A.31)$$

Now, to integrate, the primed unitary vectors have to be substituted as a function of the non-primed unitary vectors. That is $\mathbf{u}'_z = \mathbf{u}_z$ and $\mathbf{u}'_\phi = sin(\phi - \phi')\mathbf{u}_r + cos(\phi - \phi')\mathbf{u}_\phi$. Moreover, it is important to use that $cos(\phi - \phi') = \frac{1}{2}\left(e^{j(\phi-\phi')} + e^{-j(\phi-\phi')}\right)$. On the other hand, the Kronecker Delta function definition (A.7) has been used to solve the above integrals. Thus, substituting

these formulas and rearranging equation (A.31), the following equation is obtained,

$$\mathbf{E}^{inc} = \frac{\pi a \omega}{2} \sum_{m=-\infty}^{\infty} \alpha_m \left(\mu_2 J_m(k_2 r) H_m^{(2)}(k_2 r') + \mu_1 J_m(k_1 r') H_m^{(2)}(k_1 r) \right) e^{jm\phi} \mathbf{u}_z +$$

$$\frac{\pi a}{4jr} \sum_{m=-\infty}^{\infty} \left(J_m(k_2 r) H_m^{(2)}(k_2 r') + r k_2 J'_m(k_2 r) H_m^{(2)}(k_2 r') \right) \cdot$$

$$\left(e^{j(m+1)\phi} \beta_{m+1} + e^{j(m-1)\phi} \beta_{m-1} \right) \mathbf{u}_z +$$

$$\frac{\pi a}{4jr} \sum_{m=-\infty}^{\infty} \left(J_m(k_1 r') H_m^{(2)}(k_1 r) + r k_1 J_m(k_1 r') H_m'^{(2)}(k_1 r) \right) \cdot$$

$$\left(e^{j(m+1)\phi} \beta_{m+1} + e^{j(m-1)\phi} \beta_{m-1} \right) \mathbf{u}_z -$$

$$\frac{\pi a}{4jr} \sum_{m=-\infty}^{\infty} \left(J_m(k_2 r) H_m^{(2)}(k_2 r') + J_m(k_1 r') H_m^{(2)}(k_1 r) \right) \cdot$$

$$\left((m+1) e^{j(m+1)\phi} \beta_{m+1} - (m-1) e^{j(m-1)\phi} \beta_{m-1} \right) \mathbf{u}_z \tag{A.32}$$

At this point, the inner product defined as $< e^{-jn\phi} \mathbf{u}_z, \mathbf{E}^{inc} >$ has to be introduced to delete the summations in (A.32), in the same way as done in equations (A.10) and (A.11). Moreover, equation (A.33) has also to be considered,

$$\sum_{m=-\infty}^{\infty} a_m \alpha_{m\mp 1} \delta_{m\mp 1,n} = a_{m\pm 1} \alpha_n \tag{A.33}$$

And the result is,

$$< e^{-jn\phi}\mathbf{u}_z, \mathbf{E}^{inc} >= \pi^2 a\omega \left(\mu_2 J_n(k_2 r) H_n^{(2)}(k_2 r') + \mu_1 J_n(k_1 r') H_n^{(2)}(k_1 r)\right) \alpha_n$$

$$+ \frac{\pi^2 a}{2j} k_2 \left(H_{n+1}^{(2)}(k_2 r') J_n(k_2 r) - H_{n-1}^{(2)}(k_2 r') J_n(k_2 r)\right) \beta_n$$

$$+ \frac{\pi^2 a}{2j} k_1 \left(J_{n+1}(k_1 r') H_n^{(2)}(k_2 r) - J_{n-1}(k_1 r') H_n^{(2)}(k_1 r)\right) \beta_n \tag{A.34}$$

Rearranging by using the Bessel recurrence relations $\frac{2n}{x} T_n(x) = T_{n-1}(x) + T_{n+1}(x)$ and $2T_n'(x) = T_{n-1}(x) - T_{n+1}(x)$, and the Wronskian $J_n(x)H_n'^{(2)}(x) - J_n'(x)H_n^{(2)}(x) = \frac{2}{\pi x}$, it is finally obtained

$$< e^{-jn\phi}\mathbf{u}_z, \mathbf{E}^{inc} >= \pi^2 a\omega \left(\mu_2 J_n(k_2 r) H_n^{(2)}(k_2 r') + \mu_1 J_n(k_1 r') H_n^{(2)}(k_1 r)\right) \alpha_n$$

$$+ j(\pi a)^2 \left(k_2 J_n'(k_2 r) H_n^{(2)}(k_2 r') + k_1 J_n(k_2 r) H_n'^{(2)}(k_1 r')\right) \beta_n \tag{A.35}$$

Let us continue by solving the integral equation for the magnetic field, $\hat{n} \times \mathbf{H}_1 = \hat{n} \times \mathbf{H}_2$.

$$\left[-j\omega\mathbf{F}^{(1)} - \nabla\phi_m^{(1)} + \frac{1}{\mu_1}\nabla \times \mathbf{A}^{(1)} + \mathbf{H}^{inc}\right]_{tan} =$$

$$\left[-j\omega\mathbf{F}^{(2)} - \nabla\phi_m^{(2)} + \frac{1}{\mu_2}\nabla \times \mathbf{A}^{(2)}\right]_{tan} \tag{A.36}$$

Dropping the subscript *tan*, which means the tangential components of the vectors involved, and reorganizing, the following expression can be directly obtained

$$\mathbf{H}^{inc} = j\omega\mathbf{F}^{(1)} + \nabla\phi_m^{(1)} - \frac{1}{\mu_1}\nabla \times \mathbf{A}^{(1)} - j\omega\mathbf{F}^{(2)} - \nabla\phi_m^{(2)} + \frac{1}{\mu_2}\nabla \times \mathbf{A}^{(2)} \tag{A.37}$$

Now, to simplify the calculus in (A.37) the unitary vector $\mathbf{u}_r$ is not considered because the solution only consider the tangential components. So therefore, substituting equations (A.19)-(A.22) in (A.37), and also using (A.26) and (A.27), equation (A.37) takes the form,

$$\mathbf{H}^{inc} = j\omega\varepsilon_2 \iint_S \mathbf{M}_1(\mathbf{r}')G_2(\mathbf{r},\mathbf{r}')dS' - \frac{1}{j\omega\mu_2}\nabla \iint_S \nabla'\mathbf{M}_1(\mathbf{r}')G_2(\mathbf{r},\mathbf{r}')dS' -$$
$$\nabla \times \iint_S \mathbf{M}_1(\mathbf{r}')G_2(\mathbf{r},\mathbf{r}')dS' + j\omega\varepsilon_1 \iint_S \mathbf{M}_1(\mathbf{r}')G_1(\mathbf{r},\mathbf{r}')dS' -$$
$$\frac{1}{j\omega\mu_1}\nabla \iint_S \nabla'\mathbf{M}_1(\mathbf{r}')G_1(\mathbf{r},\mathbf{r}')dS' - \nabla \times \iint_S \mathbf{J}_1(\mathbf{r}')G_1(\mathbf{r},\mathbf{r}')dS' \qquad (A.38)$$

Introducing expressions (A.23), (A.24), and (A.25) in (A.38), equation (A.39) is obtained.

$$\mathbf{H}^{inc} = \frac{a\omega\varepsilon_2}{4}\int_0^{2\pi} \sum_{n=-\infty}^{\infty} \beta_n e^{jn\phi'}\mathbf{u}_{\phi'} \sum_{m=-\infty}^{\infty} J_m(k_2 r) H_m^{(2)}\left(k_2 r'\right) e^{jm\phi} e^{-jm\phi'} d\phi' +$$
$$\frac{a}{4\omega\mu_2}\nabla \int_0^{2\pi} \nabla' \left(\sum_{n=-\infty}^{\infty} \beta_n e^{jn\phi'}\mathbf{u}_{\phi'} \right) \sum_{m=-\infty}^{\infty} J_m(k_2 r) H_m^{(2)}\left(k_2 r'\right) e^{jm\phi} e^{-jm\phi'} d\phi' -$$
$$\frac{a}{4j}\nabla \times \int_0^{2\pi} \sum_{n=-\infty}^{\infty} \alpha_n e^{jn\phi'}\mathbf{u}_{z'} \sum_{m=-\infty}^{\infty} J_m(k_2 r) H_m^{(2)}\left(k_2 r'\right) e^{jm\phi} e^{-jm\phi'} d\phi' +$$
$$\frac{a\omega\varepsilon_1}{4}\int_0^{2\pi} \sum_{n=-\infty}^{\infty} \beta_n e^{jn\phi'}\mathbf{u}_{\phi'} \sum_{m=-\infty}^{\infty} J_m\left(k_1 r'\right) H_m^{(2)}(k_1 r) e^{jm\phi} e^{-jm\phi'} d\phi' +$$
$$\frac{a}{4\omega\mu_1}\nabla \int_0^{2\pi} \nabla' \left(\sum_{n=-\infty}^{\infty} \beta_n e^{jn\phi'}\mathbf{u}_{\phi'} \right) \sum_{m=-\infty}^{\infty} J_m\left(k_1 r'\right) H_m^{(2)}(k_1 r) e^{jm\phi} e^{-jm\phi'} d\phi' -$$
$$\frac{a}{4j}\nabla \times \int_0^{2\pi} \sum_{n=-\infty}^{\infty} \alpha_n e^{jn\phi'}\mathbf{u}_{z'} \sum_{m=-\infty}^{\infty} J_m\left(k_1 r'\right) H_m^{(2)}(k_1 r) e^{jm\phi} e^{-jm\phi'} d\phi' \qquad (A.39)$$

Now, to integrate, the primed unitary vectors have to be substituted as a function of the non-primed unitary vectors. That is $\mathbf{u}'_z = \mathbf{u}_z$ and $\mathbf{u}'_\phi = sin(\phi - \phi')\mathbf{u}_r + cos(\phi - \phi')\mathbf{u}_\phi$. Moreover, it is important to use that $cos(\phi - \phi') =$

$\frac{1}{2}\left(e^{j(\phi-\phi')}+e^{-j(\phi-\phi')}\right)$. On the other hand, the Kronecker Delta function definition (A.7) has been used to solve the above integrals. Thus, substituting these formulas and rearranging equation (A.39), the following equation is obtained,

$$\mathbf{H}^{inc}=\frac{\pi a\omega}{4}\sum_{m=-\infty}^{\infty}\left(\varepsilon_2 J_m\left(k_2 r\right)H_m^{(2)}\left(k_2 r'\right)+\varepsilon_1 J_m\left(k_1 r'\right)H_m^{(2)}\left(k_1 r\right)\right)\cdot$$

$$\left(e^{j(m+1)\phi}\beta_{m+1}+e^{j(m-1)\phi}\beta_{m-1}\right)\mathbf{u}_\phi-$$

$$\frac{\pi a}{2\omega r' r}\sum_{m=-\infty}^{\infty}\left(\frac{1}{\mu_2}J_m\left(k_2 r\right)H_m^{(2)}\left(k_2 r'\right)+\frac{1}{\mu_1}J_m\left(k_1 r'\right)H_m^{(2)}\left(k_1 r\right)\right)m^2 e^{jm\phi}\beta_m\mathbf{u}_\phi+$$

$$\frac{\pi a r}{2}\sum_{m=-\infty}^{\infty}\left(J_m\left(k_2 r\right)H_m^{(2)}\left(k_2 r'\right)+J_m\left(k_1 r'\right)H_m^{(2)}\left(k_1 r\right)\right)m\alpha_m e^{jm\phi}\mathbf{u}_\phi \qquad (A.40)$$

At this point, the inner product defined as $< e^{-jn\phi}\mathbf{u}_\phi, \mathbf{H}^{inc} >$ has to be introduced to delete the summations in (A.40), in the same way as done in equations (A.10) and (A.11). Moreover, equation (A.41) has also to be considered,

$$\sum_{m=-\infty}^{\infty} a_m\alpha_{m\mp1}\delta_{m\mp1,n}=a_{m\pm1}\alpha_n \qquad (A.41)$$

And the result is,

$$\left\langle e^{-jn\phi}\mathbf{u}_\phi,\mathbf{H}^{inc}\right\rangle=(\pi a)^2\omega\cdot$$

$$\left[\left(\frac{\varepsilon_2}{2}J_{n-1}\left(k_2 r\right)H_{n-1}^{(2)}\left(k_2 r'\right)+\frac{\varepsilon_1}{2}J_{n-1}\left(k_1 r'\right)H_{n-1}^{(2)}\left(k_1 r\right)\right)+\right.$$

$$\left.\left(\frac{\varepsilon_2}{2}J_{n+1}\left(k_2 r\right)H_{n+1}^{(2)}\left(k_2 r'\right)+\frac{\varepsilon_1}{2}J_{n+1}\left(k_1 r'\right)H_{n+1}^{(2)}\left(k_1 r\right)\right)\right]\beta_n-$$

$$\frac{(\pi an)^2}{2}\left(\frac{1}{\mu_2}J_n\left(k_2 r\right)H_n^{(2)}\left(k_2 r'\right)+\frac{1}{\mu_1}J_n\left(k_2 r\right)H_n^{(2)}\left(k_2 r'\right)\right)\beta_n+$$

$$(\pi a)^2 nr\left(J_n\left(k_2 r\right)H_n^{(2)}\left(k_2 r'\right)+J_n\left(k_1 r'\right)H_n^{(2)}\left(k_1 r\right)\right)\alpha_n \qquad (A.42)$$

Rearranging by using the Bessel recurrence relations $\frac{2n}{x}T_n(x) = T_{n-1}(x) + T_{n+1}(x)$ and $2T_n'(x) = T_{n-1}(x) - T_{n+1}(x)$, and the Wronskian $J_n(x)H_n'^{(2)}(x) - J_n'(x)H_n^{(2)}(x) = \frac{2}{\pi x}$, it is finally obtained

$$\left\langle e^{-jn\phi}\mathbf{u}_\phi, \mathbf{H}^{inc}\right\rangle =$$

$$-j(\pi a)^2\left(k_2 J_n'(k_2 r)H_n^{(2)}\left(k_2 r'\right) + k_1 J_n(k_2 r)H_n'^{(2)}\left(k_1 r'\right)\right)\alpha_n +$$

$$(\pi a)^2\omega\left(\varepsilon_2 J_n'(k_2 r)H_n'^{(2)}\left(k_2 r'\right) + \varepsilon_1 J_n'\left(k_1 r'\right)H_n'^{(2)}(k_1 r)\right)\beta_n \tag{A.43}$$

Concerning the TE^z case can be exactly extracted considering the same analytical procedure but considering the equivalent currents (A.44). Another way is considering the duality between the TM^z and TE^z electromagnetic fields.

$$\left\{\begin{array}{c}\mathbf{J}\\ \mathbf{M}\end{array}\right\}^{TE^z} = \sum_{n=-\infty}^{\infty}\left\{\begin{array}{c}\alpha_n^{TE^z}\\ \beta_n^{TE^z}\end{array}\right\}e^{jn\phi}\left\{\begin{array}{c}\widehat{\phi}\\ \widehat{z}\end{array}\right\} \tag{A.44}$$

The final solutions for the TE^z are:

$$< e^{-jn\phi}\mathbf{u}_\phi, \mathbf{E}^{inc} >=$$

$$(\pi a)^2\omega\left(\mu_2 J_n'(k_2 r)H_n'^{(2)}\left(k_2 r'\right) + \mu_1 J_n'\left(k_1 r'\right)H_n'^{(2)}(k_1 r)\right)\alpha_n +$$

$$j(\pi a)^2\left(k_2 J_n'(k_2 r)H_n^{(2)}\left(k_2 r'\right) + k_1 J_n(k_2 r)H_n'^{(2)}\left(k_1 r'\right)\right)\beta_n \tag{A.45}$$

$$< e^{-jn\phi}\mathbf{u}_z, \mathbf{H}^{inc} >=$$

$$-j(\pi a)^2\left(k_2 J_n'(k_2 r)H_n^{(2)}\left(k_2 r'\right) + k_1 J_n(k_2 r)H_n'^{(2)}\left(k_1 r'\right)\right)\alpha_n +$$

$$(\pi a)^2\omega\left(\varepsilon_2 J_n(k_2 r)H_n^{(2)}\left(k_2 r'\right) + \varepsilon_1 J_n\left(k_1 r'\right)H_n^{(2)}(k_1 r)\right)\beta_n \tag{A.46}$$

Appendix B

Publications

B.1 Journals

1. **Tomás Bernabeu-Jiménez**, Alejandro Valero-Nogueira, Felipe Vico, Ahmed A Kishk: *A Comparison between Natural Resonances and Characteristic Mode Resonances of an infinite circular cylinder*- IEEE Antennas and Propagation, Vol. 65, no. 5, pp. 2759-2763, May. 2017.

2. **Tomás Bernabeu-Jiménez**, Alejandro Valero-Nogueira, Felipe Vico, Ahmed A Kishk: *Internal Natural Resonances Prediction through the Theory of Characteristic Modes*-(Under minor revision review for publication in Radio Science).

3. **Tomás Bernabeu-Jiménez**, Alejandro Valero-Nogueira, Felipe Vico, Ahmed A Kishk: *On the Contribution to the Field of the Non-Physical Characteristic Modes*-(Under minor revision review for publication in Transactions on Antennas and Propagation).

B.2 International Conferences

1. F Gallée, **T Bernabeu-Jiménez**, M Cabedo-Fabres, E Antonino-Daviu, A Valero-Nogueira: *Application of the Theory of Characteristic Modes to the Design of Compact Metallic Strip Antenna with Multilayer Technology (LTCC)*. Antennas and Propagation (EuCAP), 7th European Conference 1891,1895, 8-12 April 2013, Gothenburg, Sweden; 04/2013

2. François Gallée, **T Bernabeu-Jiménez**, Marta Cabedo-Fabres, E Antonino-Daviu, A Valero-Nogueira, Christian Person: *Conception d'une antenne de type DRA à 60GHz avec la théorie des modes caractéristiques*. 18 èmes Journées Nationales Microondes, Paris; 05/2013

3. **T Bernabeu-Jiménez**, Felipe Vico-Bondia, A Valero-Noguera, Marta Cabedo-Fabres, E Antonino-Daviu, François Gallée: **Understanding the Analytical Formulation of the Characteristic Modes of a Metallic Sphere**. Antennas and Propagation Society International Symposium (APSURSI), Orlando; 07/2013

4. **T. Bernabeu-Jiménez**, A. Valero-Nogueira, F. Vico-Bondia, A. Vila-Jimenez, D. Sánchez-Escuderos, F. Gallé: *A 60-GHz Coplanar-Waveguide-Fed Slot-Coupled Rectangular DRA Design Using The Theory of Characteristic Modes*. European Conference on Antennas and Propagation, Lisbon (Portugal); 04/2015

5. François Gallé, J P Coupez, Marta Cabedo-Fabres, Eva Antonino-Daviu, **T. Bernabeu-Jiménez**, A. Valero-Nogueira: *Use of the Characteristic Modes Theory for the Design of an Antenna in a Harsh Environment from a Generic Antenna Topology*. European Conference on Antennas and Propagation, Lisbon (Portugal); 04/2015

6. **T Bernabeu-Jiménez**, A Valero-Nogueira, F Vico-Bondia, A A Kishk: *New Look of the Mysteries of the Characteristic Modes*. 1st URSI Atlantic Radio Science Conference, May, 2015 (URSI AT- RASC), Gran Canaria (Spain)

7. **T Bernabeu-Jiménez**, A Valero-Nogueira, F Vico-Bondia, Ahmed A Kishk: *Relation between Characteristic Modes and Complex Natural Resonances*. IEEE International Symposium on Antennas and Propagation and USNC-URSI National Radio ScienceMeeting, Vancouver (Canada), July, 2015.

8. **T Bernabeu-Jiménez**, A Valero-Nogueira, F Vico-Bondia, E Antonino-Daviu, M Cabedo-Fabres: *A 60-GHz LTCC Rectangular Dielectric Resonator Antenna design with Characteristic Modes Theory*. IEEE International Symposium on Antennas and Propagation (APS), Memphis, Tennessee; 07/2014

9. M. Cabedo-Fabres, E. Antonino-Daviu, **T. Bernabeu-Jimenez**, M. Ferrando-Bataller: *Review and application of the theory of characteristic modes for open radiating structures*. 2015 European Microwave Conference (EuMC 2015)

B.3 National Conferences

1. **Tomás Bernabeu-Jiménez**, Alejandro Valero-Nogueira, Felipe Vico-Bondia, Antonio Vila-Jiménez, Daniel Sánchez-Escuderos: *Diseño de una DRA Alimentada por Ranura y Guía de Ondas Coplanar mediante la Teoría de Modos Característicos a 60GHz en Tecnología LTCC*. XXIX Simposium Nacional de la Unión Científica Internacional de Radio (URSI), Valencia (Spain); 09/2014

B.4 Nonrelated

1. Felipe Vico, Miguel Ferrando-Bataller, **Tomás Bernabeu-Jiménez**, Antonio Berenguer: *A High Order Locally Corrected Nyström Implementation of the Decoupled Potential Integral Equation*. European Conference on Antennas and Propagation, Lisbon (Portugal); 04/2015

2. Antonio Berenguer, Mariano Baquero-Escudero, Daniel Sanchez-Escuderos, **Tomas Bernabeu-Jimenez**, Felipe Vico: *Design of coupled-line components with the Suspended-Strip Gap Waveguide at mm-wave frequencies*. 2015 USNC-URSI Radio Science Meeting (Joint with AP-S Symposium)

3. Felipe Vico, Miguel Ferrando-Bataller, **Tomas Bernabeu-Jimenez**, Antonio Berenguer: *Decoupled potential integral equation applied to complex geometries*. 2015 IEEE International Symposium on Antennas and Propagation & USNC/URSI National Radio Science Meeting

4. Felipe Vico, Miguel Ferrando-Bataller, **Tomas Bernabeu Jimenez**, Daniel Sanchez-Escuderos: *A decoupled charge-current formulation for the scattering of homogeneous lossless dielectrics*. 2016 10th European Conference on Antennas and Propagation (EuCAP)

5. F Vico, M Ferrando-Bataller, **T Bernabeu-Jiménez**, D Sánchez-Escuderos: *A non-resonant single source augmented integral equation for the scattering problem of homogeneous lossless dielectrics*, 2016 IEEE International Symposium on Antennas and Propagation (APSURSI)